

A Double-Sided Tubular Linear Synchronous Generator for Wave-Energy Conversion

Danson Michael Joseph

A thesis submitted to the Faculty of Engineering and the Built Environment, University of the Witwatersrand, Johannesburg, in fulfilment of the requirements for the degree of Doctor of Philosophy.

Johannesburg, May 2010

Declaration

I declare that this thesis is my own, unaided work, except where otherwise acknowledged. It is being submitted for the degree of Doctor of Philosophy to the University of the Witwatersrand, Johannesburg. It has not been previously submitted for any degree or examination to any other university.

Signed this, the _____ day of _____, in the year _____

Danson Michael Joseph

Abstract

In the field of renewable energy, ocean wave energy is one of the least commercialised resources. This is mainly attributable to the harsh environment and the technical requirements of the environment. In recent years, a vast array of new technologies have been developed for this application. Of these, some have considered the oscillatory action of the ocean waves conducive to the use of linear generators in direct-drive actuators.

Linear generators may be classified into either tubular machines, which encapsulate the magnetic flux very well, or single- and double-sided flat machines. Double-sided flat layouts exhibit very high force capabilities because of the presence of a second air-gap.

A Double-Sided Tubular machine is proposed which exhibits the force density of a double-sided flat machine combined with the superior flux efficiency of a tubular machine. The hypothesis of the present research is that this new layout will accentuate these benefits beyond the potential of the double-sided flat linear machine layout.

The machine's performance was quantified on the basis of its force capability, the mathematics of which are dealt with in detailed magnetic vector potential calculations. Simulations of two full-scale machine designs and a prototype machine were performed using Finite-Element Analysis. Fourier analysis was employed extensively to quantify the performance of the designs.

The mathematical model developed through this work is fairly accurate. The calculated machine performance deviates from the simulated and measured force capabilities by at most 1.54% for all cases which are presented.

A simulated comparison between the double-sided flat layout and the double-sided tubular layout indicates that the latter may have up to a 47% smaller volume than the former and use as little as a 83% of the permanent-magnet material as the former.

The results are compelling in terms of the possible advantages of the layout. The machine deserves further investigation, mainly into the mechanical design and integration into a complete wave-energy converter system. Notably, the bearing system requires investigation with due cognisance given to the nature of the application. Consideration may also be given to the use of soft-magnetic composites to eliminate the obstacles that tapered laminations pose in the commercialisation of tubular machines.

To my Father and Mother

For their unyielding commitment to my upbringing and education

Acknowledgements

My postgraduate study has been punctuated by adventures into various fields of engineering. Through all these deviations from my ultimate goal of graduation, the environment, through those who have defined it, has been extremely conducive to adventurous thought and experimentation.

Firstly to my Lord Jesus Christ for giving me a spirit of adventure and inquisition, I thank you. May I always use that which I have been blessed with to bless others.

I owe much of my success in this project to the continual patience and support of Professor Willem A. Cronje of the Machines Research Group at the University of the Witwatersrand. Beyond this project he has provided testimony for me in my professional career and guidance throughout my years of study.

The prototype for this research was constructed in the Electrical Engineering Workshop in the Genmin Laboratories. A great deal of thanks is due to Mr Harry Fellows and his colleagues for their work towards the machine's completion. Mr Fellows always offered his expertise on the construction of the machine and the production of its components.

A number of external companies were involved in the production of components for the prototype. These include SIMA Turners (Pty) Ltd. and Bascol (Pty) Ltd. of Johannesburg. One particular mention however is due to Mr Mark Pardini, of Transvaal Electric Company (Pty) Ltd., for his material contribution and engineering expertise, which he offered to the project on many occasions. His company produced the stator coils for the prototype at no cost to the University. These windings were exceptional in their manufacture and invaluable to the construction of the machine.

Finally, and with special credit, I thank my wife Rebecca Joseph for her patience and support through the many years of this research. At many stages during the project it was her presence which gave me the will to continue.

Contents

Declaration	i
Abstract	ii
Acknowledgements	iv
List of Figures	viii
List of Tables	x
List of Symbols	xi
Source Code Listings	xv
1 Introduction	1
2 Background	4
2.1 Energy as a Resource	4
2.2 Wave Energy Conversion	12
2.2.1 Wave Mechanics	13
2.2.2 Wave Energy Conversion Technology	16
2.3 The Application of Linear Generators to Wave-Energy Conversion	20
2.4 Conclusions	23
3 The Double-Sided Tubular Linear Machine	24
3.1 Translator Layout	24
3.2 Stator Layout	28
3.3 Conclusions	29
4 Performance Calculations	30
4.1 Modelling of Magnetic Materials	31
4.1.1 Modelling of Permanent-Magnet Materials	31
4.1.2 Modelling Ferromagnetic Materials	37

4.2	Power in Oscillating Wave-Energy Systems	40
4.2.1	The Mechanical Power of the Swells	40
4.2.2	The Electrical Power Delivered by the Generator	41
4.2.3	Phasor Representation of the Double-Sided Tubular Machine	42
4.2.4	Electrical Power Factor	45
4.2.5	Magneto-Motive Forces	46
4.3	Electromagnetic Force using the Magnetic Vector Potential Method	49
4.3.1	The Magnetic Flux Density of the Stator Windings	49
4.3.2	The Force of the Stator Acting on the Translator	52
4.3.3	Minimisation of the Harmonic Force Ripple	53
4.4	Magnetic Circuit	53
4.4.1	Simplified Magnetic Circuit	54
4.4.2	Magnetic Flux Linkage	55
4.4.3	Total Magnetic Flux per Pole	55
4.4.4	The Effective Air-gap	56
4.4.5	Saturation Factor, k_{sat}	57
4.4.6	Slot Leakage Factor, k_{sl}	57
4.4.7	Reluctances	58
4.5	Mechanical Considerations	66
4.5.1	Stator Core Constraints	66
4.5.2	Translator Core Constraints	67
4.6	Machine Design Procedure Using The Performance Calculations	67
4.7	Conclusions	70
5	Validation of the Performance Calculations	71
5.1	Simulated Validation	71
5.1.1	Analysis of the AWS Machine	71
5.1.2	Analysis of the Double-Sided Tubular Machine	74
5.2	Measured Validation	78
5.3	Conclusions	82
6	Conclusions	83
6.1	Guidelines for Future Investigations	84
6.1.1	Mechanical Considerations	84
6.1.2	Magnetic Considerations	85
6.2	Contribution of the Present Research to the Scientific Community	85
	References	87

Appendices	93
A Software Scripts	94
A.1 Mathematica	95
A.2 FEMM Lua	110
A.3 Octave Analysis	125
A.4 Octave Utilities	130
B Laplace’s Equation in Cylindrical Coordinates	133
C Prototype Construction	137
C.1 Specifications and Design	137
C.1.1 Specifications	137
C.1.2 Computer Aided Design	143
C.2 Construction Procedure	154
C.2.1 Translator Construction	154
C.2.2 Inner Stator Construction	157
C.2.3 Outer Stator Construction	159
C.2.4 Stator and Translator Integration	161
C.3 Conclusion	162

List of Figures

2.1	The Relationship between the Various Forms of Energy	5
2.2	The Fossil Fuel Energy Balance	6
2.3	Classification of Energy Reserves	8
2.4	The Energy Content of Sustainable Resources	10
2.5	Wave Energy Resource Map	13
2.6	Ocean Wave Shapes	14
2.7	Ocean Wave Mechanics	15
2.8	Wave Energy Absorber Technology	18
2.9	The Archimedes Wave Swing	19
2.10	Tubular and Flat Linear Machine Layouts	21
3.1	The Double-Sided Tubular Linear Machine	25
3.2	Permanent-Magnet Array Configurations	25
3.3	Space-Harmonics of Permanent-Magnets	27
4.1	Demagnetisation Curves of Permanent-Magnets	32
4.2	Permanent-Magnet Equivalent Circuit Models	34
4.3	Fictitious Edge-Current Representation of Permanent-Magnets	34
4.4	Fundamental mmf Distribution of Permanent-Magnets	35
4.5	Ferromagnetic Magnetisation Curve	38
4.6	Approximation of the Relative Permeability of Ferromagnetic Materials	39
4.7	Linear Force and Induced Linear Velocity	40
4.8	Induced Voltage of a Linear Generator under Oscillating Actuation	42
4.9	Phasor Diagram of the Permanent-Magnet Generator	43
4.10	Magnetic Vector Potential Model	50
4.11	Magnetic Circuit of the Active Flux	54
4.12	The Effect of Carter's Coefficient	56
4.13	Slot-Leakage Magnetic Circuit	57
4.14	Air-gap Reluctance	59

4.15	Translator Core Reluctance	60
4.16	Stator Core Reluctance	61
4.17	Stator Teeth Reluctance	63
4.18	Stator Slot Reluctance	65
4.19	Design Optimisation Objective Functions	69
5.1	FEA Model of the AWS' Machine	73
5.2	Force Distribution of the AWS' Machine	73
5.3	Harmonic Force Components of the AWS' Machine	74
5.4	FEA Models of the Full-scale Designs	76
5.5	Full-scale Designs' Force Distributions	77
5.6	Full-scale Designs' Harmonic Force Components.	77
5.7	Photograph of the Prototype Machine	79
5.8	FEA Model of the Prototype Machine	79
5.9	Measurement Apparatus: Rheostats	81
5.10	Measurement Apparatus: Scales	81
C.1	3D CAD Representation and Photograph of the Prototype Machine	143
C.2	CAD: Top System Support: SIMA-01	144
C.3	CAD: Outer Stator Support: SIMA-02	145
C.4	CAD: Bottom System Support: SIMA-04	146
C.5	CAD: Bearing Sleeve for the 66/22-2RS1 Bearings: EIE-01	147
C.6	CAD: Inner Stator Upper Support: EIE-02	148
C.7	CAD: Inner Stator Lower Support: EIE-03	149
C.8	CAD: Top Support Bearing Assembly: LC-02 and LC-03	150
C.9	CAD: Outer Stator Bearing Assembly: LC-04 and LC-05	151
C.10	CAD: Inner Stator Bearing Assembly: LC-06 and LC-07	152
C.11	CAD: Vesconite Retaining Rings: VC-01 and VC-02	153
C.12	Translator Assembly: Supporting Structures	154
C.13	Translator Assembly: Magnet Placement	155
C.14	Translator Assembly: Completion	156
C.15	Inner Stator Assembly	157
C.16	Outer Stator Assembly	159
C.17	Outer Stator Assembly: Brazing	160
C.18	Stator and Translator Integration	161
C.19	Completed Prototype Machine	162

List of Tables

2.1	Entropies of Universal Energy Forms	5
2.2	Global Energy Reserves	9
2.3	The Energy Content of Sustainable Resources	11
5.1	System Parameters of the AWS	72
5.2	Design Specifications of the AWS' Machine	72
5.3	Full-scale Double-Sided Tubular Machine Designs	75
5.4	Specifications of the Prototype Machine	80
5.5	Performance of the Prototype Machine	82
6.1	Caparison of the Machine Layouts	83
C.1	Specifications of the Prototype Machine	138
C.2	Supplier Information	138
C.3	Bill of Materials for the Prototype Machine	140

List of Symbols

Note: Given any variable of RMS value X , the instantaneous function is represented by \tilde{X} , the peak value by \hat{X} , and the average value by \bar{X} .

Latin Letters

A	Area	m^2
a_h	Armature Harmonic Line Current Distribution	A/m
B	Magnetic Flux Density	T
B_i	Intrinsic Magnetic Flux Density	T
B_r	Remnant Magnetic Flux Density	T
C_h	Fourier Coefficient	
c	Speed of Light	m/s
E	Energy	J
\mathcal{E}	Induced <i>emf</i>	V
\mathcal{E}_m	Motion Induced <i>emf</i>	V
\mathcal{E}_p	Pulsation Induced <i>emf</i>	V
F	Linear Force	N
\mathcal{F}	Magneto-Motive Force	A
f	Frequency	Hz
g	Effective Gap Length	m
H	Magnetic Field Intensity	A/m
H_c	Coercive Magnetic Field Intensity	A/m
H_i	Intrinsic Magnetic Field Intensity	A/m
h	Harmonic Order	
I	Current	A
I_n	Modified Bessel Function of the First Kind of Order n	
J	Current Density	A/m^2
K_n	Modified Bessel Function of the Second Kind of Order n	
k	General Constant Defined by Subscript	
k_c	Carter's Coefficient	

k_{dn}	Distribution Factor	
k_f	Form Factor of the Excitation Field	
k_{fill}	Slot Fill Factor	
k_l	Slot Radial Length Coefficient	m^2/A
k_{pn}	Pitch Factor	
k_{sat}	Saturation Factor	
k_{sl}	Slot-Leakage Factor	
k_{st}	Lamination Stacking Factor	
k_w	Winding Factor	
k_Λ	Permeance Coefficient	
k_ϕ	Ratio of $\hat{\Phi}$ to $\hat{\Phi}_1$	
L	Length - Typically Axial	m
l	Length - Typically Radial	m
M	Permanent-Magnet Intrinsic Magnetisation	A/m
m	Mass	kg
m	Number of phases	
N	Number of Series Turns	
n_c	Number of Coils per Pole per Phase	
P	Active Power	W
P	Pressure	Pa
p	Number of Poles	
Q	Specific Electric Loading	A/m
q	Slots per Pole per Phase	
R	Electrical Resistance	Ω
\mathcal{R}	Magnetic Reluctance	A/Wb
r	Radius or Radial Dimension	m
S	Mechanical or Electrical Apparent Power	Nm/s or VA
T_{op}	Magnet Operating Temperature	$^\circ\text{C}$
t	Time	s
V	Voltage	V
\mathcal{V}	Linear Velocity	m/s
\mathcal{V}_s	Synchronous Linear Velocity	m/s
v	Volume	m^3
w	Permanent-Magnet Energy Density	J/m^3
X	Electrical Reactance	Ω
Z	Electrical Impedance	Ω
z	Axial Dimension	m

Greek Letters

α_B	Temperature Coefficient of B	%/°C
α_c	Ratio of τ_c to τ_p	
α_H	Temperature Coefficient of H	%/°C
α_m	Ratio of τ_m to τ_p	
α_{sl}	Ratio of τ_{sl} to $\tau_{sl} + \tau_t$	
α_t	Ratio of τ_t to $\tau_{sl} + \tau_t$	
β	Angular Period: Ratio of π to τ_p	rad/m
γ	Lorentz Factor for Special Relativity	
γ_m	Form Factor of the Demagnetisation Curve	
δ	Force Displacement (Force Angle: $\beta\delta$)	m
η	Efficiency	%
θ	Phase Angle	rad
Λ	Magnetic Permeance	Wb/A
λ	Flux Linkage	Wb
λ	Load Angle	rad
λ	Wave-length	m
μ	Permeability	H/m
μ_0	Permeability of Free Space = $4\pi \times 10^{-7}$	H/m
μ_r	Relative Permeability	
μ_{rrec}	Permanent-Magnet Relative Recoil Permeability	
ρ	Density	kg/m ³
τ_c	Coil-Pitch	m
τ_m	Mechanical Magnet-Pitch	m
τ_o	Mechanical Slot-Opening-Pitch	m
τ_p	Mechanical Pole-Pitch	m
τ_{sl}	Mechanical Slot-Pitch	m
τ_t	Mechanical Tooth-Pitch	m
Φ	Magnetic Loading/Flux per Pole	Wb
ϕ	Angular Displacement	rad
ϕ	Azimuthal Displacement or Dimension	rad
χ	Magnetic Susceptibility	
ω	Angular Velocity	rad/s

Subscripts

20	Base Temperature of 20°C
<i>a</i>	Air-gap (<i>ai</i> or <i>ao</i>)
<i>c</i>	Coil
<i>c</i>	Stator Core (<i>ci</i> or <i>co</i>)
<i>ct</i>	Translator Core
<i>e</i>	Electrical
<i>g</i>	Air-gap
<i>h</i>	The h^{th} harmonic order
<i>i</i>	Inner Stator
<i>m</i>	Magnet (<i>mi</i> or <i>mo</i>)
<i>m</i>	Mechanical
<i>max</i>	Maximum
<i>min</i>	Minimum
<i>o</i>	Outer Stator
<i>ph</i>	Phase
<i>r</i>	Remnant
<i>r</i>	Resultant
<i>s</i>	Stator (<i>si</i> or <i>so</i>)
<i>sat</i>	Saturation
<i>sl</i>	Slot or Slot-Leakage
<i>st</i>	Series Turn
<i>t</i>	Teeth (<i>ti</i> or <i>to</i>)
<i>t</i>	Translator

Source Code Listings

A.1	Machine Performance Calculation Script	95
A.2	Machine Design Script	101
A.3	Script to Solve for C_{hII}	109
A.4	System Construction & Simulation: Double-Sided Tubular Machine	110
A.5	System Construction & Simulation: AWS Machine	112
A.6	Simulation Post-Processing: Double-Sided Tubular Machine	114
A.7	Simulation Post-Processing: AWS Machine	116
A.8	Lua Function Definitions	117
A.9	Simulation Input Parameter File: Double-Sided Tubular Machine	121
A.10	Simulation Input Parameter File: AWS Machine	123
A.11	Processing of Prototype Measurements	125
A.12	Force Analysis of FEMM Results	129
A.13	Saving of GNUPlot Data to File	130
A.14	Removal of Sub-Harmonic Signals	130
A.15	Fourier Series Coefficient Calculations	131
A.16	Pattern Correlation	131
A.17	Pattern Averaging and Correlation	132

Chapter 1

Introduction

We are in the age of dwindling energy resources and peak extraction of primary fuel resources. The ramifications of the use of fossil fuels on our global climate are an ever increasing concern. It is against this backdrop that research and development is being driven into the exploitation of resources which are sustainable in the long term. Of these, hydro power has had the greatest success, though it is limited in application due to geographic constraints. Wind power has also been a major player to date. Photo-voltaic solar power has been widely deployed and solar-thermal power is at a point of consolidated technical understanding where bankable deployment is possible.

Ocean wave energy on the other hand has lagged behind the rest. This is primarily due to the extremely harsh conditions that systems have to survive. Ocean swells are highly concentrated in their energy content. Whereas solar energy may provide a peak energy density of up to 1 kW/m^2 , ocean swells may exhibit *average* energy densities of up to 100 kW/m of incident wave front, peaking at values up to 1000 kW/m . With the obvious wealth of the resource, and refined techniques to battle the harsh ocean conditions, various new technologies have surfaced for the application.

Given the objective of survivability, many designs have called for direct-drive generation systems. These reduce the number of mechanical components and increase the reliability of the systems. In light of this, some systems have been developed to take advantage of the natural oscillatory nature of the ocean waves by using linear generators as the power conversion technology. A notable example of this is the Archimedes Wave SwingTM (AWS) which is the reference platform on which this research is based[1].

The plight of nearly all renewable energy systems is their relatively high cost when compared to fossil-fuel based generation. This affects their commercial viability. In wave-energy systems employing linear generators, the linear generator becomes a crucial design package. The generator cost contributes significantly to the overall project cost.

In present linear generator designs, only single-stator tubular and double-sided flat lay-

outs are typical. Each layout has its own advantages in terms of magnetic flux encapsulation and force density. The higher force density of the double-sided flat machine layout improves the material utilisation of the machine. The better flux encapsulation of the tubular machine layout improves the magnetic flux efficiency of the machine, and results in a better utilisation of the permanent-magnet material. The greater these two metrics, the lower the machine volume per unit of energy output, and typically, the lower the cost. However, these layouts are relatively well understood, and their optimisation has reached its limits in terms of these critical metrics for success.

It is in this context that a new machine layout is proposed, termed a Double-Sided Tubular machine. It exhibits the force density of a double-sided flat machine combined with the superior flux efficiency of a tubular machine. The hypothesis of the design is that by combining the fundamental structures of the two former layouts, the proposed machine will accentuate these benefits, resulting in a higher force density than is possible from the present double-sided flat layout. This would affect the material volume of the machine, the material cost of the device, and the overall cost of the wave-energy conversion system.

This thesis is structured such that the development of thought is clear to the reader:

Chapter 2 discusses the distinction between sustainable, renewable, non-sustainable and non-renewable energy forms. The availability of various energy resources is presented, leading to the quantification of the wave-energy resource. The mechanics of ocean waves is presented along with how technology may be used to extract energy from the waves. The peculiar application of linear generators to wave-energy conversion is presented, as well as a background to the field of linear machines.

Chapter 3 provides an introduction to the proposed machine layout. Some preliminary design considerations are discussed in terms of the stator and translator designs. Given the nature of the application, some magnet array topologies are not viable, and are eliminated at this point from further discussion. The nuances of the stator winding configuration are discussed which affects the application of present linear machine theory to this specific layout.

Chapter 4 details the mathematical description of the double-sided tubular machine. Initially, the analytical modelling of the magnetic and ferromagnetic materials is presented. The relationship between the mechanical power delivery of the waves and the electrical power absorption of the generator is discussed. This is followed by a detailed derivation of the electromagnetic force capability of the generator. The magnetic circuit of the active flux is presented along with derivations for the magnetic saturation and slot leakage factors which linearly reduce the electromagnetic force capability. Two design objectives are dis-

cussed along with the design algorithm and methodology.

Chapter 5 begins with the results of the Finite-Element Analysis (FEA) of the AWS' double-sided flat machine. The suitability of the techniques employed in the analysis of the FEA results is confirmed through the comparison of the analysed data with the expected results from published information. The chapter continues with the validation of the performance calculations through the simulation of two full-scale designs. These designs were intended to match the performance of the AWS' machine. Finally, the results of the prototype testing are presented to provide a measured validation of the accuracy of the performance equations which were developed in this research.

Chapter 6 summarises the results of the research. A comparison is presented between the double-sided flat and double-sided tubular layouts. This is based on the full-scale simulations of Chapter 5. Recommendations are made in terms of the mechanical and magnetic considerations which should follow in further research.

Appendix A documents all the design, simulation and analysis scripts which were used in this research. **Appendix B** presents a brief derivation of the general solutions to Laplace's equation in cylindrical coordinates, with particular application to tubular linear machines. **Appendix C** provides further details on the suppliers, parts and construction procedure employed in the assembly of the prototype machine.

Chapter 2

Background Research

¹In the beginning, God created the heavens and the earth. ²The earth was without form and void, and darkness was over the face of the deep. And the Spirit of God was hovering over the face of the waters. ³And God said, “Let there be light”, and there was light.[2]

Introduction: *The creation of the universe in the Holy Bible is an account of the beginning of energy and matter. Modern physics provides analytical descriptions of the mechanisms which were more than likely at play in the creation. Albert Einstein’s theory of energy-matter equivalence, $E = \gamma mc^2$, and the possibility of the universe originating from an infinitesimally small point, under the forces of a massive explosive power, are descriptions of the creation through a convergence of energy at this point, and the subsequent creation of matter from this energy. The cosmos exhibits energy in various forms. On earth we are exposed to all of them, either directly or indirectly. We have been able to use some forms more readily than others. How has our utilisation of the energies available to us shaped our present and how will our future utilisation of these energies shape our future? This chapter documents the energies available to us, our present utilisation of said energies, and why ocean-wave energy is a favourable component of the future energy mix. The extraction of energy from ocean waves is discussed, followed by the application of linear generators to wave energy conversion.*

2.1 Energy as a Resource

The universe contains energy in various forms including heat, gravitational, mechanical, electromagnetic, nuclear and chemical[3]. The laws of thermodynamics dictate that energy not only has a quantity, but a quality, dubbed entropy[4], which is a measure of the disorder of the energy form. In all interactions, energy *must* flow in such a manner that the entropy of the system is increased. Thus energy of a high quality (low entropy), may be degraded into a form of a lower quality (higher entropy). The reverse flow would reduce the entropy

and is thermodynamically invalid[4]. Table 2.1 lists the entropies of different forms of energy in the universe[3].

Table 2.1: Entropies of Energy Forms Present in the Universe[3].

Form of Energy	Entropy per Unit-Energy [Inverse Electron Volt]
Gravitational	0
Rotational Motion	0
Orbital Motion	0
Nuclear Reactions	10^{-6}
Internal Heat of Stars	10^{-3}
Sunlight	1
Chemical Reactions	1 – 10
Terrestrial Waste Heat	10 – 100
Cosmic Microwave Radiation	10^4

The predominant energy in the universe is gravitational, and is among the highest quality energy forms, as is evident from Table 2.1. This energy is degraded into all other forms of energy which are present in the universe. The purity of the zero-entropy gravitational energy may be appreciated by the high efficiencies achievable in hydro-electric power systems. The losses in hydro-electric power systems are attributable to the mechanical and electrical losses of the equipment, and are not inherent in the energy conversion itself.

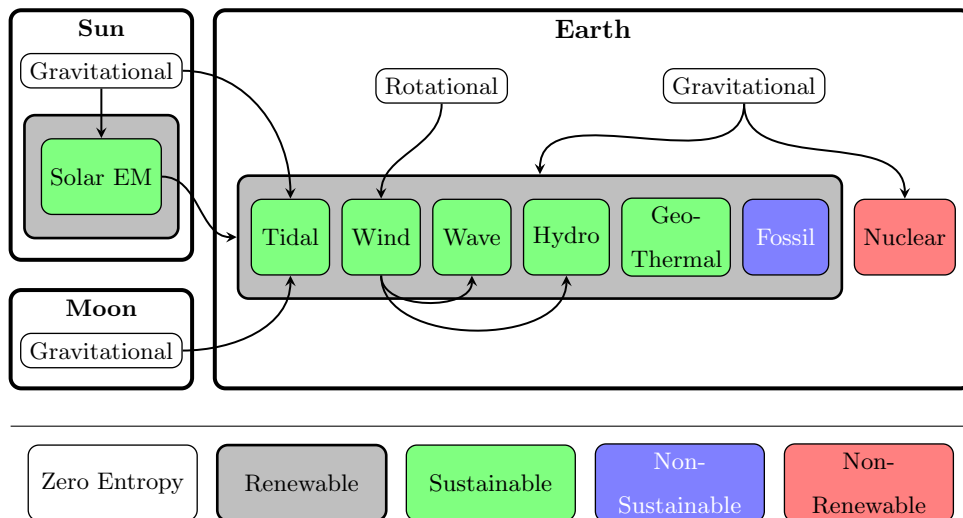


Figure 2.1: The Relationship between the Various Forms of Energy.

Consider Figure 2.1 which illustrates the universal energy flows which have in the past,

and presently do affect the energy which is available to us. The formation of the sun through gravitational energy resulted in the creation of nuclear fusion energy, which in turn has resulted in the electromagnetic and heat energy which we receive from the sun. The formation of the Earth through gravitational energy resulted in the creation of nuclear and chemical material. The interaction of the Earth's gravitational energy and the electromagnetic energy from the sun results in fossil fuels (oil and coal) and wind, wave, hydro and geo-thermal energy. Finally, the interaction of the gravitational energies of the sun, moon and earth are exhibited in the tidal swings of the oceans.

Only nuclear fuels are non-renewable as no mechanism on Earth naturally regenerates nuclear fuel. Contrary to popular definition, fossil fuels are renewable. The interaction of the chemical, solar and gravitational energies in the system provides a mechanism for the replenishment of these fuels. This is illustrated in Figure 2.2 in the form of the energy balance for fossil fuels[3].

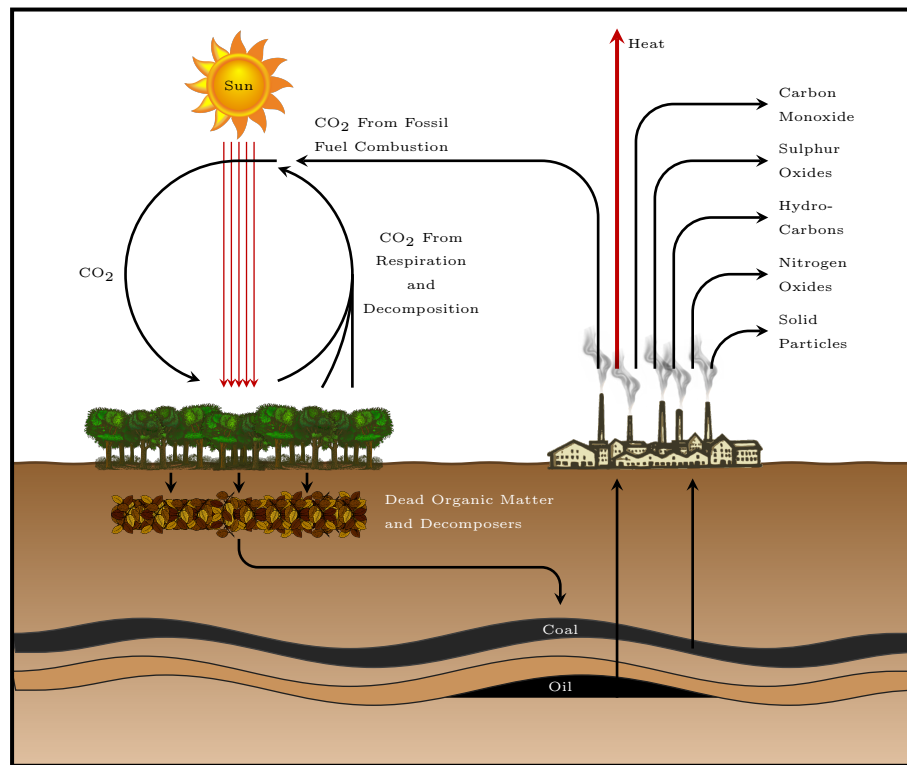


Figure 2.2: The Energy Balance for Fossil Fuels in the Earth's Crust[3]. Contrary to popular definition, fossil fuels are renewable.

Photosynthesis is the means by which plants grow. Oxidation is prevented in some of the dead organic matter by virtue of the conditions under which it is buried. In such circumstances, the organic material undergoes chemical changes which convert it into fossil fuels in the forms of oils, coals and natural gasses[3].

Figure 2.2 shows that plants require carbon dioxide for respiration. Oceans are also able

to absorb carbon-dioxide present in the atmosphere. There does exist a capacity for the biosphere to support additional carbon-dioxide levels. The limit to this capacity is termed the bio-capacity[5] and is a non-linear function of the state of the entire system. Mankind is actively retarding the bio-capacity of the Earth through deforestation, over-population, pollution, and resource exploitation. In this way we are crippling the Earth's ability to maintain an equilibrium. The most prominent symptom of this loss of equilibrium is the change in the global climate, which has made climate patterns more extreme across the globe.

Even though these fossil fuels are renewable by definition, human activity has made their continual usage non-sustainable. The distinguishing factor between the two is the rate of use versus the rate of regeneration and supply. Not only will our present rate of use deplete the reserves the Earth has of these fossil fuels in not-too-distant future[6], but our usage of these fuels will place enormous stresses on the ecological systems. The environment does not have the capacity to naturally sequester the green-house gasses in the form of fossil fuels at the same rate at which we are providing these gasses through our combustion of fossil fuels.

At present, the energy used by people is split between industry, automotive and commercial/household usage in the ratios of 40%, 25% and 35% respectively[7]. The World Energy Conference sanctioned a research study in the 1980's in an attempt to answer the question: "Is there, or is there not, a danger that some day our energy supplies will run out?"[6]. The conclusion of the report is undoubtedly "Yes!". The energies under consideration were those in common use in the 20th century, namely coals, oils and natural gas. These are the primary fuels of the modern age.

The 2004 survey by the World Energy Council on Energy Resources highlights the state of our energy reserves and utilisation as of end-2002[8]. In quantifying these reserves, some subjective definitions arise as to what is commercially extractable. The World Energy Council gives definitions as to these levels of reserves, which are shown in Figure 2.3 and are defined as follows[8]:

- Proved Amount in Place – "The resource which remains in known deposits that have been carefully measured and assessed as exploitable under present and expected local economic conditions with existing available technology."
- Proved Recoverable Reserves – "The tonnage *within* the proved amount that can be recovered in the future under present and expected local economic conditions with existing available technology."
- Estimated Additional Amount in Place – "The indicated and inferred tonnage additional to the proved amount in place that is of foreseeable economic interest. It includes estimates of amounts that could exist in unexplored extensions of known deposits or in

undiscovered deposits in known [resource-bearing] areas, as well as amounts inferred through knowledge of favourable geological conditions. Speculative amounts are not included.”

- Estimated Additional Reserves Recoverable – “The tonnage *within* the estimated additional amount in place that geological and engineering information indicates with reasonable certainty might be recovered in the future.”

Other sources include the categories of “Speculative” and “Ultimate” reserves which extend successively beyond the boundaries of the Estimated Additional Amount in Place[6].

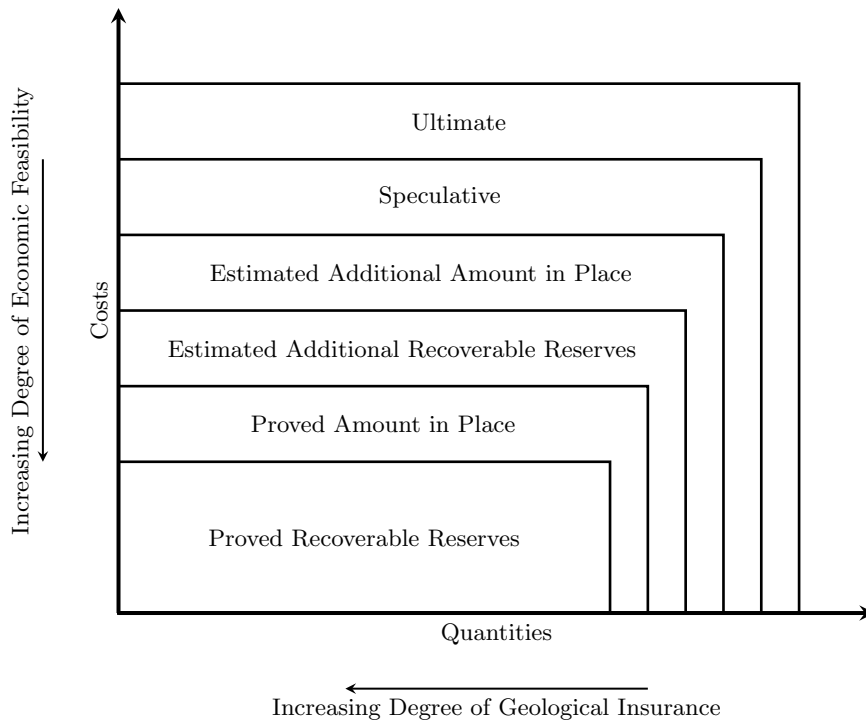


Figure 2.3: Classification of Reserves, as Defined by the World Energy Council[8] and World Energy Conference[6].

Table 2.2 presents the figures of the 2004 World Energy Council report. The years remaining for each fuels type is based on end-2002 production levels. It is evident that there are still significant reserves of coal, which is the main fuel for electrical generation. Crude oil and natural gas on the other hand have a very short life ahead, being depleted within fifty and one hundred years respectively. In the special case of Uranium production, advances in breeder reactors will advance the nuclear cause[7]. This is because they utilise the Uranium more completely, and are thus more fuel-efficient, and are able to use reprocessed, spent-fuel instead of freshly mined Uranium. Thus the yield per unit of Uranium fuel may be increased.

In all resource mining operations, there exists a concept of peak-production. In essence, this suggests that, given a certain amount of a resource, there exists a production curve

Table 2.2: Global Proved Recoverable Reserves and Production Rates (end-2002)[8].

Resource	Units	Proved Recoverable	Production (end-2002)	Years Remaining
Coals	10 ⁶ Tonnes	909 064	4 823	188
Crude Oil & NGL	10 ⁶ Tonnes	148 342	3 509	42
Oil Shale	10 ⁶ Tonnes	487 602	578	844
Extra-Heavy Oil	10 ⁶ Barrels	48 354	205	236
Natural Bitumen	10 ⁶ Barrels	247 277	275	899
Natural Gas	10 ⁹ m ³	170 531	2 684	64
Uranium	10 ³ Tonnes	3 169	36	88

which increases rapidly, reaches a peak and then enters decline. The late Mr. Marion King Hubbert, a geo-scientist from Houston, Texas in the USA, developed a model for peak oil production as part of his research at the Shell research labs[9]. The production curve approximates a normal distribution, or bell-curve, but is its own distinct logistical curve. All mined resources will experience some form of production peak and subsequent decline in production. Whether or not we have already passed the peak for any of the primary fossil fuel sources is a hotly-debated topic. However, if we are not there yet, then we are surely close, and regardless of the timing, the eventuality is certain.

Based on these figures, we are likely to run out of fossil fuels before long, as was the conclusion of the World Energy Conference[6]. However, the biosphere would have already lost equilibrium before we have depleted these reserves, and so the argument is slowly moving from “Do we have enough?” to “Can we ecologically afford the continued use of fossil fuels?”.

Enter the sustainable energy resources. These are by definition sources of energy which mankind can utilise at a rate which is less than the rate of their supply. From Figure 2.1 one may recognise these as:

- Solar Energy
- Wind Energy
- Wave Energy
- Geo-thermal Energy
- Hydraulic Energy, and
- Tidal Energy

The primary energies which drive these systems are the gravitational energies of the sun, moon and earth, the rotational energy of the Earth, and the electromagnetic solar energy. Sustainable energies are typically more complex to utilise and more expensive to extract energy from when compared to fossil and nuclear fuels. This is because they have lower energy densities than the non-sustainable resources. It is interesting to note that in Genesis, God made the earth, moon and the sun before any life. Is it a philosophical truth that these resources are the only ones that can sustain life on Earth?

Figure 2.4 illustrates the relative contributions of these energies to the Earth's energy mix. Obviously, we could not extract excessive portions of these energies to meet our own requirements without adversely affecting the environment once again. This is because those energy sources drive natural, non-linear systems on Earth. Removing energy from these sources will prejudice the systems that rely on them. Even though the entire world's energy usage is significantly smaller than these supplies, by many orders of magnitude, sensitivity to the environmental influences of our actions must not be abandoned. No single source is the most appropriate to "solve" the world's energy problems. The most feasible solution is one in which there exists a mix of different sources, such that no single system is affected too severely.

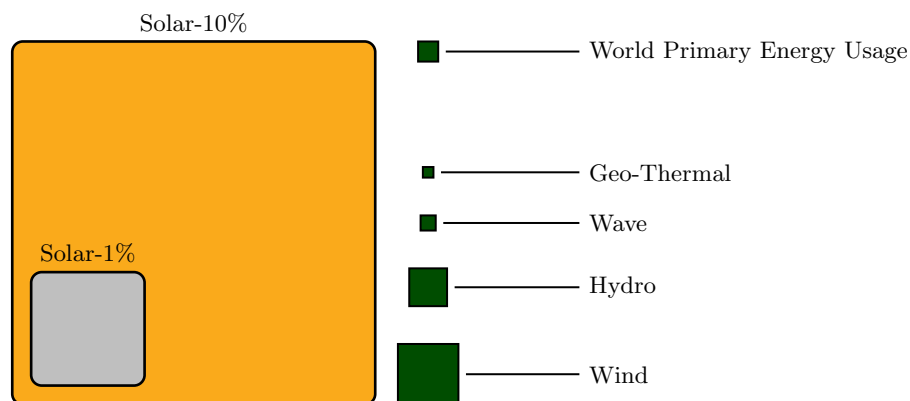


Figure 2.4: The Relative Energy Content of the Various Sustainable Resources. The exact figures used are shown in Table 2.3

Mankind must also realise that although the resource is large, the present economic theories of unrestricted growth are in themselves non-sustainable. Unrestricted growth in economies requires unrestricted resources. This will result in the bio-sphere being stressed, even with the use of sustainable energy solutions. The bio-capacity is not just a measure of the environments sustainability in terms of energy, but also in terms of land, water and mineral resources[5]. It is evident that most of the developed world is operating beyond the bio-capacity of their respective regions. The holistic solution in terms of bio-capacity limitations is conservation of resources and reduced populations. Conservation in the energy

context is the cheapest form of incremental “new” energy[3]. Thus future energy is a double-edged sword: sustainability from conservation and from sustainable resources.

The greatest challenge facing sustainable energies is the dispatchability of the recovered energy. Technologies exist to extract energy from the resources, but the supply profile rarely matches the load profile. These resources are not only cyclic in nature but spectral. Thus base-load performance is not achievable unless suitable storage mechanisms can improve the dispatchability of these systems.

Two notable exceptions to this are geo-thermal and hydro-electric power. Both may be operated as base-load supplies and are less susceptible to the transients of the surrounding environment. This is because they are situated within systems which exhibit large time-constants, which essentially filters out the disturbances of the prevailing environment. This may be considered an environmental inertia which helps stabilise the resource.

Table 2.3 provides a quantitative assessment of the sustainable energy resources. The total incident energy per resource is often quoted as the entire energy content of the resource across the entire Earth. It is not feasible to extract the full energy content of a resource and so the figures presented represent more realistic approximations of the resource. In matching the requirements of power generation to the resources, the capacity factor and the energy density are important.

Table 2.3: The Energy Content of the Various Sustainable Energy Resources, as Reported by the World Energy Council[8], Hartnett[7], Lomborg[10], Brooke[11], Sergeant & Lundy[12], Thorpe[13], EPRI[14], REN21[15], Archer and Jacobson[16] and Wikipedia[17]. Solar has two cases, showing the percentage of unused land in the world on which the solar energy may be extracted. Data which is either unavailable or not applicable is shown as a hyphen.

Resource	Energy [TWh/yr]	Energy Density	Installed Capacity [GW]	Capacity Factor
Solar (10%)	13 840 000	170 [W/m ²]	13.5	25%
Solar (1%)	437 500	170 [W/m ²]		25%
Hydro	15 899	-	945	46%-60%
Geo-Thermal	300	-	10	73%-90%
Wind	62 802	400 [W/m ²]	121	20%-40%
Wave	750	50 [kW/m]	-	30%-45%
Tidal	-	-	0.3	30%
World Energy Usage	118 055			

The solar radiation is the primary source for the other sources of energy. As such, it has

the lowest energy density out of all the resources. As the energy is imparted on the systems of the Earth, such as wind patterns and hydro cycles, the energy tends to be naturally concentrated[8]. The extent to which the energy is concentrated varies according to the system. If the solar radiation may be termed the first generation resource, then subsequent generations tend to exhibit higher concentration factors.

Wave energy, being a third generation resource, has a relatively high energy density. The waves are generated by the action of the prevailing winds across the oceans. The prevailing winds are generated by the differential heating of the Earth's surface by the solar radiation, combined with the Coriolis effect of the air migrating across the latitudes (the Earth's rotational energy). Wind energy exhibits higher energy densities than solar energy, but lower densities than ocean wave energy. An initial annual average solar energy density of 100 W/m^2 will typically be concentrated into an annual average of 10-50 kW/m of incident wave crest[11], depending on the location. The peak values of wave energy can reach 1000 kW/m versus a solar energy peak of roughly 1 kW/m^2 [8].

The oceans are also large expanses which are acted on by different wind systems at different points. This gives ocean wave energy an environmental inertia which stabilises the resource, as with hydro and geo-thermal power. Thus, ocean wave energy is an attractive prospect for future sustainable base-load power[18]. It is less dependant on the transient local environmental conditions, and is of a relatively high concentration.

2.2 Wave Energy Conversion

Wave climatology at any geographic location is largely dependent on the prevailing wind systems. These are the Polar Easterlies, the Prevailing Westerlies and the Trade Winds. Other wind systems including monsoons and tropical storms affect the energy content of the ocean, but it is their transient impact that make it impractical to consider them as consistent sources of wave energy.

Figure 2.5 presents the annual global average wave energy distribution based on empirical data that has been collected regarding the energy content in the oceans. The wave energy is typically greater in regions which are exposed to larger wind tracks than in regions that are buffered from any significant wind track.

The commercial exploitation of ocean wave energy is affected by the energy intensity at the point of generation. The lower limit for commercial feasibility has been estimated at 20 kW/m of incident wave front[19]. This is a relatively low intensity, given that the highest values are roughly 100 kW/m . The economics of any system becomes increasingly attractive with increasing energy intensity. It is the extensive resource that has resulted in the birth of numerous wave-energy conversion technologies. The nature of the environment however, and the technical limitations of these systems, has made the economic prospects

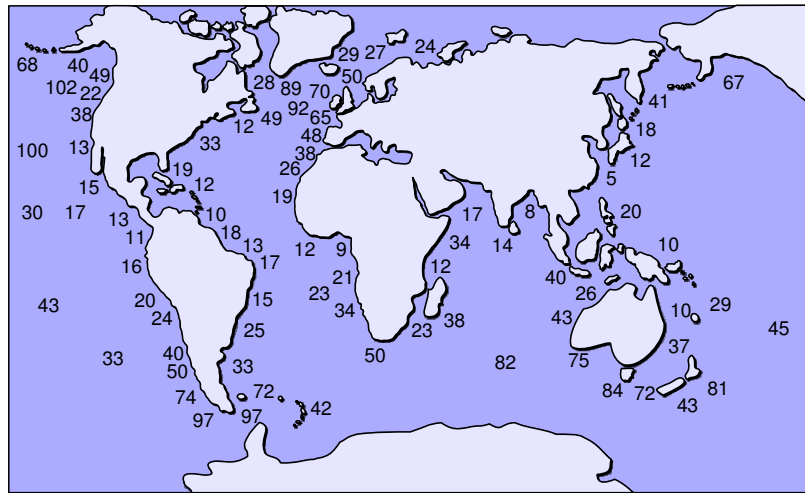


Figure 2.5: Annual Global Average Wave-Energy Densities Given in Kilowatts per Metre of Incident Wave Crest[8]. Economic viability is achieved at values above 20 kW/m. The distribution of energy in the ocean is largely due to the wind track and prevailing winds.

of wave-energy conversion uncertain. Without a definitive technical solution, the business risks are often perceived as too high given that most systems are still experimental.

2.2.1 Wave Mechanics

“A bit of gossip starting in Washington reaches New York [by word of mouth] very quickly, even though not a single individual who takes part in spreading it travels between these two cities. There are two quite different motions involved, that of the rumour, Washington to New York, and that of the persons who spread the rumour. The wind, passing over a field of grain, set up a wave which spreads out across the whole field. Here again we must distinguish between the motion of the wave and the motion of the separate plants, which undergo only small oscillations... The particles constituting the medium perform only small vibrations, but the whole motion is that of a progressive wave. The essentially new thing here is that for the first time we consider the motion of something which is not matter, but energy propagated through matter.”[20]

This excerpt highlights an important distinction to be made in wave mechanics: the distinction between the motion of the wave, and the motion of the medium through which it progresses. One must distinguish between the motion of the ocean wave and the motion of the water particles through which the wave moves.

As wind moves over the water surface, the air imparts some energy on the surface water particles through friction. This creates small capillary-waves whose primary restoring force is the surface tension of the water. The wavelength of these waves is typically less than

1.73 cm. As more energy is transferred from the wind into the water, the waves become more pronounced. The restoring force in these larger waves is the force of gravity and are aptly termed gravity-waves[21].

The energy imparted on the water manifests itself in the orbital motion of the water particles. The shape of the resultant wave is trochoidal. This is defined as the shape traced out by a point on a circle as the circle is rolled along a line[22]. This shape is illustrated in Figure 2.6 a) and features a more pointed crest, and an elongated trough. For gravity-waves with significant wavelengths, such as offshore swells, the shape of the trochoidal wave approaches that of a sinusoid, which is shown in Figure 2.6 b).

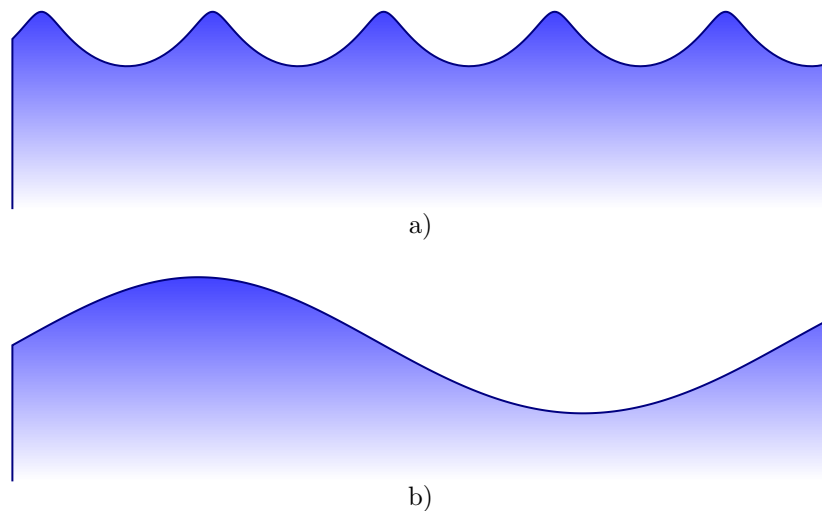


Figure 2.6: Oceans waves are shaped like trochoids. a) For short wavelength waves, including capillary-waves, the wave exhibits a more pointed crest and an extensive trough. b) For longer wavelengths, including off-shore swells, the shape of the trochoid becomes more symmetrical and may be approximated by a sinusoid.

The energy transferred from wind to water is transferred further between the particles of the subsequent layers of water below. The energy in each subsequent layer is less than the one above because of frictional losses in the water. The result is that the amplitude of each successive trochoid is diminished and the radius of the orbital paths of water particles is exponentially reduced with depth.

At roughly half a wave-length, the orbital motion is less than 4% of the surface orbital motion. This depth is referred to as the wave-base, the point below which the wave motion is unable to affect a significant water particle motion. Figure 2.7 shows this distribution of the energy in off-shore ocean swells. At ocean depths deeper than the wave-base, very little energy is lost to the sea bed through friction. These swells can travel for extended distances without significant attenuation.

As waves approach shallower water (ie: when the depth is approximately half of one

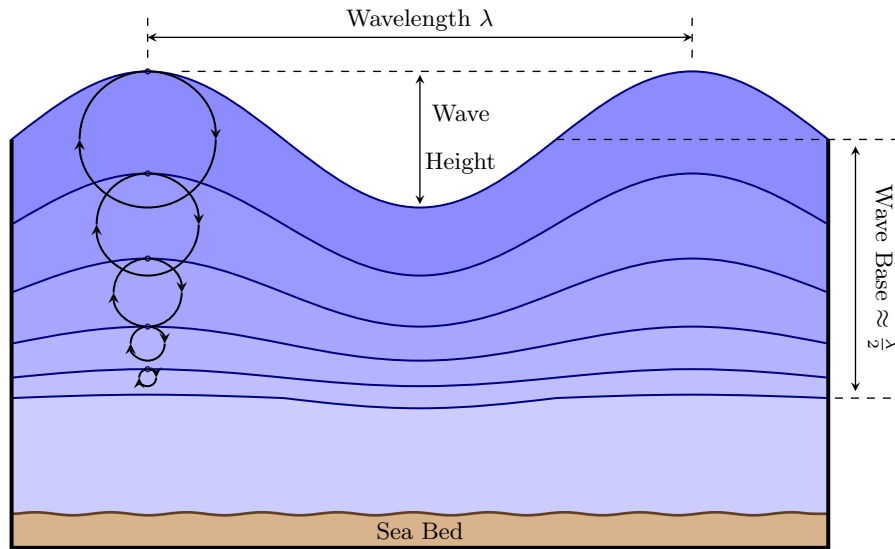


Figure 2.7: The energy in ocean swells reduces exponentially with depth. At a depth of roughly half a wavelength, the energy content is less than 4%, a point which is defined as the wave-base. The orbital motion of the water particles is shown to decrease with increasing depth. This is because of the reduced energy content with depth.

wave-length), the sea bed begins to act on the wave. The result is a dissipation of the energy in the wave through friction, shoaling and breaking. Thus it is advantageous to extract energy from the ocean before the any energy is lost to the sea-bed.

The above description of ocean wave mechanics is based on monochromatic waves. In the ocean, waves have a random height, period and direction. The energy content is spectral by nature. Several models have been developed to quantify the ocean's energy spectrum, the most common of which is the JONSWAP spectral model, named after the Joint North Sea Wave Project[11]. The typical frequency range of random ocean waves is between 0.04 Hz and 0.25 Hz, or periods of 25 s to 4 s respectively. The distribution is similar in shape to that of Max Plank's curve describing block-body radiation, the peak of which is focussed about the frequency of 0.1 Hz (10 s period).

In order to achieve economic viability, wave energy must achieve generating costs which are at least comparable to that of wind energy. In the medium-term, wave energy will need to achieve grid parity in order to be economically viable. In 2003, a study was conducted into the likely operating costs of mature wave-energy devices, arranged in suitable arrays in areas of promising wave activity[23]. The study concluded that a number of devices have the potential, once mature, to generate electricity at between one to two times the grid cost of power, including operation and maintenance costs. The World Energy Council indicates that the cost of energy from prototype installations is likely to be two to three times the cost of energy from mature, commercial installations[8].

Similar experiences have been the case for other technologies through their development cycles, most notably wind energy, which has experienced roughly a ten-fold reduction in the cost of production over the past few decades[8]. Besides the reductions attributable to the migration from prototypes to commercial offerings, the factors which have contributed to these reductions include[8]:

1. The increasing scale of the wind turbines which has decreased the cost per installed kW, owing to the economies of scale,
2. The improved and more efficient manufacturing techniques which have matured with the technology,
3. The optimised field designs which have improved the annual yields per turbine, and
4. The reduced maintenance costs.

The first two factors are characteristics of industrialisation while the latter two are related to the improved design of the turbines and their application. Wave energy converters share these opportunities for cost reductions: the industrialisation will lead to lower costs per device, and the improvements in converter and field designs will lead to reduced maintenance costs and higher yields per device.

The increase in the installed capacity of wave-energy converter systems would be positively influenced by the implementation of appropriate feed-in tariffs and incentives which would help to offset some of the research and industrialisation costs. This has been the case with solar power systems[8]. In Spain, for instance, the *Instituto para la Diversificación y Ahorro de la Energía's* (IDEA) was approved by the Spanish government in December 1999. It set out a programme for the development of solar thermal and solar photo-voltaic systems. This led to massive investment in solar technologies, and has moved the industry from pilot plants to commercial installations, significantly contributing to the maturity of the technologies and reducing the levelised electricity costs. One possible obstacle for wave-energy conversion systems, in terms of the implementation of such incentives, is the variety of solutions on the market with no definite technology leader.

2.2.2 Wave Energy Conversion Technology

The exploitation of wave energy is not a new concept. Various 19th century proposals call for the conversion of wave energy to perform mechanical work. An example of a modern practical, application of wave-energy conversion is found in the use of wave-energy to power navigation buoys. This application was based largely on the pioneering work of Yoshio Masuda, leading to many thousands of wave-powered navigation buoys being developed since 1965[11].

The amount of energy absorbed is largely dependant on the axes of freedom in which the device operates. This is because ocean waves have a three-dimensional power vector. An ideal system should absorb energy from all three dimensions along which the wave-front delivers energy. The effectiveness of each type of system to absorb energy is thus limited by the designed axes of freedom.

Conversion of the incident wave-energy into an appropriate form of useful energy for man involves two important stages. Firstly, the energy must be absorbed by some mechanical device. The second stage involves the power transfer system in which the energy absorbed by the device is converted into either some form of mechanical mass-flow (pumping) energy or into electrical energy, or a series coupling of the two to achieve an electrical output.

Energy Absorption Technology

The primary conversion stage absorbs the kinetic and potential energy of the wave-front. Many absorber techniques have been developed along with many means to classifying them. In essence all wave-energy absorption techniques require a form of absorber and a form of reaction point. The absorber will be acted on by the wave, while the reaction point will provide a reference according to which the energy is absorbed. Without the relative movement of absorber to reaction point, power-takeoff would not be possible.

Hagerman classifies the techniques according to three criteria whereby he has been able to define twelve distinct process variations[24]. The features that distinguish the various processes are the axis of freedom of the energy absorption, the type of absorber and the type of reaction point. This classification has been further extended and revised and is well documented by John Brooke[11].

The axes of freedom of absorption are pitch (an angular motion about an axis parallel to the wave-front), heave (vertical motion) and surge (horizontal motion perpendicular to the wave-front).

The absorber may be classified into either a rigid structure, flexible structure or a free-surface. A free-surface absorber is the water's surface itself, and is applicable when a differential water volume is used.

The type of reaction point is classified into inertial structures, sea-floor anchors and fixed structures. An inertial structure's mass prevents the perturbation's of the ocean waves from moving it significantly. An anchored structure is not free to move and provides a solid reaction point. Fixed structures include land and concrete structures. Off-shore absorbers employ either inertial or anchored reaction points; coastal devices will typically utilise a fixed reaction point.

Hagerman's classification is comprehensive, but not exhaustive. Instead of revisiting these classifications, and given the diversity of absorber technologies, the author has defined

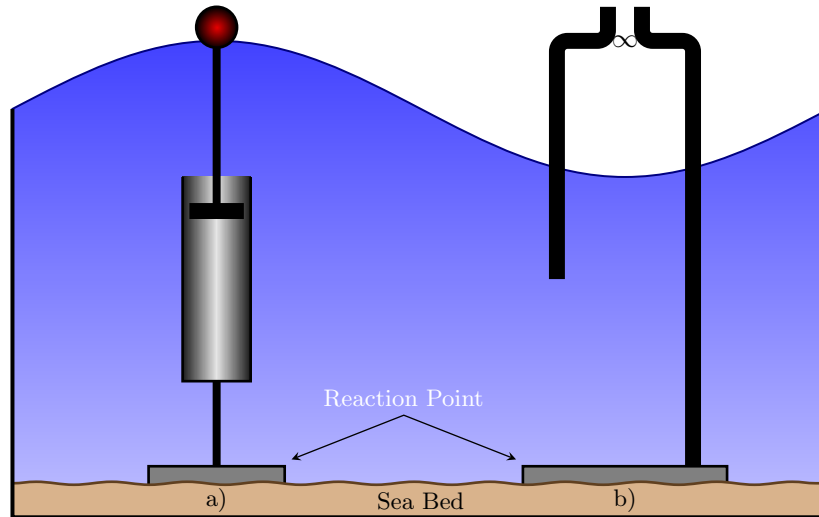


Figure 2.8: Absorbers may be classified into two broad categories: a) Devices which use the positional change due to the surface fluctuations of the ocean to drive the power transfer units. b) Devices which use a volumetric change in air or water to drive the power transfer units.

two fundamentally distinct types of absorber technologies.

The first technology is based on a positional change of the absorber as a result of the wave action. The absorber is of either the rigid or flexible type. The primary example of a position-based system is the buoy which floats in relation to fixed point below the water's surface, as shown in Figure 2.8 a).

The second technology is based on a volumetric displacement of either air or water. The absorber is typically the free-surface of the water. An example of a volume-based system is an oscillating water or air column, as shown in Figure 2.8 b).

The primary advantage of volumetric absorbers over positional absorbers is the natural gearing affect that may be achieved through either pneumatics or resonant buoyancy. Oscillating water columns (OWC) are examples of pneumatic gearing which is inherent in the operating philosophy of an OWC. The Archimedes Wave SwingTM (AWS) is an example of a resonant buoyancy system[1], and is shown in Figure 2.9.

In a resonant buoyancy system, a volumetric change in the amount of water above the device affects a change in the force applied downwards on the device. By controlling the buoyant force of the chamber, the system is made to resonate with the frequency of the waves above. In this fashion, a small perturbation of 1 m on the water's surface results in an amplified motion of the chamber of up to 7 m, thus affecting a naturally geared system, in a linear sense. This natural gearing is of importance to the design of the power transfer system.

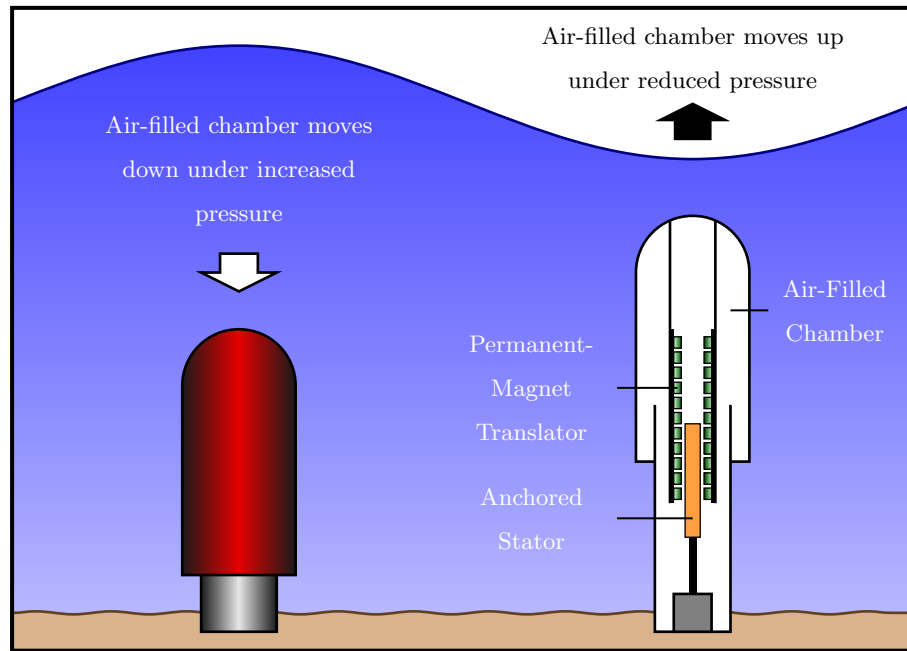


Figure 2.9: The Archimedes Wave Swing is an example of a resonant buoyancy system[1].

Power Transfer Technology

The energy absorbed by the absorber system must be used as either mechanical energy, or converted into electrical energy. This will typically involve driving either a pump or generator respectively. Both these types of loads will require an actuation frequency which is higher than that of the frequency of the waves.

In order to achieve this frequency increase, a form of gearing is required. Various techniques have been devised to achieve this frequency shift and have been extensively documented[11]. Hydraulic systems are the best proved technology for mechanical power transfer and gearing. In such a system, the pump/generator is driven indirectly by the absorber, through the hydraulic system.

Indirect-drive systems present a significant advantage in terms of being able to locate the mechanical load (pump or electrical generator) on-shore. This makes maintenance less of a problem. The associated disadvantage is that the system suffers from parasitic losses in the transmission of the working fluid, and is thus typically limited to near-shore applications.

In the case of natural gearing of the absorber, a direct-drive system may be employed. Direct-drive systems eliminate the transmission stage of wave-energy conversion. The reciprocating absorber is coupled directly to the generator. The efficiency is thus increased because of a lack of hydraulic or gearing losses. The associated reduction in system complexity may also result in a reduction in the maintenance requirements. However, the issue of off-shore generator maintenance becomes problematic.

The configuration of generators driven directly by a naturally geared volumetric absorber

system tend to oscillate linearly. Their design is based less on the axes of freedom of the incident waves, and more on the force variations in their primary axis with variations in water volume. This configuration lends itself to the application of linear electrical generators, coupled directly to the absorber system[25].

2.3 The Application of Linear Generators to Wave-Energy Conversion

A linear machine may be visualised as a rotary machine, cut along its axial length, and rolled out to form a linear machine. Linear machines may be designed in any of the common electromagnetic designs, or a combination thereof:

- Induction Machine
- Reluctance Machine (Switched/Synchronous/Stepper)
- Synchronous Machines (DC-Field/Permanent-Magnet)

All linear machines, regardless of the electromagnetic design, may be classified according to their topology:

- Flat (planar) or Tubular (cylindrical) Layout
- Single- or Double-Sided Flat Layout
- Slotted- or Slotless-Armature
- Ferromagnetic- or Air-Cored
- Transverse- or Longitudinal-Flux

The definitions and characteristics of the different linear machine topologies is discussed in detail in the literature[26]. Of particular importance to the present research is which topology is most appropriate for wave-energy conversion. In order to properly answer this question, the high-level design criteria are necessary.

Direct-drive systems, which are to be installed off-shore, are primarily cost and maintenance sensitive in their design. In order to achieve grid-parity, both capital and maintenance costs must be reduced. The following high-level requirements must be met in the design of the generator:

- A Small Size - This affects the capital cost, weight and maintenance efforts.
- A High Power Factor - The cable feeding the grid from offshore would be poorly utilised if the generators provided power at a poor power factor.

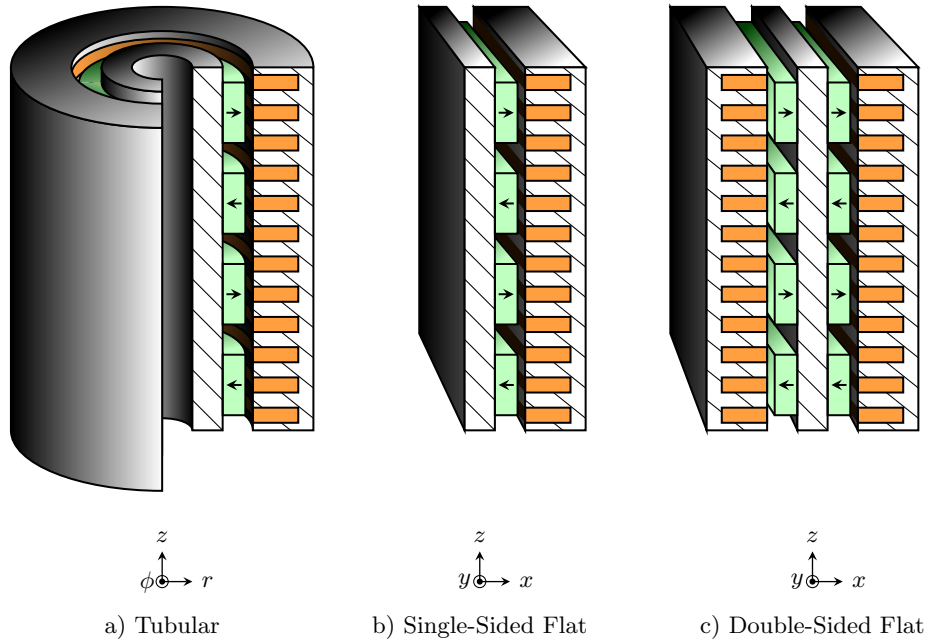


Figure 2.10: Tubular and Flat Linear Machine Layouts.

- A Smooth Motion - The more abrupt the motion of the translator, the more wear the bearings experience.

A number of studies have been conducted to consider the relative merits of various topologies and electromagnetic designs[27]. In the literature, double-sided flat layouts were used so as to balance the attractive forces between the stators and translator. Both ferromagnetic and air-cored systems were tested. An additional study has researched the merits of a tubular slotless design[28].

An illustration of the published linear machine layouts is shown in Figure 2.10. The particular layouts shown illustrate the use of slotted ferromagnetic cores and surface-mounted permanent-magnets, which are applicable to the present research. The following observations were made in the literature regarding the various topologies:

- Designs without ferromagnetic slots eliminate the reluctance force component, but exhibit a lower force density, and poor material utilisation.
- Transverse flux machines have higher force densities and sheer forces, but the harmonic content of the force distribution produces a rough motion, which is not suitable in terms of maintenance. These machines are also more complex in terms of the mechanical design, and the power factor is very low at roughly 0.3.
- The highest power factor is exhibited by permanent-magnet synchronous machines at greater than 0.9. Although they do not provide the same force density as the transverse flux machines, the translator motion is smoother.

The available literature suggests that the most appropriate electromagnetic design for ocean wave-energy conversion is the permanent-magnet synchronous machine. This is primarily because of the smooth operation, high power factor and suitably high force production. Indeed, most designs to date, which have been piloted, have been of this design, including the AWS' machine. Although the slotless design eliminates the reluctance component of the force, it requires a significantly larger machine, which bring them into conflict with the design objectives. Thus slotted machines are most suitable for the application.

The literature does not discuss the characteristics of flat versus tubular layouts for the particular application of wave-energy conversion. However linear machine theory indicates the following characteristics of the two layouts[26]:

- Double-sided flat layouts provide a higher force density than single-sided designs. The two stators also help stabilise the transverse forces in the machine generated through the attractive forces of the stators to the translators.
- Tubular machines encapsulate the flux more completely. Unlike flat designs, there exist no transverse edges from which flux may leak. Thus the flux utilisation of tubular machines is better than that of flat machines. This results in a better utilisation of the permanent-magnet material.

Linear generator designs are able to satisfy the design criteria of direct-drive systems in all the aspects save one: size. The low actuation speed means that the induced *emf* in the stator windings is low. This combined with the requirement for the machine to oppose very high linear forces, imposed by the waves above, means that the electrical current in the machine is high. A high electrical current results in a larger machine.

The superior flux-utilisation in a tubular machine means that less permanent-magnet material is required per unit of force-capability. The double-sided flat layout reduces the size of the machine through sharing magnetic material between the two stators.

The hypothesis of the present research is that a combination of the double-sided and tubular machine would result in a smaller, and hence more cost-effective machine, which uses less permanent-magnet material than that of an equivalently rated double-sided flat machine.

2.4 Conclusions

There exist various forms of energy in the cosmos. Most of these energies are available to us in some form or another. Some of the forms of energy that we have at our disposal are renewed through natural cycles, others are limited and have no natural mechanisms for renewal. Of the renewable resources, only those that do not involve a chemical conversion to fossil-fuels are sustainable in light of our rate of usage. Solar-electromagnetic energy and gravitational energy are the primary resources from which all other renewable energies are transformed. The successive conversion of solar energy into wind and wave energy provides two significant advantages over the direct use of solar and wind resources:

- There exists a natural concentrating effect in the conversion from solar to wind and wind to wave energy, and
- The expanses over which the prevailing winds act are large enough to give wave energy a significant environmental inertia, thus filtering out the local weather transients at the point of extraction.

Ocean wave energy is thus a very well concentrated resource with the potential to provide sustainable base-load power, because of the environmental inertia. The energy in the waves is present in three axes of freedom. Thus effective energy extraction is very difficult. Many systems have been developed with varying levels of success.

The mechanics of wave energy are such that most absorber technologies are acted on in a reciprocating linear motion. This linear motion lends itself to the application of linear generators for direct-drive systems. These systems eliminate the power transmission stage used in other wave energy converters, improving efficiency and increasing the yield.

Linear machines come in various topologies and electromagnetic designs. The permanent-magnet synchronous generator is the most appropriate for wave-energy conversion because of the smooth motion, the high power factor and the favourable force capability of this electromagnetic design.

Double-sided flat layouts and tubular layouts have differing advantages: double-sided layouts reduce the material required by sharing the material between two air-gaps; tubular layouts improve the flux encapsulation thus resulting in a better utilisation of the permanent-magnet material.

Chapter 3

The Double-Sided Tubular Linear Machine

***Introduction:** Electric machines generate or absorb force through the interaction of the stator's magnetic field with that of the translator or rotor. The amount of magnetic flux in the air-gap is proportional to the surface area of the air-gap. The force capability is linearly proportional to the amount of magnetic flux linking the stator to the translator or rotor. In flat or tubular designs, the air-gap surface area is directly proportional to the cross-sectional size of the machine. An increase in force capability may be achieved by a proportional increase in the machine size. In tubular machines, this becomes especially wasteful. The air-gap moves further away from the axis of symmetry of the machine, and the volume becomes less well utilised. The present design of a double-sided tubular machine improves the machine's volume utilisation. The force capability is increased not by enlarging the air-gap, but rather by adding another air-gap to the machine. Although not limited to two air-gaps, the scope of this research is limited thus. The result of the dual air-gap design is a higher force density than a standard double-sided flat machine through the incorporation of the benefits of tubular machines. A conceptual illustration of the proposed machine layout is shown in Figure 3.1.*

3.1 Translator Layout

The design of the translator must consider the electromagnetic performance as well as the mechanical integrity. The electromagnetic performance may be quantified in terms of the force capability (FC) and total force ripple (TFR). The mechanical integrity may be quantified in terms of the tensile strength of the translator.

The three possible magnet array configurations are shown in Figure 3.2. The axially-aligned buried magnets produce very low harmonic content with suitable flux levels for

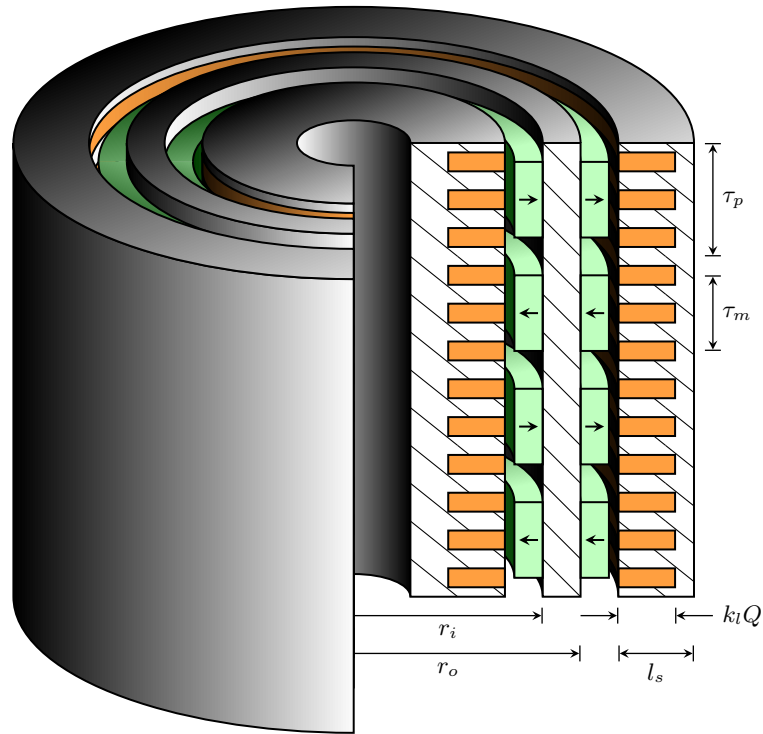


Figure 3.1: The double-sided tubular machine implements dual air-gaps, resulting in a higher force-density than other machine layouts.

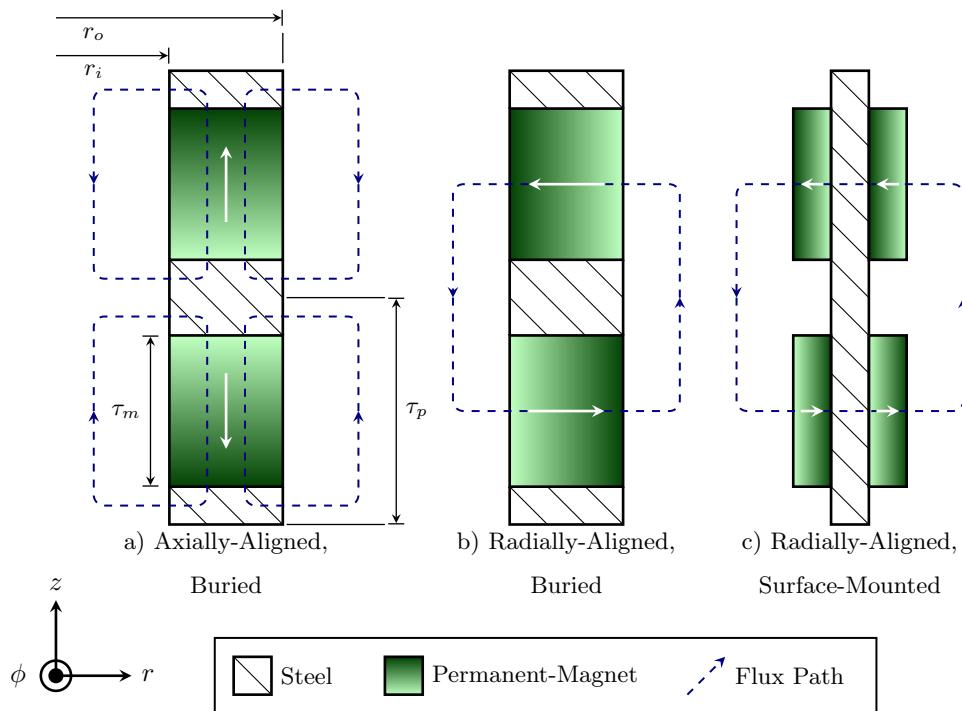


Figure 3.2: Permanent-Magnet Array Configurations, Shown per Pole-Pair.

use[29]. The radially-aligned buried magnets have slightly more harmonics than the former. Both these magnet arrangements possess very large salience.

Salience enhances the second harmonic of the force distribution. This increases the peak force capability of the device. In a low-maintenance environment however, this is not suitable. The large harmonic force components contribute significantly to the bearing wear and mechanical stress.

Another characteristic of these two designs is the relatively low mechanical strength of the magnet array over long translator lengths. The sections are stacked vertically along z . Rods are needed to run through the magnet and steel blocks to strengthen the stack. However, the length of the stack (translator length) is limited by the tensile strength of these rods. An increase in translator length, and hence weight, is accompanied by an increase in the rods' diameter, compromising the magnetic performance of the array.

A surface-mounted magnet array accounts for both of these issues. Firstly, the array is relatively non-salient because the magnets' permeability is comparable to that of air. Secondly, the mechanical support is a solid tube, gathering strength from its circular structure and its continuous form. Consequently, the most suitable magnet array is a tubular back-iron with surface mounted magnets on both the inner and outer surfaces, as shown in Figure 3.2 c).

The quantification of the force capability and total force ripple is based on the analysis of the machine which follows in Chapter 4. The magnetic flux density *in the air-gap* is composed of a fundamental and a sequence of space-harmonics. One may consider the Total Harmonic Distortion (THD) of this space-distribution, as given in Equation 3.1, to quantify the TFR, but this is not entirely accurate.

$$THD = \frac{1}{\hat{B}_1} \sqrt{\sum_{h=2}^{\infty} \hat{B}_h^2} \quad (3.1)$$

$$TFR \neq THD$$

The force production of the machine is a function of the magnetic flux which *links* the stator and translator. There are two mechanisms which affect the force ripple. Firstly, the design of the magnet array determines the magnitude of the individual harmonics of the magnetic flux density. The Fourier representation of the magnetic flux density in the air-gap, as shown in Figure 3.3, and resulting from the permanent-magnets, is:

$$\tilde{B}(z) = \sum_{h=1}^{\infty} 2|C_h| \cos(h\beta z + \theta_h) \quad (3.2)$$

where : $C_h = \frac{2B_{gmax}}{h\pi} \sin\left(h\frac{\alpha_m\pi}{2}\right) \quad \forall h \text{ odd}$

$$\theta_h = \angle C_h$$

It is evident from this representation that the magnitudes of the individual harmonics of the magnetic flux density are affected by the design of the permanent-magnet array only through the choice of α_m . This is the ratio of the magnet-pitch, τ_m , to the pole-pitch τ_p .

The second mechanism which affects the force ripple is the design of the stator windings. This determines to what extent the harmonics in Equation 3.2 link with the armature coils. The winding configuration may be designed to eliminate or minimise the influence of certain space-harmonics through the appropriate selection of the coil-pitch, τ_c . Consider Figure 3.3 which illustrates the fundamental and third harmonic of a permanent-magnet array.

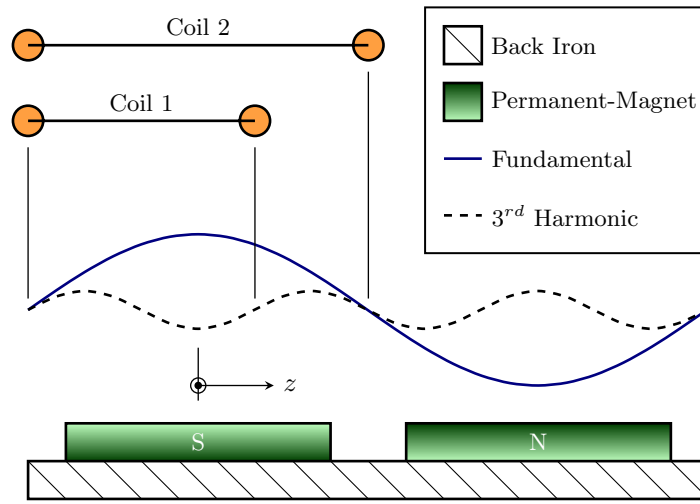


Figure 3.3: The winding factor affects the force capability and TFR. In this case, both coils experience a force from the fundamental component of the flux distribution, however, only coil 2 will experience a force component from the presence of the harmonic. For each coil, the relative impact of each harmonic in the flux distribution is different, leading to different TFR and force capabilities.

The space-harmonics which link the stator windings are limited by the space-distribution of the stator coils. For any given space-harmonic, the stator windings may be wound such that the coil-pitch is a multiple of the harmonic's period. This results in the total flux of this harmonic which links with the coil being zero.

Therefore, the quantification of the permanent-magnet's force capability and total force ripple, depends on the stator's winding design as well as the magnet array design. This analysis will be developed further in Section 4.3.3. However, there are other limitations on the stator design which limit the possible contribution of the winding pitch factor to the minimisation of force ripple.

3.2 Stator Layout

The stators are slotted to increase the force-density of the machine. Chapter 2 documents the consequences of this design choice. The primary concern is that there exist slot-cogging reluctance forces associated with the ferromagnetic teeth. This may be minimised through a more detailed tooth design.

The frequency at which the stator coils are excited is[26]:

$$f = \frac{\mathcal{V}_s}{2\tau_p} \quad (3.3)$$

In direct drive machines, the synchronous excitation velocity, \mathcal{V}_s , is limited by the frequency of the ocean waves and the stroke length of the machine. The higher the frequency of the induced voltage, the higher the voltage, and the lower the current requirement for the designed power output.

The frequency of the induced voltage may therefore be maximised through the minimisation of the machine's pole-pitch. Consequently, for a fixed tooth and slot width, the smallest pole-pitch is achieved with one slot per pole per phase. Thus the winding's pitch-factor becomes ineffective in limiting the effects of space-harmonics on the force-ripple. If a machine were to be designed using two slots per pole per phase, and short-chorded by one slot, the affects of the fifth harmonic may be minimised, but the pole-pitch would double in size. The necessity for a higher induced voltage frequency tends to overrule the minimisation of the harmonic forces using the windings. These harmonics are therefore best minimised through the appropriate selection of α_m , as previously mentioned.

The second deviation from traditional linear machine theory is in the quantification of the number of series-turns per phase. The number of series turns per phase for any electrical machine is $N_{ph} = p \times n_c \times N_c$. In all typical electrical machines, a coil constitutes a set of *send* and *return* conductors or turns. The number of series-conductors per coil is N_c , and the number of coils per pole per phase is n_c . In a double-layer configuration, $N_{sl} = 2N_c$ and $n_c = q$. In a single-layer configuration, $N_{sl} = N_c$ and $n_c = q/2$. N_{sl} is the number of series-turns per slot and q is the number of slots per pole per phase. Regardless of the layer configuration, the product of $N_c n_c$ is always equal to $qN_{sl}/2$. An alternative representation of the number of series-turns per phase is therefore $N_{ph} = pqN_{sl}/2$.

The double-sided tubular machine does not have a *return* conductor. The coils naturally return to where they originate from in each turn. The coils in this machine are wound in the transverse plane, as opposed to other machines which are wound along the axial plane of the machine. In this arrangement, the number of coils per pole per phase, n_c , is double that of a typical machine. The result of this is that the number of series turns per phase is double that of a typical machine. The resulting definition of the number of series-turn per

phase in a double-sided tubular machine is given by Equation 3.4.

$$N_{ph} = pm_c N_c = pq N_{sl} \quad (3.4)$$

The orientation of the winding means that the amount of flux which links with each coil is only half total flux per pole. This is because the flux enters the stator core and then splits into the positive and negative axial directions to link the coils. The nett result of this winding arrangement is that the number of series turns is doubled and the linked flux per series-turn is halved. The total flux linkage is therefore $N_{ph} k_w \hat{\Phi}/2$.

The use of an inner stator, surrounded by a cylindrical translator, raises concerns regarding its cooling. Traditional forced-air cooling is a likely solution to this problem, and is made possible by the reciprocating motion of the translator. By using the translator as an air-piston, air may be pushed past the inner stator, or through specially designed cooling ducts, to draw the heat away from the windings. Suitable air-valves may be used to ensure that the air is pushed in one direction only. Although beyond the scope of this research, suitable thermal modelling is required to ensure that the inner stator is not crippled by the thermal consequences of its position in the machine.

3.3 Conclusions

The introduction of an additional air-gap increases the force-capability of the machine without a proportional increase in the machine volume. This results in a greater utilisation of the machine's volume and the material from which it is constructed.

A surface-mounted permanent-magnet array is the most appropriate array for the application. The translator core has no discontinuities which improves the mechanical strength. This becomes a significant factor in wave energy generators which are often many metres long. This magnet array configuration also generates suitably low harmonics in the air-gap. The magnets' dimensions may be chosen so as to minimise the total force ripple. The stator design is slotted so as to increase the force density.

The overriding requirement for a higher frequency in the induced voltage of the generator means that it is unlikely that the winding configuration may be used to further minimise the affects of space-harmonics on the force distribution. The number of slots per pole per phase would typically be chosen as $q = 1$ so as to minimise the pole-pitch and increase the frequency of the induced voltage.

Chapter 4

Performance Calculations for the Double-Sided Tubular Machine

Introduction: The dual air-gaps of the double-sided tubular machine may be treated as two distinct electrical machines. However, the dimensions of one are coupled to the dimensions of the other. Applying design equations without cognisance of this coupling is fruitless. This chapter begins with a treatise in the modelling the magnetic materials of an electric machine. This is often excluded, resulting in invalid performance predictions. The behaviour of electrical machines in the context of ocean wave energy is discussed, focussing on the effects on the power ratings and operation of electrical machines in this environment. Thereafter, a detailed evaluation of the force capability of the layout is presented which makes use of the Magnetic Vector Potential of the stator windings. The magnetic circuit of the active component of flux is discussed. The value of this section is in the manner in which magnetic saturation and stator slot-leakage are accounted for. This, combined with the equation for the electromagnetic force, quantifies a machine's capabilities whilst including the effects of the parasitic losses in the magnetic circuit of the machine. Finally a design procedure is presented which describes what the author considers to be the two feasible objectives in a machine design. These are the optimisation of the electrical loading of the two stators and the optimisation of the machine's volume. The focus of the performance equations is the force capability. It does not deal with the optimisation of the dynamic losses, such as eddy-current losses.

In the mathematics to follow the subscripts of i and o representing the inner stator and outer stator variables are dropped for generality and neatness. All the equations are applicable to both the inner and outer stator systems. The distinction is only made in circumstances where the variables from both stators are present in the same set of equations.

4.1 Modelling of Magnetic Materials

4.1.1 Modelling of Permanent-Magnet Materials

Permanent-magnets are considered *hard magnetic materials*. These are materials with a wide hysteresis loop[30]. Unlike the electro-technical steel cores in the system, a permanent-magnet should operate only in the upper left-hand quadrant of its demagnetisation curve. This region is shown in Figure 4.1. A few important parameters may be defined for permanent-magnets[31]:

- Remnant Magnetic Flux Density B_r , or remnance, is the flux density which corresponds to $H = 0$. This may also be considered the point of magnetic “short-circuit”.
- Coercive Field Strength H_c , or coercivity, is the magnetic field intensity which corresponds to $B = 0$. This may also be considered the point of magnetic “open-circuit”.
- Saturation Magnetic Flux Density, B_{sat} , is the flux density at which all magnetic moments in the material are aligned with the externally applied magnetic field. As with other ferromagnetic materials, this occurs in the upper right-hand quadrant of the magnetisation curve and is greater than B_r .
- The Maximum Energy-Density Product, w_{max} , is the maximum energy density produced by the permanent-magnet. This is given by $w_{max} = (BH)_{max}/2$, where $(BH)_{max}$ corresponds to the co-ordinate (H_{max}, B_{max}) at which the product of B and H is at its maximum.
- The Form Factor of the Demagnetisation Curve, γ_m , is a measure of the characteristic shape of the demagnetisation curve, given by:

$$\gamma_m = \frac{B_{max}H_{max}}{B_rH_c} \quad (4.1)$$

The magnetic flux density B , and the magnetic field intensity H are parameters that may be measured in a magnetic circuit. These are the result of the normal demagnetisation curve, as shown in Figure 4.1 by the set of curves labelled as $B(H)$. The magnet itself has another magnetisation curve associated with it called the intrinsic magnetisation curve. This is shown in Figure 4.1 as the set of curves labelled as $B_i(H)$. Each intrinsic curve is associated with one of the normal curves. The intrinsic magnetisation curve cannot be measured as it is characteristic of the material without a magnetic circuit, yet the magnet will always exist in a magnetic circuit by its physical existence. The relationship between the normal and intrinsic curves is described by Equation 4.2[30][31].

$$B = \mu_0 H + B_i = \mu_0(H + M) = \mu_0[(1 + \chi)H + M_r] = \mu_0\mu_r H + B_r \quad (4.2)$$

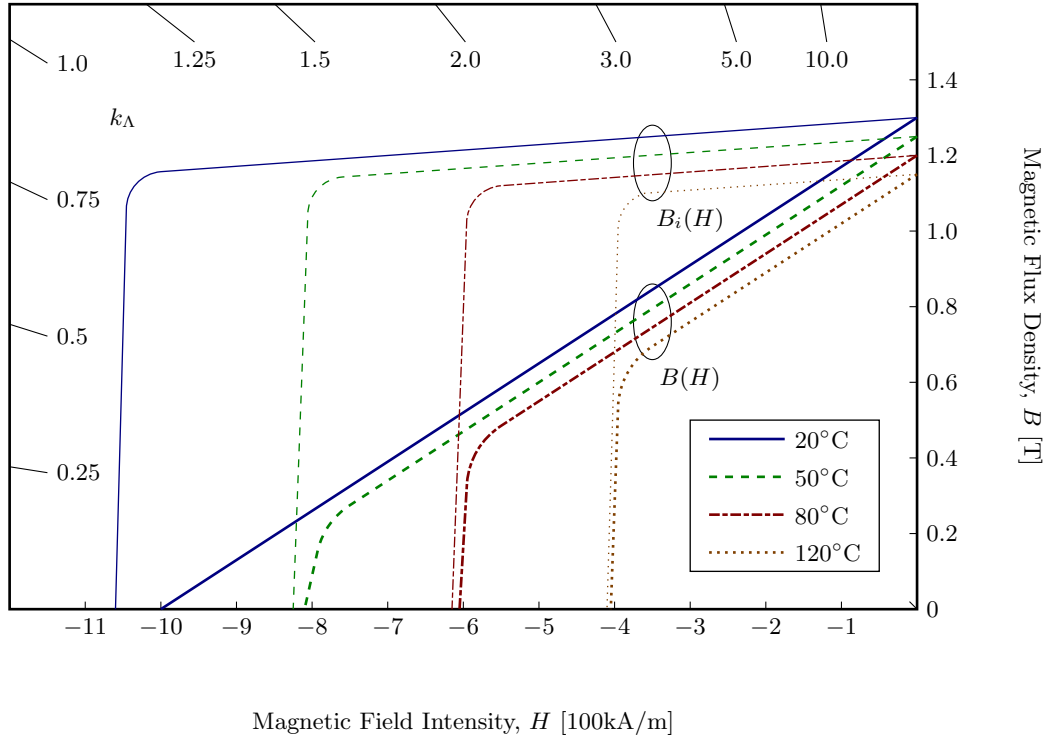


Figure 4.1: Exemplary Intrinsic and Normal Demagnetisation Curves at Various Temperatures. Intrinsic curves are labelled as $B_i(H)$ and normal curves are labelled as $B(H)$.

The component of magnetic flux $\mu_0 H$, is that component which appears in the magnet because of the non-ferromagnetic ingredients in the magnet, while the intrinsic magnetisation, $B_i = \mu_0 M = \mu_0 \chi H + M_r$, is that component which appears in the magnet because of the ferromagnetic ingredients in the magnet. The magnetisation, M , is proportional to the susceptibility of the material, χ . This parameter, χ , is a measure of how easily the materials is magnetised by an externally applied magnetic field intensity, H . In pure iron, this is very high, in the order of a few thousands, resulting in a high relative permeability, μ_r [32]. In a permanent-magnet, the material has a far smaller percentage ferromagnetic make-up and so the susceptibility is in the region of 1 to 3.5[26].

The intrinsic curve must be inferred based on the normal curve according to Equation 4.2. In magnetic circuits without external magnetic fields, it is not necessary to design with the intrinsic curve. However, with an externally applied field, which shifts the operating point dynamically, designing without this intrinsic curve may lead to permanent demagnetisation of the magnets.

Consider the curves in Figure 4.1. The load lines are shown along the left and top margins. Each load line has a slope of $-\mu_0 k_\Lambda$, and is labelled with the permeance coefficient of the magnetic circuit, k_Λ , represented by that load line. The intersection of these lines with the demagnetisation curves determines the point of operation of the permanent-magnets.

At 20°C operation at the point of maximum energy, $k_\Lambda = 1.0$, would seem acceptable. However, as temperature increases, the demagnetisation curves shift, and the operating point falls beyond the knee of the intrinsic demagnetisation curve at more than 50°C, even though the knee of the normal demagnetisation curve would only become a problem around 120°C. Thus the selection of a suitable load line is critical to the operation of the permanent-magnet above the knee of the *intrinsic* demagnetisation curve at all operating temperatures. To prevent the demagnetisation of the permanent-magnets, the permeance coefficient should be between 4 and 10. Ignoring the ferromagnetic cores in the magnetic circuit, and their saturation, the permeance coefficient may be represented by[31][33]:

$$k_\Lambda = \frac{A_g l_m}{A_m l_g} \quad (4.3)$$

The sensitivity of the demagnetisation curves to temperature may be accounted for by reducing the remnant flux, B_r , and the coercivity, H_c , according to Equations 4.4 and 4.5. The temperature coefficients α_B and α_H are expressed as negative values in %/°C.

$$B_r = B_{r20} \left[1 + \frac{\alpha_B}{100} (T_{op} - 20) \right] \quad (4.4)$$

$$H_c = H_{c20} \left[1 + \frac{\alpha_H}{100} (T_{op} - 20) \right] \quad (4.5)$$

The approximation of the demagnetisation curve takes the form of a hyperbola[30] as given in Equation 4.6. Variables B and H are the coordinates along the demagnetisation curve and a_0 is a factor given by Equation 4.7 which is a function of the form factor of the demagnetisation curve.

$$B = B_r \frac{H_c - H}{H_c - a_0 H} \quad (4.6)$$

$$a_0 = \frac{B_r}{B_{sat}} = \frac{2\sqrt{\gamma_m} - 1}{\gamma_m} \quad (4.7)$$

For rare-earth permanent-magnets, the demagnetisation curve is practically linear and so the form factor is given by $\gamma_m = 0.25$ at 20°C. This leaves $a_0 = 0$ and a relationship between B and H of:

$$B = B_r \left(1 - \frac{H}{H_c} \right) \quad (4.8)$$

When operating above 20°C, the value for a_0 may be approximated by Equation 4.9, where (B_k, H_k) are the coordinates of n arbitrarily chosen points $k = 1, 2, 3, \dots, n$ on the demagnetisation curve[30].

$$a_0 = \frac{1}{n} \sum_{k=1}^n \left(\frac{H_c}{H_k} + \frac{B_r}{B_k} - \frac{H_c}{H_k} \frac{B_r}{B_k} \right) \quad (4.9)$$

For the purposes of this research, only rare-earth permanent-magnets are considered because of their superior energy products and near-linear demagnetisation curves.

Equivalent Representations of Permanent-Magnets

Once the value for H_c has been determined, the permanent-magnets may be represented by their Thévenin or Norton equivalent two-terminal circuits, as shown in Figure 4.2[33]. In this manner, the magnet may be represented as either a flux source or an mmf source. The values of these flux and current sources correspond to the values of B_r and H_c on the demagnetisation curve respectively, such that $\mathcal{F}_c = H_c \times l_m$ and $\Phi_r = B_r \times A_m$. These values also represent the open- and short-circuit values of mmf and flux respectively in a two-terminal sense. The Thévenin equivalent model is used in the following discussions.

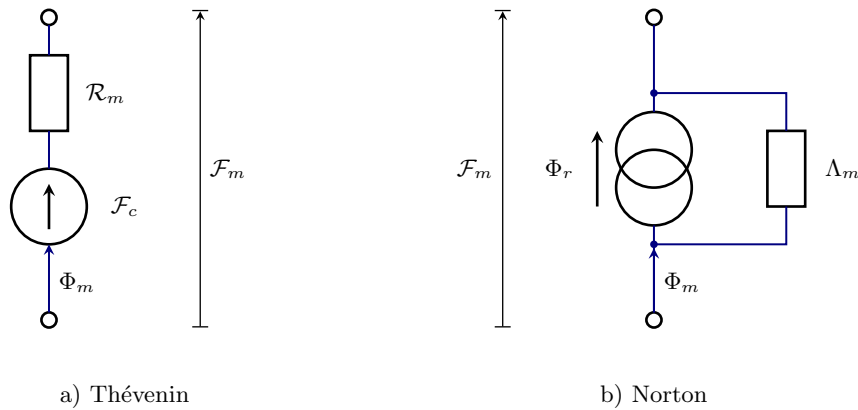


Figure 4.2: Thévenin and Norton Equivalent Circuit Models of Permanent-Magnets.

In the derivation of the electro-magnetic force, a third representation of the permanent-magnet is used, and is shown in Figure 4.3. In this representation, the mmf and magnetic flux are generated by the action of fictitious edge current densities which exist on the radial edges of the magnets[26].

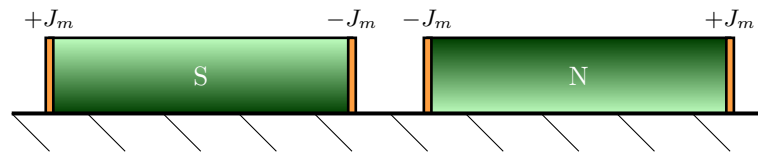


Figure 4.3: The Representation of Permanent-Magnets with the Aid of a Fictitious Edge Current Density, J_m . A positive value represents a current into the plane and a negative value represents a current out of the plane.

The value of J_m is numerically identical to the “open-circuit” coercivity, H_c :

$$J_m = \frac{B_r}{\mu_0 \mu_{rec}} \tag{4.10}$$

Quantifying the Space-Harmonics of the *mmf* Distribution

The *mmf* distribution of the permanent-magnet array is stepped by nature. The analysis presented in the following sections requires that the space harmonics be quantified as well as their respective magnetic fluxes per pole.

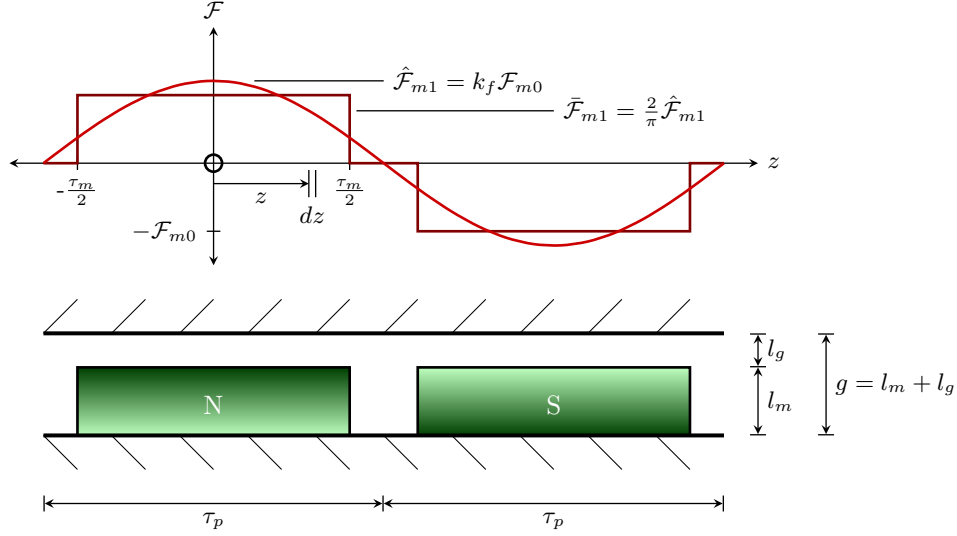


Figure 4.4: The *mmf* distribution may be defined by its harmonic components. The fundamental is shown as it is the component which acts in synchronism with the stator *mmf*. The flux per pole of the h^{th} harmonic, $\hat{\Phi}_h$, is the spatial sum of the flux developed at each point along the length of the pole by the *mmf* at that point.

The total *mmf* and flux are not the components which interact synchronously with the stator. In calculating the useful *mmf* and flux for the synchronous force capability, the fundamental component of this stepped distribution must be used. The value of the h^{th} Fourier coefficient of a step, as shown in Figure 4.4, is given by the following derivation[34]:

$$\begin{aligned}
 C_h &= \frac{1}{2\tau_p} \int_{-\tau_p}^{\tau_p} \mathcal{F}(z) e^{-jh\beta z} dz \\
 &= \frac{1}{2\tau_p} \left[2 \int_{-\frac{\tau_m}{2}}^{\frac{\tau_m}{2}} \mathcal{F}_{m0} e^{-jh\beta z} dz \right] \\
 &= \frac{\mathcal{F}_{m0}}{\tau_p} \left[\frac{e^{-jh\beta z}}{-jh\beta} \right]_{-\frac{\tau_m}{2}}^{\frac{\tau_m}{2}} \\
 &= \frac{\mathcal{F}_{m0}}{\tau_p} \frac{\tau_p}{-jh\pi} [e^{-jh\alpha_m \frac{\pi}{2}} - e^{jh\alpha_m \frac{\pi}{2}}] \\
 &= \frac{\mathcal{F}_{m0}}{-jh\pi} \left[-2j \sin \left(h \frac{\alpha_m \pi}{2} \right) \right] \\
 &= \frac{2\mathcal{F}_{m0}}{h\pi} \sin \left(h \frac{\alpha_m \pi}{2} \right) \quad \forall h \text{ odd}
 \end{aligned} \tag{4.11}$$

The original *mmf* distribution, as shown in Figure 4.4 does not comprise any even harmonics. This is because of the half-wave symmetry of the distribution. The value of C_h is

a real value. Therefore the phase angle, θ_h , of each harmonic may only be zero or π , depending on the value of the sinusoidal factor in Equation 4.11. The Fourier representation of the h^{th} harmonic in time and space is given in Equation 4.12. The magnitude of the h^{th} harmonic is given by twice the absolute value of the Fourier coefficient C_h [34], resulting in Equation 4.13. Thus the form factor of the *mmf* distribution for the h^{th} harmonic is given by k_{fh} in Equation 4.14. The form factor for the fundamental, which will be labelled k_f in further discussions, reduces to Equation 4.15.

$$\tilde{\mathcal{F}}_{mh}(z, t) = 2|C_h| \cos(h\beta z + \theta_h - \omega t) \quad (4.12)$$

$$\begin{aligned} \hat{\mathcal{F}}_{mh} &= 2|C_h| \\ &= \frac{4\mathcal{F}_{m0}}{h\pi} \left| \sin\left(h \frac{\alpha_m \pi}{2}\right) \right| \end{aligned} \quad (4.13)$$

$$\theta_h = \angle C_h$$

$$\therefore k_{fh} = \frac{\hat{\mathcal{F}}_{mh}}{\mathcal{F}_{m0}} = \frac{4}{h\pi} \left| \sin\left(h \frac{\alpha_m \pi}{2}\right) \right| \quad (4.14)$$

$$k_f = k_{f1} = \frac{4}{\pi} \sin\left(\frac{\alpha_m \pi}{2}\right) \quad (4.15)$$

Quantifying the Harmonic Flux Per-Pole

Having established the relationship between the magnet's *mmf*, \mathcal{F}_{m0} , and the harmonic component thereof, \mathcal{F}_{mh} , it is now important to establish how this affects the harmonic of the flux per pole in the air-gap. There is a distinct difference between the flux at any point in a pole-pitch and the flux per-pole. The flux per-pole is the space-integral of the flux at any point in a pole-pitch. Therefore $\hat{\Phi}$ does not represent the peak flux at any point within the magnetic circuit, but rather the peak flux crossing one pole-pitch.

The *mmf* required to develop $\hat{\Phi}$ is the spatial-average of the resultant *mmf* in the air-gap. This is shown mathematically in the following derivation which is based on Figure 4.4. There is an assumption of uniformity in the air-gap which suggests that the ferromagnetic material is infinitely permeable, and that the effects of slotting are excluded. This is an acceptable assumption for this stage of the model as we are simply deriving a generic expression for the relationship between the flux per pole and the *mmf*'s spatial distribution. The finite permeability of the cores will be taken into account in the modelling of their respective reluctances. The effects of slotting will be taken into account with the extension of the

air-gap according to Carter's coefficient.

$$\begin{aligned}
 d\tilde{\Phi}_h &= \frac{\tilde{\mathcal{F}}_h}{d\mathcal{R}} = \tilde{\mathcal{F}}_h \times \frac{\mu_0 L dz}{g} \\
 \therefore \tilde{\Phi}_h &= \int_{-\frac{\tau_p}{2}}^{\frac{\tau_p}{2}} \tilde{\mathcal{F}}_h \times \frac{\mu_0 L dz}{g} \\
 \tilde{\Phi}_h &= \frac{\hat{\mathcal{F}}_h \mu_0 L}{g} \int_{-\frac{\tau_p}{2}}^{\frac{\tau_p}{2}} \cos(h\beta z + \theta_h - \omega t) dz \\
 \tilde{\Phi}_h &= \frac{\hat{\mathcal{F}}_h \mu_0 L}{-gh\beta} \left[\sin\left(h\frac{\pi}{2} + \theta_h - \omega t\right) - \sin\left(-h\frac{\pi}{2} + \theta_h - \omega t\right) \right]
 \end{aligned}$$

Using : $\sin(A \pm B) = \sin A \cos B \pm \cos A \sin B$

and : $\cos(A \pm B) = \cos A \cos B \mp \sin A \sin B$

$$\begin{aligned}
 \tilde{\Phi}_h &= \frac{\hat{\mathcal{F}}_h \mu_0 L \tau_p}{gh\pi} \left[2 \sin\left(h\frac{\pi}{2}\right) \cos(\omega t - \theta_h) \right] \\
 \tilde{\Phi}_h &= \frac{\frac{2}{\pi} \hat{\mathcal{F}}_h}{h \frac{g}{\mu_0 L \tau_p}} \sin\left(h\frac{\pi}{2}\right) [\cos \omega t \cos \theta_h + \sin \omega t \sin \theta_h]
 \end{aligned}$$

But : $\sin \theta_h = 0 \forall h$ odd

$$\begin{aligned}
 \therefore \tilde{\Phi}_h &= \hat{\Phi}_h \sin\left(h\frac{\pi}{2}\right) \cos \theta_h \cos \omega t \\
 \therefore \hat{\Phi}_h &= \frac{\tilde{\mathcal{F}}_h}{h\mathcal{R}} \tag{4.16}
 \end{aligned}$$

From the derivation one can see that the flux per pole oscillates with time and has a peak value which is related to the *mmf* by a factor of $\frac{2}{\pi}$. This explains why the *mmfs* in the magnetic circuit of the active flux, to follow in Section 4.4, are prefixed with a factor of $\frac{2}{\pi}$.

4.1.2 Modelling Ferromagnetic Materials

The relationship between the magnetic field intensity (H) and the magnetic flux density (B) through a ferromagnetic material is non-linear. The exact relationship differs from material to material, however the characteristic remains the same.

Consider the “virgin” magnetisation curve shown in Figure 4.5. In the region before the knee, the permeability of the material is significantly higher than that of free space, μ_0 , by a relative permeability of up to $\mu_r = 9400$ [32]. In this region, the magnetic voltage drops (MVD) developed over the ferromagnetic regions are negligible in comparison to those developed across the air-gaps. This leads to the common assumption of infinite permeability in the ferromagnetic materials. It is important to note however that this knee occurs at a very low magnetic flux density of roughly 1.3 T. The design of a machine may involve the limitation of the flux density in the ferromagnetic material to below such a value, but this results in a larger machine than is necessary. If one designs such that flux densities of 1.5-1.8 T are achieved in the teeth of the machine[36], the material moves into the region of saturation, above the knee, where the assumption of infinite permeability no longer holds.

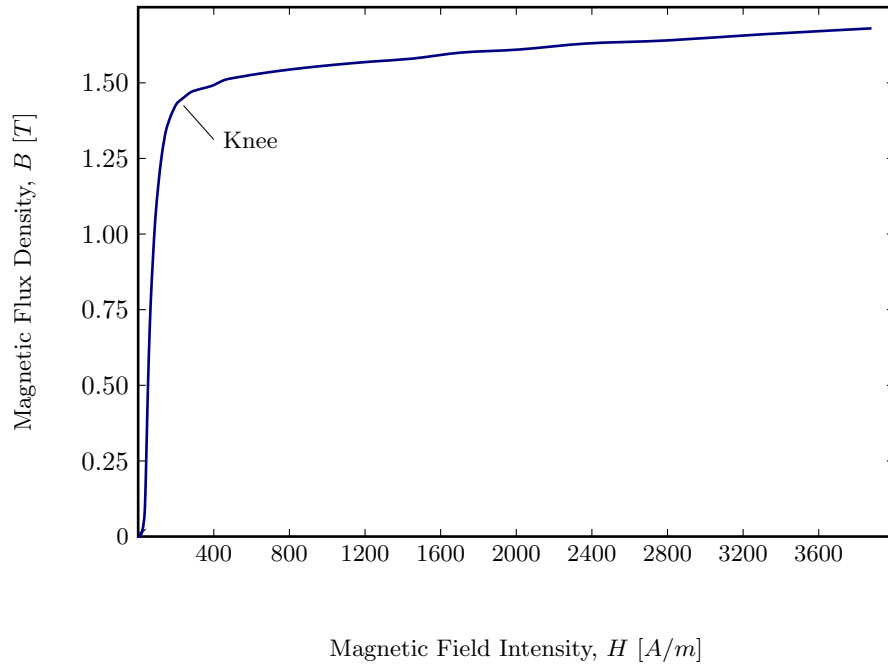


Figure 4.5: A Characteristic “Virgin” Magnetisation Curve of a Ferromagnetic Material. This is the curve before hysteresis cycling comes into effect and is used in the modelling of the machine. The data used to produce this curve is from the FEMM Library and is marked as “US Steel Type 2-S 0.018 Inch Thickness” [35]. This material was used consistently throughout the Finite-Element Analysis for this research.

The effect of saturation is that, for any given mmf , the effective flux in the air-gap is reduced because it is restricted by its passage through the ferromagnetic material. In analytical models that neglect the saturation, this results in a significantly higher force prediction than is possible.

To more accurately predict the force, the saturation must be taken into account. A simple, yet effective analytical expression for the relationship between B and H must be developed. Specifically, an expression for the value of μ_r as a function of B is required because the reluctances of the magnetic circuit are calculated according to $\mathcal{R} = l/\mu_r\mu_0A$. The flux density is readily calculated according to the linked magnetic flux, and so a function of B is the most appropriate representation of μ_r .

A multi-termed, exponential expression may be used to represent μ_r as a function of B . Although fairly accurate, the integration of the exponential as part of the reluctances does not have an analytic form because of the integral of the exponential $e^{\frac{1}{r}}$. A simpler expression is required.

The characteristic equation of the simplest and yet most effective solution is shown in Equation 4.17. It requires the definition of four constants, $k_{\mu 1}, n_{\mu 1}, k_{\mu 2}, n_{\mu 2}$. The resulting curve for “US Steel Type 2-S 0.018 Inch Thickness” is given in Figure 4.6. The author

believes that the error presented represents the most appropriate trade-off between absolute accuracy and simplicity.

$$\mu_r(B) = \frac{1}{k_{\mu 1} B^{n_{\mu 1}} + k_{\mu 2} B^{n_{\mu 2}}} \quad (4.17)$$

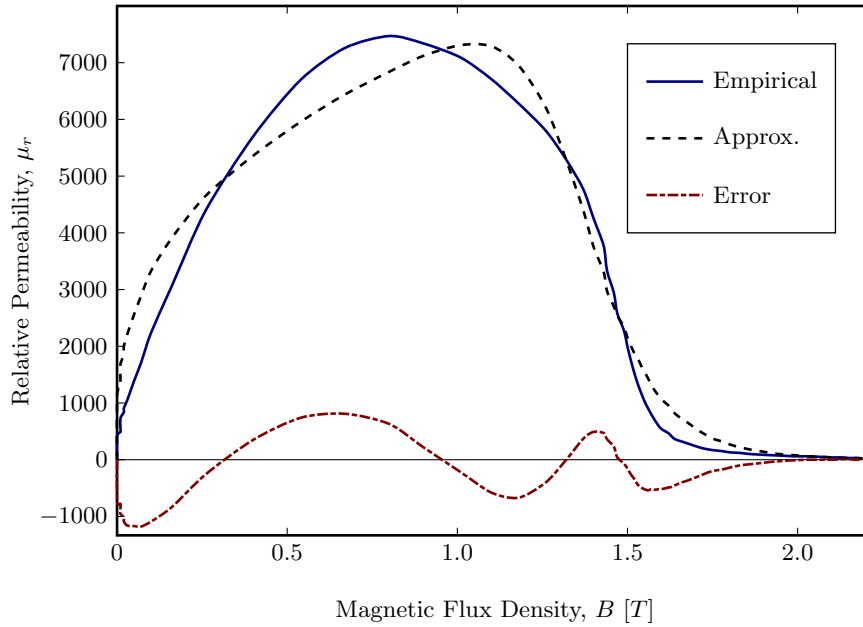


Figure 4.6: Approximation of the Relative Permeability of “US Steel Type 2-S 0.018 Inch Thickness”. The set of constants are $k_{\mu 1} = 1.35 \times 10^{-4}$, $n_{\mu 1} = -0.35$, $k_{\mu 2} = 2.0 \times 10^{-6}$ and $n_{\mu 2} = 12.75$.

4.2 Power in Oscillating Wave-Energy Systems

4.2.1 The Mechanical Power of the Swells

The force produced by the action of the waves on an absorber oscillates with the angular frequency of the swells, ω_m . The acceleration that results is resisted by the hydrodynamic drag and/or inertia of the absorber. Thus the velocity of the absorber will lag behind the application of force. Consider the force phasor, $\tilde{F} = \hat{F} \cos(\omega_m t)$ and the associated velocity phasor, $\tilde{V} = \hat{V} \cos(\omega_m t - \theta_m)$. This system may be represented as in Figure 4.7.

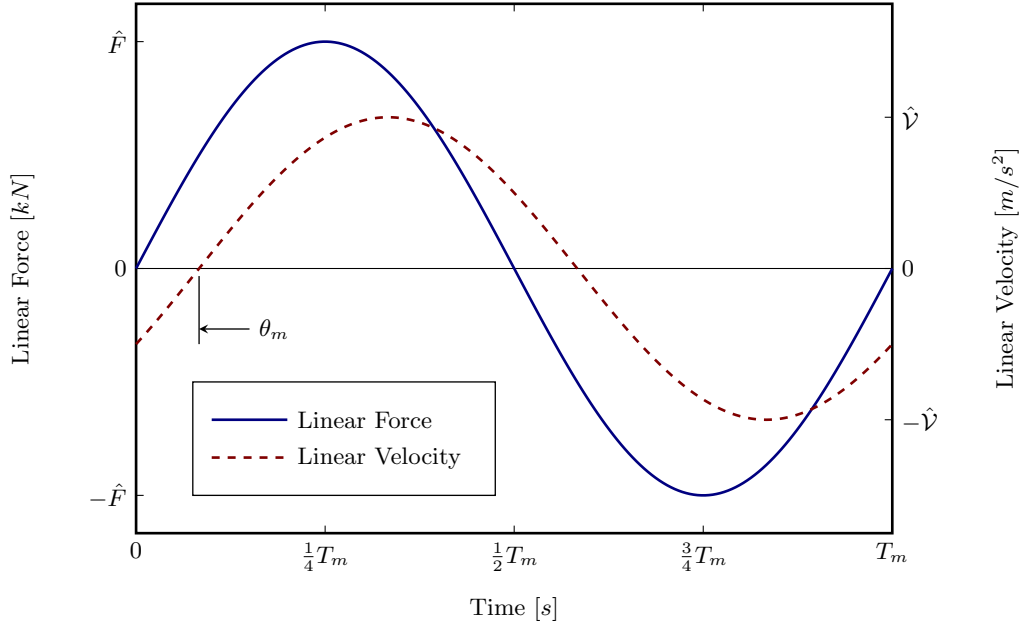


Figure 4.7: Linear Force and Induced Linear Velocity of Oscillating Wave Energy Converters.

This system is analogous to an electrical alternating-current system. The instantaneous power of such a system is given by the product of \tilde{F} and \tilde{V} . The resultant apparent power function is comprised of two components which oscillate in quadrature:

$$\begin{aligned}
 \tilde{S}_m &= \hat{F} \cos(\omega_m t) \times \hat{V} \cos(\omega_m t - \theta_m) \\
 &= \frac{\hat{F}\hat{V}}{2} \{ \cos \theta_m + \cos(2\omega_m t - \theta_m) \} \\
 &= \frac{\hat{F}\hat{V}}{2} \{ \cos \theta_m + \cos \theta_m \cos(2\omega_m t) + \sin \theta_m \sin(2\omega_m t) \} \\
 &= \frac{\hat{F}\hat{V}}{2} \cos \theta_m \times \{ 1 + \cos(2\omega_m t) \} + \frac{\hat{F}\hat{V}}{2} \sin \theta_m \times \sin(2\omega_m t) \quad (4.18)
 \end{aligned}$$

$$\text{Using : } \cos u \cos v = \frac{1}{2} \{ \cos(u - v) + \cos(u + v) \}$$

$$\cos(u - v) = \cos u \cos v + \sin u \sin v$$

The first term is the active power, while the second term is the reactive power. The average of \tilde{S}_m is the coefficient of the active power component. This is because both the sine and the cosine components average out to zero over a full period. Therefore, for this sinusoidally excited mechanical system, the average power is given by Equation 4.19. It is important to note that the RMS values, F and \mathcal{V} , are given by the quotient of their respective peaks divided by $\sqrt{2}$, as is typical of a sinusoidally excited system.

$$\bar{P}_m = \frac{\hat{F}\hat{\mathcal{V}}}{2} \cos \theta_m = F\mathcal{V} \cos \theta_m \quad (4.19)$$

4.2.2 The Electrical Power Delivered by the Generator

The oscillating frequency of the electrical system in a linear-generator-based wave-energy converter is modulated by the velocity phasor of the mechanical system[26]:

$$\begin{aligned} \tilde{\omega}_e &= 2\pi \times \frac{\tilde{\mathcal{V}}}{2\tau_p} = \frac{\pi\hat{\mathcal{V}}}{\tau_p} \cos(\omega_m t - \theta_m) \\ \tilde{\omega}_e &= \hat{\omega}_e \cos(\omega_m t - \theta_m) \end{aligned} \quad (4.20)$$

The implication of this modulation is that the flux linkage $\tilde{\lambda}$ has a sinusoidally varying frequency. The derivative of this flux linkage is the induced *emf* $\tilde{\mathcal{E}}$. This *emf* may be visualised as a function with a frequency modulated by ω_m and an amplitude modulated by $\tilde{\omega}_e$ as shown in Figure 4.8. The induced *emf* has a motional component, $\tilde{\mathcal{E}}_m$, and a pulsational component, $\tilde{\mathcal{E}}_p$ [36][37]:

$$\tilde{\mathcal{E}} = \frac{d\tilde{\lambda}}{dt} = \frac{\partial\tilde{\lambda}}{\partial\tilde{\phi}_e} \cdot \frac{d\tilde{\phi}_e}{dt} + \frac{\partial\tilde{\lambda}}{\partial t} = \tilde{\mathcal{E}}_m + \tilde{\mathcal{E}}_p \quad (4.21)$$

The partial derivative of the flux linkage with respect to time is only non-zero if the excitation field is time-varying independent of the translator position. Given that the excitation field in a permanent-magnet machine is not time-varying, $\tilde{\mathcal{E}}_p = 0$. Thus the only component of the *emf* that remains is the motional component $\tilde{\mathcal{E}}_m$ according to Equation 4.22.

$$\begin{aligned} \tilde{\lambda} &= N_{ph}k_w\hat{\Phi} \cos(\tilde{\omega}_e t - \theta_e) \\ \tilde{\mathcal{E}} &= \frac{\partial\tilde{\lambda}}{\partial\tilde{\phi}_e} \cdot \frac{d\tilde{\phi}_e}{dt} = \frac{\partial\tilde{\lambda}}{\partial\tilde{\phi}_e} \cdot \tilde{\omega}_e \\ \tilde{\mathcal{E}} &= -N_{ph}k_w\hat{\Phi}\tilde{\omega}_e \sin(\tilde{\omega}_e t - \theta_e) \\ \tilde{\mathcal{E}} &= -N_{ph}k_w\hat{\Phi}\hat{\omega}_e \cos(\omega_m t - \theta_m) \sin(\tilde{\omega}_e t - \theta_e) \end{aligned} \quad (4.22)$$

Unlike the mechanical system, the RMS value of Equation 4.22 cannot be derived analytically from Equation 4.22 because $\tilde{\mathcal{E}}^2$ has no analytical integral. By considering the total instantaneous power as the combination of the powers in each phase, Brooking and Mueller show that the RMS value is comprised of a factor of $\sqrt{2}$ because the signal is oscillating, and a second factor of $\sqrt{2}$ because of the sinusoidal amplitude-modulation caused by $\tilde{\omega}_e$ [38].

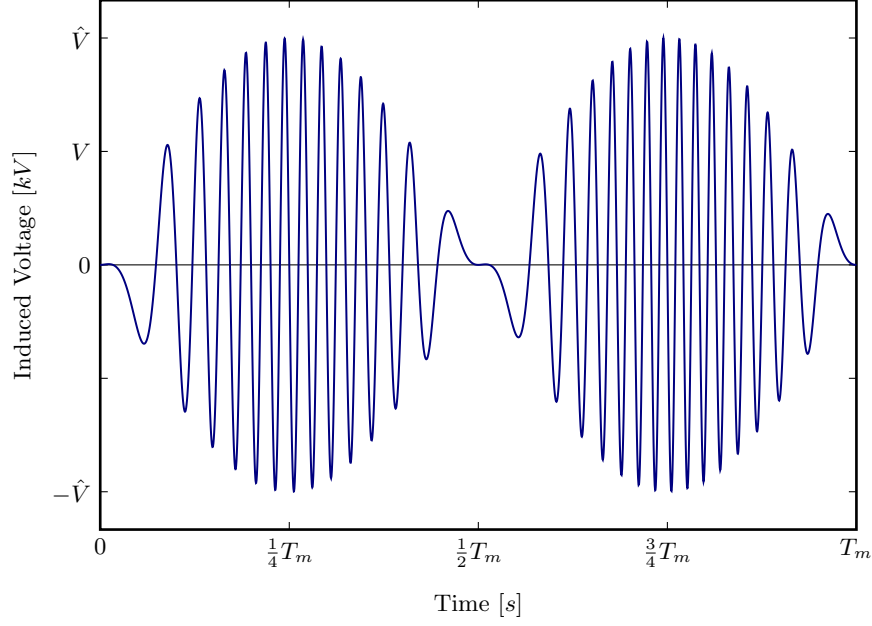


Figure 4.8: Voltage of a Linear Synchronous Generator Induced by the Motion of the Permanent-Magnets past the Stator Windings. Of particular importance is the modulation of the amplitude and frequency. This is caused by the sinusoidally varying application of force and the resulting sinusoidally varying velocity.

The RMS voltage is therefore half of the peak voltage, as shown in Figure 4.8. Assuming that the current \tilde{I} is proportional to $\tilde{\mathcal{E}}$, and ignoring the stator's self-impedance, we may now represent the electrical power output as:

$$\begin{aligned}
 V = \mathcal{E} &= \frac{\hat{\mathcal{E}}}{\sqrt{2} \times \sqrt{2}} = \frac{\hat{\mathcal{E}}}{2} = \frac{\hat{V}}{2} \\
 I &= \frac{\hat{I}}{\sqrt{2} \times \sqrt{2}} = \frac{\hat{I}}{2} \\
 \bar{P}_e &= \frac{\hat{V}}{2} \frac{\hat{I}}{2} \cos \theta_e = \frac{\hat{V} \hat{I}}{4} \cos \theta_e
 \end{aligned} \tag{4.23}$$

4.2.3 Phasor Representation of the Double-Sided Tubular Machine

When a synchronous generator is connected to an infinite bus, the resultant *mmf* in the air-gap is defined by the need for the induced *emf* to balance the bus voltage. As such, there is scope for over- and under-excitation, depending on the operating conditions of the machine relative to the infinite bus[36].

In the case of a direct-drive linear synchronous generator for wave energy conversion, the terminal voltage and frequency are set by the device itself, recovered through power electronics and then synchronised to the grid by the power electronics. Therefore, the resultant *mmf* in the air-gap is not determined by the device's bus system. Power electronics will typically track the maximum power set-point of the device in order to draw the most

power from the system. Therefore, the stator does not need to act in such a fashion as to aid or retard the air-gap *mmf* so as to match a “system”-derived *mmf* .

We can therefore consider that the case for over-excitation is not applicable in these types of machines as this would reduce the air-gap *mmf* and hence the force capability. The resultant air-gap *mmf* is the resultant of the translator and stator *mmfs* . The relevant phasor diagram for this generator, operating as an under-excited synchronous machine, is shown in Figure 4.9.

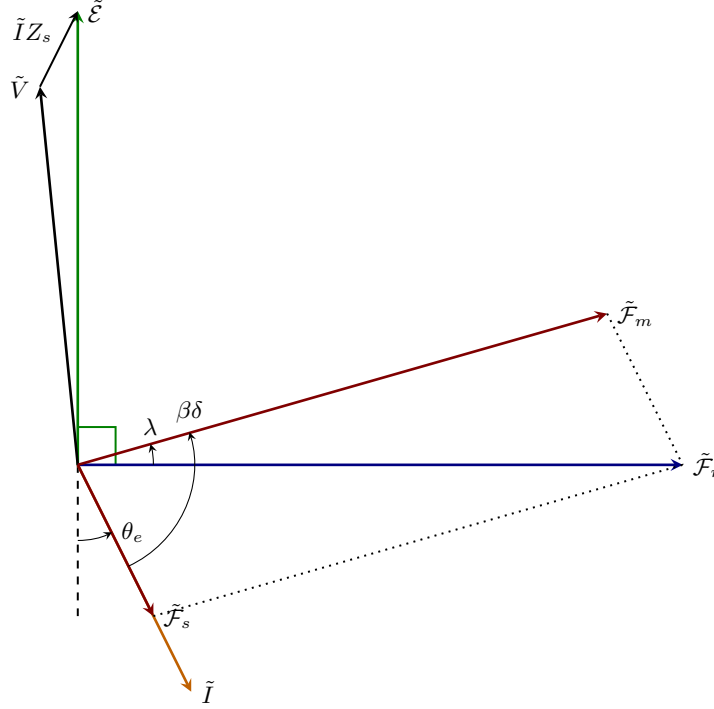


Figure 4.9: Phasor Diagram for an Under-excited Permanent-Magnet Synchronous Generator. The stator’s self impedance has been represented as Z_s which comprises the stators’ resistance, R_s and self-inductance X_s .

The average electrical and average mechanical power, as derived in Section 4.2.2 and 4.2.1 respectively, are linked by a factor of η , the efficiency. In an m -phase machine, the total electrical power is m times the power in each phase, such that, for a generator:

$$\bar{P}_m = \frac{\bar{P}_e}{\eta} = m \frac{\bar{P}_{ph}}{\eta} \quad (4.24)$$

$$\frac{\hat{F}\hat{V}}{2} \cos \theta_m = m \frac{\hat{V}_{ph}\hat{I}_{ph}}{4} \frac{\cos \theta_e}{\eta} \quad (4.25)$$

$$\hat{F} = m \frac{\hat{V}_{ph}\hat{I}_{ph}}{2\hat{V}} \times \frac{\cos \theta_e}{\eta \cos \theta_m} \quad (4.26)$$

The mechanical alignment of the magnets is such that their respective magnetic fields are spatially in phase. The *emfs* induced in each of the respective stators are therefore in phase. It is recommended that the stator sections are connected in series such that, with

the exclusion of the stators' self-inductance and series resistance ($Z_s = R_s + jX_s$):

$$\tilde{V}_{ph} = \tilde{\mathcal{E}}_{ph} = \tilde{\mathcal{E}}_{pho} + \tilde{\mathcal{E}}_{phi} \quad (4.27)$$

$$\tilde{I}_{ph} = \tilde{I}_{pho} = \tilde{I}_{phi} \quad (4.28)$$

From the discussion in Section 3.2, the flux linkage may be represented as $\frac{N_{ph}k_w\hat{\Phi}}{2}$. Substituting this into Equation 4.22 allows the induced *emf* to be expressed as per Equation 4.29.

$$\tilde{\mathcal{E}}_{ph} = -N_{ph}k_w \frac{\hat{\Phi}}{2} \tilde{\omega}_e \sin(\tilde{\omega}_e t - \theta_e) \quad (4.29)$$

$$\tilde{\mathcal{E}}_{ph} = -\frac{\tilde{\omega}_e}{2} \left(N_{pho}k_{wo}\hat{\Phi}_o + N_{phi}k_{wi}\hat{\Phi}_i \right) \sin(\tilde{\omega}_e t - \theta_e)$$

$$\hat{V}_{ph} = \hat{\mathcal{E}}_{ph} = \frac{\hat{V}\pi}{2\tau_p} \left(N_{pho}k_{wo}\hat{\Phi}_o + N_{phi}k_{wi}\hat{\Phi}_i \right) \quad (4.30)$$

Substituting Equation 4.30 into Equation 4.26 results in Equation 4.31:

$$\hat{F} = \frac{m}{2\hat{Y}} \frac{\hat{V}\pi}{2\tau_p} \left(N_{pho}k_{wo}\hat{I}_{pho}\hat{\Phi}_o + N_{phi}k_{wi}\hat{I}_{phi}\hat{\Phi}_i \right) \times \frac{\cos\theta_e}{\eta \cos\theta_m}$$

$$\hat{F} = \frac{m\pi}{4\tau_p} \left(N_{pho}k_{wo}\hat{I}_{pho}\hat{\Phi}_o + N_{phi}k_{wi}\hat{I}_{phi}\hat{\Phi}_i \right) \times \frac{\cos\theta_e}{\eta \cos\theta_m} \quad (4.31)$$

The Specific Electric Loading, Q , is defined as the RMS Ampere-conductors per unit air-gap length[26]:

$$Q = \frac{mN_{ph}k_w I_{ph}}{L} \quad (4.32)$$

$$\therefore N_{ph}k_w \hat{I}_{ph} = \frac{2QL}{m} \quad (4.33)$$

$$\therefore \hat{I}_{ph} = 2I_{ph}$$

By substituting Equation 4.33 into Equation 4.31, we may determine the final electro-mechanical equation for the dynamic force-capability of the machine, derived from the phasor diagram:

$$\hat{F} = \frac{m\pi}{4\tau_p} \left(\frac{2Q_o L}{m} \hat{\Phi}_o + \frac{2Q_i L}{m} \hat{\Phi}_i \right) \times \frac{\cos\theta_e}{\eta \cos\theta_m}$$

$$= \frac{\pi L}{2\tau_p} \left(Q_o \hat{\Phi}_o + Q_i \hat{\Phi}_i \right) \times \frac{\cos\theta_e}{\eta \cos\theta_m} \quad (4.34)$$

The primary value of Equation 4.34 is in its representation of the relationship between the dynamic force-capability of the machine in the environment, and the static force capability of the machine. When actuated by a mechanically oscillating system, such as the ocean waves, the power factors and efficiency will reduce the effective force that may be absorbed. The first factor of Equation 4.34 is the static force-capability of the machine; the second factor accounts for the effects of the dynamic system. Rearranging this equation, we may show the relationship between the static and dynamic force components as:

$$\hat{F} = \hat{F}_{static} \times \frac{\cos\theta_e}{\eta \cos\theta_m}$$

$$\text{where : } \hat{F}_{static} = \frac{\pi L}{2\tau_p} \left(Q_o \hat{\Phi}_o + Q_i \hat{\Phi}_i \right) \quad (4.35)$$

This representation of the force capability of the machine is relevant in that it illustrates the dynamic response of the machine. However, the quantification of \hat{F}_{static} depends on an accurate quantification of the active magnetic flux in the machine. Magnetic circuit modelling is not flexible enough to cater for all the possible flux paths that may occur in any given design. Taking into account the effects of magnetic leakage flux by this method is inaccurate and unreliable. Therefore, this representation will not be used for the determination of the static force capability. The Magnetic Vector Potential method will be used instead, and follows in Section 4.3.

4.2.4 Electrical Power Factor

The resultant *mmf* in the air-gap is the vector-sum of the *mmf* from the magnets and the *mmf* from the stator windings. This is reflected in Figure 4.9. The resultant *mmf* in either air-gap is therefore given by:

$$\begin{aligned}\tilde{\mathcal{F}}_r &= \tilde{\mathcal{F}}_m + \tilde{\mathcal{F}}_s \\ \therefore \hat{\mathcal{F}}_r^2 &= \hat{\mathcal{F}}_m^2 + \hat{\mathcal{F}}_s^2 - 2\hat{\mathcal{F}}_m\hat{\mathcal{F}}_s \cos \beta\delta\end{aligned}\quad (4.36)$$

The force capability is maximised when the stator and translator *mmfs* are in quadrature, i.e.: $\beta\delta = \pi/2 \therefore \delta = \tau_p/2$. This is most easily understood by considering that the force is developed by the action of the component of stator flux which is in quadrature with the translator flux. If $\delta = \tau_p/2$ then the stator flux is completely in quadrature with the field flux, and $\hat{\mathcal{F}}_r$ becomes:

$$\hat{\mathcal{F}}_r = \sqrt{\hat{\mathcal{F}}_m^2 + \hat{\mathcal{F}}_s^2}\quad (4.37)$$

The relative magnitudes of the stator and rotor *mmfs* affect the power factor of the electrical system. From the phasor diagram, it is evident that the electrical power factor is given by $\cos \theta_e$, neglecting the stator's own impedance, Z_s . We may form the following equations from the diagram:

$$\begin{aligned}\hat{\mathcal{F}}_m \sin \lambda &= \hat{\mathcal{F}}_s \cos \theta_e \\ \therefore \cos \theta_e &= \frac{\hat{\mathcal{F}}_m}{\hat{\mathcal{F}}_s} \sin \lambda \\ \text{But : } \therefore \frac{\sin (180 - \beta\delta)}{\hat{\mathcal{F}}_r} &= \frac{\sin \lambda}{\hat{\mathcal{F}}_s} \\ \cos \theta_e &= \frac{\hat{\mathcal{F}}_m}{\hat{\mathcal{F}}_s} \times \frac{\hat{\mathcal{F}}_s}{\hat{\mathcal{F}}_r} \sin \beta\delta \\ \therefore \cos \theta_e &= \frac{\hat{\mathcal{F}}_m}{\hat{\mathcal{F}}_r} \sin \beta\delta\end{aligned}\quad (4.38)$$

It has already been determined that power electronics can be used to match the peak power delivery by drawing current such that $\beta\delta = \pi/2$. The contribution of the magnets'

mmf and the resultant mmf may therefore be related to the system power factor, $\cos \theta_e$, by Equation 4.39 where $\beta\delta = \pi/2$, leaving $\sin \beta\delta = 1$.

$$\hat{\mathcal{F}}_m = \hat{\mathcal{F}}_r \times \cos \theta_e \quad (4.39)$$

The power factor for a permanent-magnet synchronous machine is typically greater than 0.9. This means that the resultant mmf is almost identical to the translator mmf .

4.2.5 Magneto-Motive Forces

Magneto-motive Force of the Permanent-Magnets

We represent the magnets by an equivalent coil distributed along the edges of the magnet and carrying a fictitious surface current that would produce an equivalent flux and field intensity as in Section 4.1.1. This edge-current density, J_m , is then used to find $\hat{\mathcal{F}}_{mh}$ as given in Equation 4.40.

$$\hat{\mathcal{F}}_{mh} = J_m \times l_m \times k_{fh} \quad (4.40)$$

Magneto-motive Force of the Stator Coils

Unlike a flat linear machine, where the coils are wound in the axial plane, the mmf distribution of single coil-pitch, τ_c , is generated by the action of two coils, not one. The mmf distribution of two tubular coils, spaced one coil-pitch apart, may be decomposed into a Fourier series of space-harmonics[39]. For N_c turns per coils, each carrying a current of \tilde{I}_c and having a pole-pitch of τ_p , the distribution may be expressed as:

$$\tilde{\mathcal{F}}_c(z) = \sum_{h=1}^{\infty} \frac{2N_c \tilde{I}_c}{h\pi} \sin(h\alpha_c\pi/2) \cos(h\beta z)$$

given : $\beta = \frac{\pi}{\tau_p}$ and $\alpha_c = \frac{\tau_c}{\tau_p}$

When grouped together to form a phase, the distribution of the coils must be considered. The resulting mmf of a single phase of n_c coils is:

$$\begin{aligned} \tilde{\mathcal{F}}_{ph}(z) &= \sum_{h=1}^{\infty} \frac{2N_c n_c \tilde{I}_c}{h\pi} \sin(h\alpha_c\pi/2) \frac{\sin\left(h\frac{\pi}{2m}\right)}{q \sin\left(h\frac{\pi}{2mq}\right)} \cos(h\beta z) \quad \forall h \text{ odd} \\ \tilde{\mathcal{F}}_{ph}(z) &= \sum_{h=1}^{\infty} \frac{2N_c n_c \tilde{I}_c}{h\pi} k_{wh} \cos(h\beta z) \end{aligned} \quad (4.41)$$

where : $k_{wh} = k_{ph} k_{dh}$ is the winding factor

given : $k_{ph} = \sin(h\alpha_c\pi/2)$ as the pitch factor, and

$$k_{dh} = \frac{\sin\left(h\frac{\pi}{2m}\right)}{q \sin\left(h\frac{\pi}{2mq}\right)} \text{ as the distribution factor}$$

The resulting *mmf* of a single phase is comprised of only odd harmonics. This is because the even harmonics are eliminated either through the use of double-layer windings, or through the half-wave symmetry of single-layer windings. The coil pitch of a double layer winding may be chosen so as to eliminate further space harmonics.

Equation 3.4 gives the number of series-turns per phase, regardless of the layer configuration, as $N_{ph} = pn_c N_c$. The *mmf* of a single phase may therefore be written in terms of the number of series-turns per phase and the phase current:

$$\tilde{\mathcal{F}}_{ph}(z) = \sum_{h=1}^{\infty} \frac{2N_{ph}\tilde{I}_{ph}k_{wh}}{h\pi p} \cos(h\beta z) \quad (4.42)$$

When excited by a sinusoidal current, $\tilde{I}_{ph} = \hat{I}_{ph} \cos \tilde{\omega}_e t$, the *mmf* may be represented as two counter-rotating *mmf* waves of half the peak amplitude of their combined *mmf*:

$$\tilde{\mathcal{F}}_{ph}(z, t) = \frac{1}{2} \sum_{h=1}^{\infty} \frac{2N_{ph}\hat{I}_{ph}k_{wh}}{h\pi p} \{\cos(h\beta z - \tilde{\omega}_e t) + \cos(h\beta z + \tilde{\omega}_e t)\} \quad (4.43)$$

The *mmf* of each subsequent phase of an m -phase machine is shifted by $2\pi/m$ electrical radians in space from the magnetic axis of the first phase, as well as by $2\pi/m$ electrical radians in time. The the generic expression for the h^{th} harmonic *mmf* of the m'^{th} phase is given by Equation 4.44.

$$\begin{aligned} \tilde{\mathcal{F}}_{hph}(m', z, t) &= \frac{1}{2} \sum_{h=1}^{\infty} \hat{\mathcal{F}}_{hph} \left\{ \cos \left(h \left(\beta z - (m' - 1) \frac{2\pi}{m} \right) - \left(\tilde{\omega}_e t - (m' - 1) \frac{2\pi}{m} \right) \right) \right. \\ &\quad \left. + \cos \left(h \left(\beta z - (m' - 1) \frac{2\pi}{m} \right) + \left(\tilde{\omega}_e t - (m' - 1) \frac{2\pi}{m} \right) \right) \right\} \\ &= \frac{1}{2} \sum_{h=1}^{\infty} \hat{\mathcal{F}}_{hph} \left\{ \cos \left((h\beta z - \tilde{\omega}_e t) - (h - 1)(m' - 1) \frac{2\pi}{m} \right) \right. \\ &\quad \left. + \cos \left((h\beta z + \tilde{\omega}_e t) - (h + 1)(m' - 1) \frac{2\pi}{m} \right) \right\} \end{aligned} \quad (4.44)$$

$$\text{where : } \hat{\mathcal{F}}_{hph} = \frac{2N_{ph}\hat{I}_{hph}k_{wh}}{h\pi p}$$

The resultant *mmf* of all m -phases is the sum of the individual phase *mmfs*. For each harmonic, the resultant *mmf* may either have a positive phase sequence (forward travelling waves augment while reverse travelling waves cancel), a negative phase sequence (reverse travelling waves augment while forward travelling waves cancel), or zero phase sequence (all waves cancel).

Consider the instant in time and position in space when $h\beta z - \tilde{\omega}_e t = 0$. For the positive phase sequence harmonics orders, $h = 2mk + 1, k = 0, 1, 2, \dots$, the forward travelling wave in

Equation 4.44 becomes:

$$\begin{aligned}
\cos\left((h\beta z - \tilde{\omega}_e t) - (h-1)(m'-1)\frac{2\pi}{m}\right) &= \cos\left((h-1)(m'-1)\frac{2\pi}{m}\right) \\
&= \cos\left((2mk+1-1)(m'-1)\frac{2\pi}{m}\right) \\
&= \cos((2k)(m'-1)2\pi) \\
&= \cos(2n\pi) = 1 \quad \because k, n, (m'-1) \in \mathbb{N} \quad (4.45)
\end{aligned}$$

The sum of the forward travelling harmonic waves of all phases is therefore m times the sum of the forward travelling harmonic waves of one phase, $1 \times m = m$. For the reverse travelling waves, the phases of the harmonic mmf s are uniformly distributed about 2π electrical radians. Therefore their sum is zero, and the resultant mmf of all reverse travelling harmonic waves of all phases is zero:

$$\cos\left((h\beta z + \tilde{\omega}_e t) - (h+1)(m'-1)\frac{2\pi}{m}\right) = \cos\left((h+1)(m'-1)\frac{2\pi}{m}\right) \quad (4.46)$$

For the negative phase sequence harmonic orders, $h = 2mk - 1, k = 1, 2, 3, \dots$, the opposite is true. All forward travelling harmonic waves sum to zero, while all reverse travelling harmonic waves of all the phases sum to a resultant mmf of m times the individual phase mmf .

The resultant positive and negative phase sequence mmf s are thus given by Equation 4.47 and 4.48 respectively.

$$\tilde{\mathcal{F}}_h^+(z, t) = \frac{m}{2} \sum_{\substack{h=2mk+1 \\ k=0,1,2,\dots}}^{\infty} \hat{\mathcal{F}}_{hph} \cos(h\beta z - \tilde{\omega}_e t) \quad (4.47)$$

$$\tilde{\mathcal{F}}_h^-(z, t) = \frac{m}{2} \sum_{\substack{h=2mk-1 \\ k=1,2,3,\dots}}^{\infty} \hat{\mathcal{F}}_{hph} \cos(h\beta z + \tilde{\omega}_e t) \quad (4.48)$$

Equation 4.33 may now be used to express the mmf s in terms of the Specific Electrical Loading, Q_h :

$$\tilde{\mathcal{F}}_h^+(z, t) = \frac{1}{2} \sum_{\substack{h=2mk+1 \\ k=0,1,2,\dots}}^{\infty} \frac{4Q_h\tau_p}{h\pi} \cos(\tilde{\omega}_e t - h\beta z) \quad (4.49)$$

$$\tilde{\mathcal{F}}_h^-(z, t) = \frac{1}{2} \sum_{\substack{h=2mk-1 \\ k=1,2,3,\dots}}^{\infty} \frac{4Q_h\tau_p}{h\pi} \cos(\tilde{\omega}_e t + h\beta z) \quad (4.50)$$

$$\text{given : } N_{ph} \hat{I}_{ph} k_{wh} = \frac{2Q_h L}{m} \text{ and } L = p\tau_p$$

4.3 Electromagnetic Force using the Magnetic Vector Potential Method

The Magnetic Vector Potential (MVP) method is a very accurate method of direct force calculation. The force is calculated using the Lorentz equation for the force acting on a current-carrying coil in the presence of a magnetic field[40]:

$$\vec{F} = \tilde{I} \int d\vec{l} \times \vec{B} \quad (4.51)$$

The magnetic flux density, \vec{B} , in Equation 4.51 does not include the reaction magnetic flux density from the current \tilde{I} in the conductor on which the force acts. For the present machine analysis, the magnetic flux, \vec{B} , is developed by the armature windings, while the conductor on which this field acts is the fictitious edge-current density defining a permanent-magnet, as described in Section 4.1.1.

The advantage of calculating the electro-magnetic force in this manner is that the flux leakage of the permanent-magnets is inherently catered for by the method. This is because the force is calculated by integrating the differential Lorentz force along the magnets' edges.

The disadvantage of the method is that in its most useful form, the saturation of the magnetic circuit is excluded. This may be accounted for by the inclusion of a saturation factor which linearly reduces the force production, and is calculated using a simplified magnetic circuit model.

The method was originally applied to flat linear machines in Cartesian co-ordinates[41], and further developed for tubular machines in cylindrical co-ordinates[42]. The derivation described by Wang et. al. considers the magnetic flux density of the permanent-magnets acting on the stator coils. The following derivation is based on the magnetic flux density of the stator coils acting on the permanent-magnets. This has been found to be a simpler solution to the problem as it eliminates the use of Green's functions to determine the MVP and limits the complexity of the solution to modified Bessel functions of the first and second kind.

4.3.1 The Magnetic Flux Density of the Stator Windings

The magnetic vector potential is a potential function \vec{A} , the *curl* of which defines the magnetic flux density, $\vec{B} = \nabla \times \vec{A}$ [43]. The resulting magnetic field vector describes the magnetic flux density at all points in the region.

The derivation of the magnetic vector potential is based on Figure 4.10 where the problem is simplified into a two-dimensional field distribution. This is valid because of the axial symmetry of the cylindrical system. The following assumptions are made in the use of this method[26]:

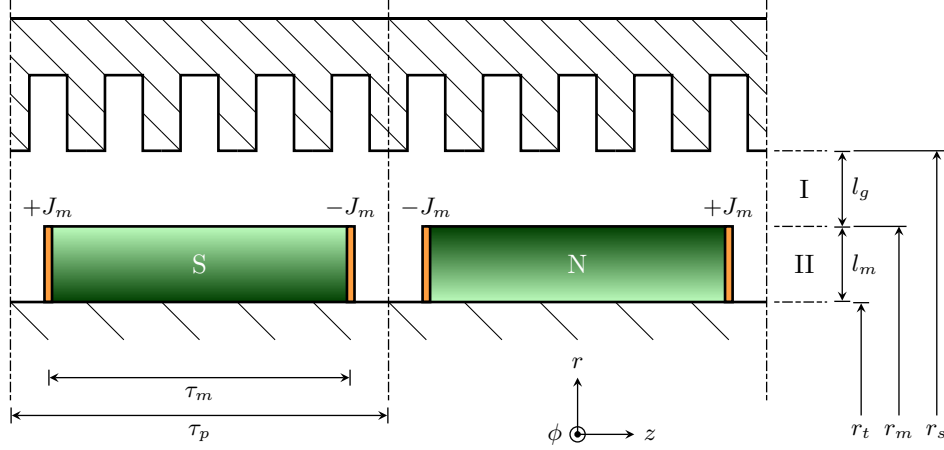


Figure 4.10: Model of a Linear Machine with Surface PMs for Two-Dimensional Magnetic Vector Potential Calculations.

1. Both the armature core and the translator core are represented by isotropic, slotless blocks with ideal electromagnetic properties, i.e.: infinite permeability and zero conductivity. The effects of slotting will be accounted for by an increased effective air-gap, according to Carter's coefficient. The effects of magnetic saturation will be accounted for by the inclusion of a saturation factor in the final solution.
2. The armature winding is represented by an infinitely thin current sheet, uniformly distributed on surface of the armature core. The armature line current flow is perpendicular to the plane, in the ϕ direction. The effects of the slot-leakage flux will be accounted for by the inclusion of a slot-leakage factor.
3. The permanent-magnets are represented by equivalent coils, as discussed in Section 4.1.

The time-space distribution of the armature line current is given by the first derivative of the mmf distribution with respect to z . For harmonic orders $h = 2mk \pm 1$ this results in:

$$\begin{aligned} a_h(z, t) &= \frac{d\mathcal{F}_h^\pm}{dz} = \frac{1}{2} \frac{4Q_h\tau_p}{\pi h} \cdot \frac{d}{dz} \cos(h\beta z \mp \tilde{\omega}_e t) \\ &= -2Q_h \sin(h\beta z \mp \tilde{\omega}_e t) \end{aligned} \quad (4.52)$$

The space distribution is given by setting $t = 0$:

$$a_h(z) = -2Q_h \sin(h\beta z) \quad (4.53)$$

The equivalent edge-current density which represents the permanent-magnets is given by Equation 4.10, and is repeated here as:

$$J_m = \frac{B_r}{u_0 u_{rrec}}$$

The magnetic vector potential in the air-gap and magnet regions (regions I and II respectively) is described by Laplace's equation for cylindrical co-ordinates[44]:

$$\begin{aligned} \nabla^2 \vec{A} &= 0 \\ \frac{1}{r} \frac{\partial}{\partial r} \left(r \frac{\partial \vec{A}}{\partial r} \right) + \frac{1}{r^2} \frac{\partial^2 \vec{A}}{\partial \theta^2} + \frac{\partial^2 \vec{A}}{\partial z^2} &= 0 \end{aligned} \quad (4.54)$$

The magnetic vector potential only has a component in the ϕ direction because the armature current flows perpendicularly to the $r - z$ plane. Using the method of separation of variables, and noting that the armature line current density is a real function, the space harmonic of \vec{A} in ϕ is given by Equation 4.55. The components of magnetic flux density in r and z are given by Equations 4.56 and 4.57 respectively.

$$A_{\phi h}(r, z) = \sin(h\beta z) \{A_h I_0(h\beta r) + B_h K_0(h\beta r)\} \quad (4.55)$$

$$B_{rh}(r, z) = -\frac{\partial A_{\phi h}}{\partial z} = -h\beta \cos(h\beta z) \{A_h I_0(h\beta r) + B_h K_0(h\beta r)\} \quad (4.56)$$

$$\begin{aligned} B_{zh}(r, z) &= \frac{1}{r} \frac{\partial(r A_{\phi h})}{\partial r} \\ &= \sin(h\beta z) \left[A_h \left(\frac{I_0(h\beta r)}{r} + h\beta I_1(h\beta r) \right) + B_h \left(\frac{K_0(h\beta r)}{r} - h\beta K_1(h\beta r) \right) \right] \end{aligned} \quad (4.57)$$

The description of $A_{\phi h}$ requires the two constants A_h and B_h to be defined for both regions I and II. This is achieved through the simultaneous solution of four boundary conditions. These boundary conditions define the magnetic flux density relationships at the material boundaries.

In the definition of the boundary equations, the arguments to the modified Bessel functions are removed for simplicity. At the surface of the armature, the infinite permeability of the core results in $B_{zhI}(r = r_s, z)/\mu_0 = a(z)/(k_{sl}k_{sat})$, which defines the first boundary condition as in Equation 4.58. At the magnet/air boundary, $B_{zhI}(r = r_m, z)/\mu_0 = B_{zhII}(r = r_m, z)/\mu_0 \mu_{rrec}$ and $B_{rhI}(r = r_m, z) = B_{rhII}(r = r_m, z)$ resulting in the second and third boundary conditions in Equations 4.59 and 4.60 respectively. Finally, at the translator core surface, the infinite permeability of the core results in $B_{zhII}(r = r_t, z) = 0$, and the final boundary condition in Equation 4.61.

$$\frac{-2\mu_0 Q_h}{k_{sl}k_{sat}} = A_{hI} \left[\frac{I_0}{r} + h\beta I_1 \right] + B_{hI} \left[\frac{K_0}{r} - h\beta K_1 \right] \Big|_{r=r_s} \quad (4.58)$$

$$\frac{A_{hII}}{\mu_{rrec}} \left[\frac{I_0}{r} + h\beta I_1 \right] + \frac{B_{hII}}{\mu_{rrec}} \left[\frac{K_0}{r} - h\beta K_1 \right] = A_{hI} \left[\frac{I_0}{r} + h\beta I_1 \right] + B_{hI} \left[\frac{K_0}{r} - h\beta K_1 \right] \Big|_{r=r_m} \quad (4.59)$$

$$A_{hI} I_0 + B_{hI} K_0 = A_{hII} I_0 + B_{hII} K_0 \Big|_{r=r_m} \quad (4.60)$$

$$A_{hII} \left[\frac{I_0}{r} + h\beta I_1 \right] + B_{hII} \left[\frac{K_0}{r} - h\beta K_1 \right] = 0 \Big|_{r=r_t} \quad (4.61)$$

The solution to this set of equations will define A_{hI} , B_{hI} , A_{hII} and B_{hII} . The resulting equations are very large, and so for conciseness, only the form of A_{hII} and B_{hII} are presented, as these are of significance in the subsequent derivation of the electro-magnetic force. The final solutions to A_{hII} and B_{hII} are given in Equations 4.62 and 4.63 respectively.

$$A_{hII} = + \frac{2h\beta Q_h \mu_0 \mu_{rrec}}{k_{sl} k_{sat}} C_{hII} \left[\frac{K_0(h\beta r_t)}{r_t} - h\beta K_1(h\beta r_t) \right] \quad (4.62)$$

$$B_{hII} = - \frac{2h\beta Q_h \mu_0 \mu_{rrec}}{k_{sl} k_{sat}} C_{hII} \left[\frac{I_0(h\beta r_t)}{r_t} + h\beta I_1(h\beta r_t) \right] \quad (4.63)$$

C_{hII} is that portion of Bessel functions which is common to the solutions of A_{hII} and B_{hII} . C_{hII} is too extensive to document, but is readily determined by solving the set of simultaneous equations and matching the solutions for A_{hII} and B_{hII} to the forms shown in Equations 4.62 and 4.63.

4.3.2 The Force of the Stator Acting on the Translator

The one edge of a permanent-magnet, at $z = 0.5\tau_m - \delta$, is represented by the edge-current density of $+J_m$. The second edge, at $z = -0.5\tau_m - \delta$, is represented by the edge-current density $-J_m$. The electromagnetic force of interest is along the z axis. The armature current flows only in the ϕ axis. Therefore, only the magnetic flux density along the r axis is of importance according to Lorentz' force shown in Equation 4.51. The incremental force acting over the length dr of an edge is $d\hat{F}_{eh}(\delta) = B_{rhII}(r, z = \pm 0.5\tau_m - \delta)(\pm J_m) \times (2\pi r)dr$. The total force acting over the entire length of the magnet's edge is:

$$\begin{aligned} \hat{F}_{eh}(\delta) &= \int_{r_t}^{r_m} dF_{eh}(r, z = \pm 0.5\tau_m - \delta) \\ &= \int_{r_t}^{r_m} -h\beta(2\pi r)(\pm J_m) \cos\left(\pm h\frac{\alpha_m\pi}{2} - h\beta\delta\right) [A_{hII}I_0(h\beta r) + B_{hII}K_0(h\beta r)] dr \\ &= -2\pi h\beta(\pm J_m) \cos\left(\pm h\frac{\alpha_m\pi}{2} - h\beta\delta\right) \left[A_{hII} \int_{r_t}^{r_m} rI_0(h\beta r)dr + B_{hII} \int_{r_t}^{r_m} rK_0(h\beta r)dr \right] \end{aligned} \quad (4.64)$$

The integrals may be evaluated given the recurrence relations of the modified Bessel functions in Equations 4.65 and 4.66[44]. The resulting expression for the total force acting over the entire length of the magnet's edge as in Equation 4.67:

$$\int rI_0(h\beta r)dr = \frac{rI_1(h\beta r)}{h\beta} \quad (4.65)$$

$$\int rK_0(h\beta r)dr = -\frac{rK_1(h\beta r)}{h\beta} \quad (4.66)$$

$$\hat{F}_{eh}(\delta) = -2\pi(\pm J_m)K_{hII} \cos\left(\pm h\frac{\alpha_m\pi}{2} - h\beta\delta\right) \quad (4.67)$$

where : $K_{hII} = [A_{hII}\{r_m I_1(h\beta r_m) - r_t I_1(h\beta r_t)\} + B_{hII}\{r_t K_1(h\beta r_t) - r_m K_1(h\beta r_m)\}]$

The force acting on a single magnet is therefore the sum of the force acting on the leading and trailing edges of the magnet at $z = \pm 0.5\tau_m - \delta$. Making use of the trigonometric identity $\cos(A \pm B) = \cos A \cos B \mp \sin A \sin B$ [44]:

$$\begin{aligned}\hat{F}_{mh}(\delta) &= -2\pi J_m K_{hII} \times \left[\cos\left(h\frac{\alpha_m\pi}{2} - h\beta\delta\right) - \cos\left(h\frac{\alpha_m\pi}{2} + h\beta\delta\right) \right] \\ &= -4\pi J_m K_{hII} \times \sin\left(h\frac{\alpha_m\pi}{2}\right) \sin(h\beta\delta)\end{aligned}\quad (4.68)$$

For p poles, the total force is p times the individual magnet force:

$$\hat{F}_h(\delta) = p \times F_{mh} = -4\pi p J_m K_{hII} \sin\left(h\frac{\alpha_m\pi}{2}\right) \sin(h\beta\delta)\quad (4.69)$$

4.3.3 Minimisation of the Harmonic Force Ripple

The individual force harmonics may be calculated according to Equation 4.69. No triplen harmonic forces will exist because of the three-phase stator windings. The harmonic force ripple may be expressed as[45]:

$$TFR = \frac{1}{F_1} \sqrt{\sum_h F_h^2}\quad (4.70)$$

$$h = 2mk \pm 1, k \in \mathbb{N}$$

The next highest force component is the fifth harmonic. Then follows the seventh, eleventh, thirteenth and so on. To minimise the total force ripple without affecting the force capability of the machine, the value of α_m may be adjusted to remove said harmonics, but keeping it as close to 1.0 as possible. It may be shown that the optimal value of α_m is 0.8 which effectively eliminates the fifth harmonic force component. This is intuitively appropriate given that the fifth harmonic is the largest contributor to the force ripple.

4.4 Magnetic Circuit

Defining the amount of magnetic flux which links with the stator coils is the most difficult task in the design or analysis of a machine. The total flux in the system is comprised of the active flux, the harmonic leakage flux and the spatial leakage flux. Both the leakage flux and the saturation of the magnetic circuit reduce the amount of active flux.

Calculating the active flux may be achieved through modelling the magnetic circuit using lumped components of mmf and reluctance. However, this requires an accurate definition of the various flux paths in the system, which is not always possible nor entirely accurate.

The active flux is a direct factor of the force in Equation 4.34. This requires a high level of accuracy in the magnetic modelling in order to accurately determine the force using this equation. The active flux is an indirect factor of the force in the MVP force equation, Equation 4.69. The active flux only affects the saturation factor, which in turn affects the

force calculation. Therefore, the variation of the force with active flux using the MVP method is significantly smaller than when using the induced *emf* method.

4.4.1 Simplified Magnetic Circuit

The primary reason for determining the active magnetic flux is to quantify the saturation of the magnetic circuit. The magnetic circuit may now be limited to the magnetic circuit of the active flux path, eliminating the parasitic reluctances. The magnetic circuit for the active magnetic flux is shown in Figure 4.11. It is governed by the magnetic analogue of Ohm's law as expressed by $\mathcal{F} = \Phi\mathcal{R}$.

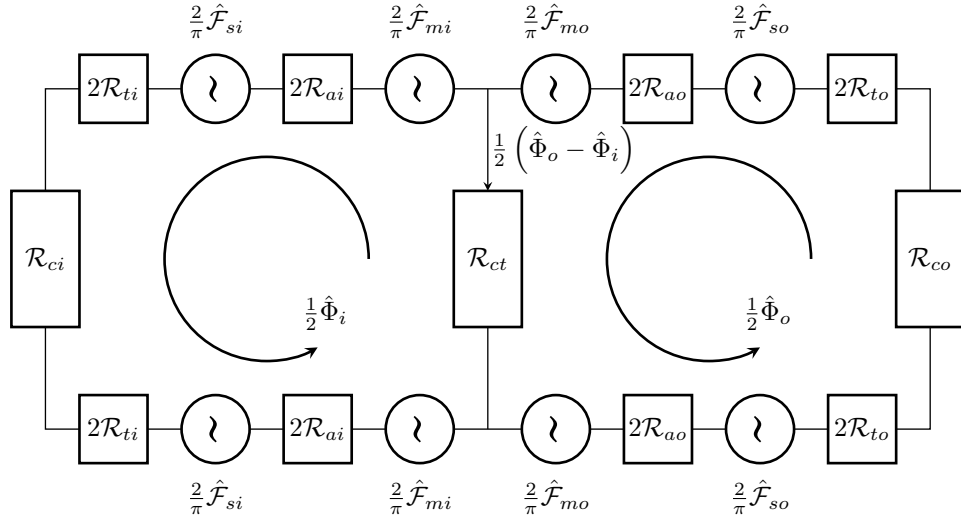


Figure 4.11: Magnetic Circuit per Pole of the Active Flux Component. The ferromagnetic reluctances are included and are functions of the flux passing through them. This facilitates the modelling of the magnetic circuit saturation.

This circuit represents a single pole-pitch, taken from the centre of one magnet, through to the centre of the next. This is done because the active flux from each pole will typically split axially in the cores, such that half the flux passes in the $+z$ direction and the remaining half through the $-z$ direction. The reluctances \mathcal{R}_t and \mathcal{R}_a are calculated across a full pole-pitch, and so the values for each half of the pole-pitch are doubled.

The resultant *mmfs* in the air-gaps are expressed by Equation 4.37 as $\hat{\mathcal{F}} = \sqrt{\hat{\mathcal{F}}_m^2 + \hat{\mathcal{F}}_s^2}$. The magnetic circuit equations for the inner and outer loops, after simplification and in terms of peak values, are given in Equations 4.71 and 4.72 respectively.

$$\frac{2}{\pi} \times 4\hat{\mathcal{F}}_i = \hat{\Phi}_i \times (4\mathcal{R}_{ai} + 4\mathcal{R}_{ti} + \mathcal{R}_{ci} + \mathcal{R}_{ct}) - \hat{\Phi}_o \times \mathcal{R}_{ct} \quad (4.71)$$

$$\frac{2}{\pi} \times 4\hat{\mathcal{F}}_o = \hat{\Phi}_o \times (4\mathcal{R}_{ao} + 4\mathcal{R}_{to} + \mathcal{R}_{ci} + \mathcal{R}_{ct}) - \hat{\Phi}_i \times \mathcal{R}_{ct} \quad (4.72)$$

4.4.2 Magnetic Flux Linkage

Equation 4.34 defines the force in terms of the active magnetic flux; Equation 4.69 defines the force in terms of the MVP of the stator windings. By equating the two equations, and placing $\hat{\Phi}_h$ as the subject of the equation, we may determine the active flux component as a function of the MVP force calculation. In this manner, we eliminate the complexity, variability and inaccuracy of determining the active flux completely through magnetic circuit modelling:

$$\begin{aligned}
 F_{h\text{-induced emf}} &= F_{h\text{-mvp}} \\
 \frac{\pi L}{2\tau_p} Q_h \hat{\Phi}_h &= -4\pi p J_m K_{hII} \sin\left(h \frac{\alpha_m \pi}{2}\right) \sin(h\beta\delta) \\
 \therefore \hat{\Phi}_h &= -\frac{8J_m K_{hII}}{Q_h} \sin\left(h \frac{\alpha_m \pi}{2}\right) \sin(h\beta\delta) \quad (4.73)
 \end{aligned}$$

The value of $\hat{\Phi}_h$, as shown in Equation 4.73 represents the total flux linkage per pole for the h^{th} harmonic. Importantly this value takes into consideration the effects of permanent-magnet flux leakage: the inclusion of an effective air-gap such that $g = k_c g'$ takes account of the slotting, and the definition of the stator windings' magnetic vector potential considers the effect of slot leakage using k_{sl} and the saturation of the magnetic circuit, using k_{sat} . Therefore, the value of $\hat{\Phi}_h$, as shown in Equation 4.73 results in a fairly accurate evaluation of the harmonic flux linkage including all parasitic effects.

4.4.3 Total Magnetic Flux per Pole

The relationship between the total linked flux per-pole and the fundamental component of this linked flux must be established. The total flux per pole is required in the derivation of the magnetic saturation of the magnetic circuit. The total magnetic flux per pole is the sum of the individual harmonic components $\hat{\Phi}_h$ taking note of the harmonic phase angles: $\hat{\Phi} = \sum_h \hat{\Phi}_h$.

Although this sum should consider an infinite sum of harmonics, only the lower harmonics cross the air-gap. Higher harmonics have wavelengths which become comparable to the air-gap length. These flux components do not cross the air-gap but rather leak back to the translator core. A decision must be made as to a suitable limit to this sum to more accurately reflect the harmonics which truly cross the air-gap and contribute to the tooth and core saturation. Typically, one should limit this to the third, fifth and possibly the seventh harmonic.

Although triplen harmonics are excluded in the force calculation because of the three-phase winding arrangement, they cannot be excluded from the total magnetic circuit flux. The total flux which links with the stator still includes these triplen harmonics; their effects are simply cancelled out through the stator windings' three-phase connections.

The resulting factor of total flux per pole versus the fundamental is given in Equation 4.74. Typical values for k_Φ range between 1.0 and 1.5.

$$k_\Phi = \frac{\hat{\Phi}}{\hat{\Phi}_1} = \frac{\sum_h \hat{\Phi}_h}{\hat{\Phi}_1} \quad (4.74)$$

4.4.4 The Effective Air-gap

The effects of slotting may be accounted for by extending the mechanical air-gap to an effective air-gap according to:

$$g = k_c g' \quad (4.75)$$

Carter's coefficient is employed in modelling the effective air-gap dimensions[30]. A representative diagram of how this factor affects the air-gap dimensions is shown in Figure 4.12.

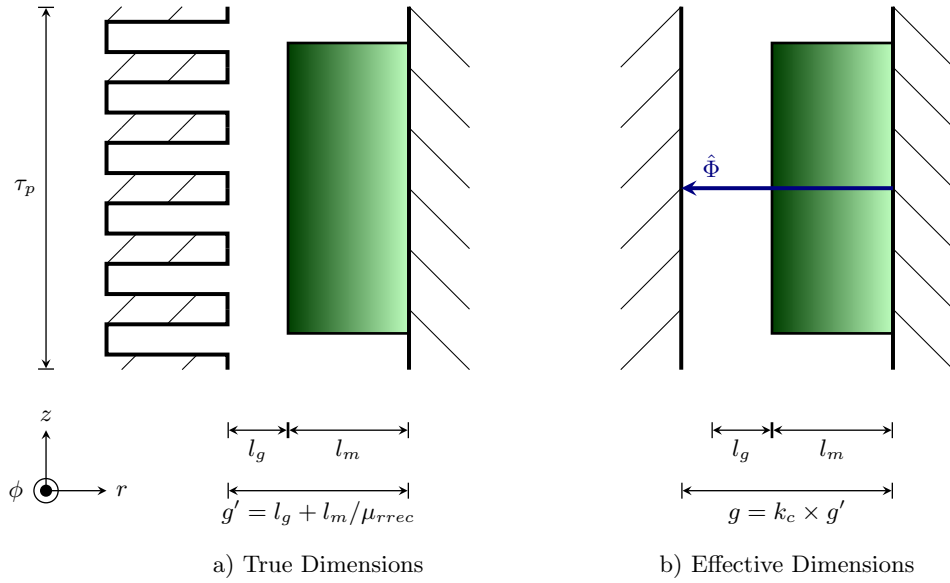


Figure 4.12: The mechanical air-gap length is modified by Carter's coefficient to account for the increased flux paths which results from the slotting.

In essence, the length is increased so as to account for the different flux path between a slot region and a tooth region. This coefficient is calculated in Equation 4.76.

$$k_c = \frac{\tau_{sl} + \tau_t}{(\tau_{sl} + \tau_t) - \gamma_g g'} \quad (4.76)$$

Where : $\gamma_g = \frac{4}{\pi} \left(y \arctan y - \ln \left(\sqrt{1 + y^2} \right) \right)$
and $y = \frac{\tau_o}{2g'}$

For the purposes of this model, two different mechanical lengths are used. For the MVP method, the length of the air-gap alone is used, $g' = l_g$. For the reluctance of the air-gap in the magnetic circuit, the sum of the air-gap length and the effective magnet thickness is used, and is represented by $g' = l_g + l_m / \mu_{rrec}$.

4.4.5 Saturation Factor, k_{sat}

The saturation factor is the factor by which the air-gap reluctance is increased such that, when exposed to the resultant mmf , it will produce the same magnetic flux as when the full magnetic circuit is exposed to the resultant mmf . Consider for a moment the inner magnetic circuit as expressed by Equation 4.71:

$$\frac{2}{\pi} \times 4\hat{\mathcal{F}}_i = \hat{\Phi}_i \times (4\mathcal{R}_{ai} + 4\mathcal{R}_{ti} + \mathcal{R}_{ci} + \mathcal{R}_{ct}) - \hat{\Phi}_o \times \mathcal{R}_{ct}$$

Using a saturation factor, k_{sati} , the magnetic circuit equation may be reduced to:

$$\frac{2}{\pi} \times 4\hat{\mathcal{F}}_i = \hat{\Phi}_i \times (4k_{sati}\mathcal{R}_{ai}) \quad (4.77)$$

The definition of the saturation factor is given by equating the right-hand sides of these two equations:

$$\begin{aligned} \hat{\Phi}_i \times (4k_{sati}\mathcal{R}_{ai}) &= \hat{\Phi}_i \times (4\mathcal{R}_{ai} + 4\mathcal{R}_{ti} + \mathcal{R}_{ci} + \mathcal{R}_{ct}) - \hat{\Phi}_o \times \mathcal{R}_{ct} \\ \therefore k_{sati} &= 1 + \frac{4\mathcal{R}_{ti} + \mathcal{R}_{ci} + (1 - C_{\Phi})\mathcal{R}_{ct}}{4\mathcal{R}_{ai}} \end{aligned} \quad (4.78)$$

$$\text{Similarly : } k_{sato} = 1 + \frac{4\mathcal{R}_{to} + \mathcal{R}_{co} + (1 - C_{\Phi}^{-1})\mathcal{R}_{ct}}{4\mathcal{R}_{ao}} \quad (4.79)$$

$$\text{where : } C_{\Phi} = \frac{\hat{\Phi}_o}{\hat{\Phi}_i}$$

4.4.6 Slot Leakage Factor, k_{sl}

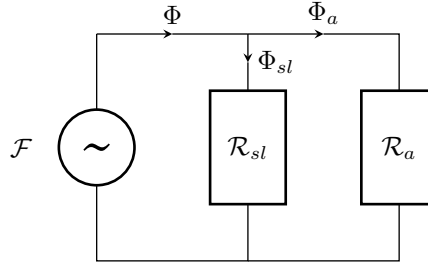


Figure 4.13: Simplified Magnetic Circuit including Slot-Leakage.

The saturation of the magnetic circuit is excluded in the determination of the slot-leakage factor. This is because it is already accounted for in the definition of k_{sat} . Consider Figure 4.13 which shows a generic and simplified magnetic circuit which includes a reluctance for the slot-leakage. The mmf , \mathcal{F} , develops a flux, Φ , which is split between the slot-leakage reluctance and the air-gap reluctance.

We define the slot-leakage factor as the ratio of the total magnetic flux, Φ , developed by

the mmf through the total reluctance, to the air-gap flux of Φ_a :

$$\begin{aligned}
 \mathcal{F} &= \Phi (\mathcal{R}_{sl} || \mathcal{R}_a) \\
 &= \Phi \frac{\mathcal{R}_{sl} \mathcal{R}_a}{\mathcal{R}_{sl} + \mathcal{R}_a} \\
 \text{But : } \mathcal{F} &= \Phi_a \mathcal{R}_a \\
 \therefore \Phi_a \mathcal{R}_a &= \Phi \frac{\mathcal{R}_{sl} \mathcal{R}_a}{\mathcal{R}_{sl} + \mathcal{R}_a} \\
 \therefore k_{sl} &= \frac{\mathcal{R}_{sl} + \mathcal{R}_a}{\mathcal{R}_{sl}} \tag{4.80}
 \end{aligned}$$

4.4.7 Reluctances

The reluctances of the individual sections of the magnetic circuit are modelled from first principles. In some cases a mean path and area are used instead of integration so as to reduce the complexity. The saturation of the ferromagnetic components will be modelled using the approximated B-H characteristic derived in Section 4.1.2. The reluctances which are modelled are:

1. \mathcal{R}_a - The Air-gaps Including the Effective Magnet Lengths
2. \mathcal{R}_{ct} - The Translator Core
3. \mathcal{R}_c - The Stator Cores
4. \mathcal{R}_t - The Teeth
5. \mathcal{R}_{sl} - The Slot Leakage

In the case of the reluctances of the air-gaps, the permeability, μ , is simply the permeability of free space, $\mu_0 = 4\pi \times 10^{-7}$. In the case of the ferromagnetic material, we recall from Section 4.1.2 that the permeability may be expressed by Equation 4.17 as:

$$\mu_r(B) = \frac{1}{k_{\mu 1} B^{n_{\mu 1}} + k_{\mu 2} B^{n_{\mu 2}}}$$

The Air-gap Reluctances

The reluctance of an air-gap region, as depicted in Figure 4.14, is expressed as an integral and simplified as follows:

$$\begin{aligned}
 \mathcal{R}_a &= \int_{r_1}^{r_2} \frac{dr}{\mu_0 2\pi r \tau_p} \\
 &= \frac{\ln\left(\frac{r_2}{r_1}\right)}{2\pi \mu_0 \tau_p} \tag{4.81}
 \end{aligned}$$

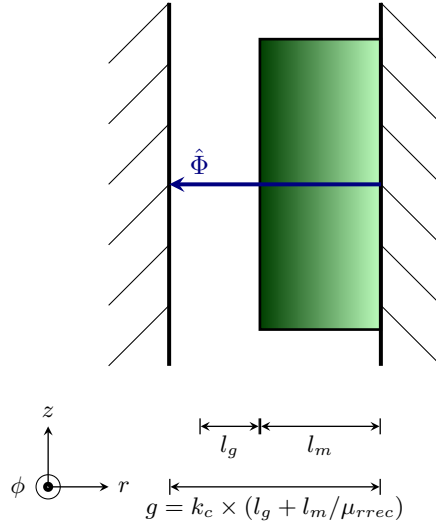


Figure 4.14: Model of the Air-gap and the Effective Magnet Length. The air-gap length is modified by Carter’s coefficient to account for the increased flux paths resulting from the slotting.

The radii r_2 and r_1 are defined differently according to the air-gap region:

$$\text{For } \mathcal{R}_{ai} : r_1 = r_i - g$$

$$r_2 = r_i$$

$$\text{For } \mathcal{R}_{ao} : r_1 = r_o$$

$$r_2 = r_o + g$$

$$\text{where : } g = k_c (l_g + l_m / \mu_{rrec})$$

The Translator Core Reluctance

The section of the translator core which is to be modelled is shown in Figure 4.15. The tubular nature of the device will result in the outer circuit’s flux being greater than that of the inner circuit. Therefore, the flux through the translator core is the difference between these two as shown in the magnetic circuit, Figure 4.11.

The reluctance of this portion of the magnetic circuit is negligible. However, it must be included because it affects the values of the saturation factors. The relatively close proximity of r_i to r_o means that a linear approximation of the depth of the material may be made. If this were not simplified in this manner, then the analytical expression would become cluttered with integrals, the benefits of which would not be realisable. We resort to approximating the reluctance with the aid of a mean path and a mean area, being l and A

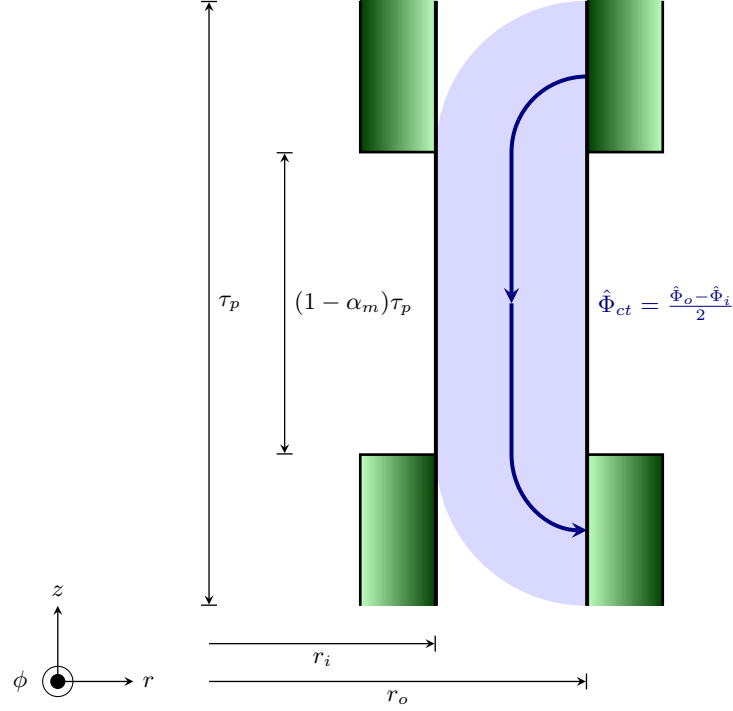


Figure 4.15: Model of the Translator Core. The outer flux will always be greater than the inner flux because of the tubular nature of the machine. Therefore, the flux tube is drawn arcing toward the outer air-gap

respectively. The reluctance is therefore expressed as:

$$\mathcal{R}_{ct} = \frac{l}{\mu A} = \frac{l}{\mu_0 \mu_r(B) \times A}$$

$$\text{Now : } \mu_r(B) = \frac{1}{k_{\mu 1} B^{n_{\mu 1}} + k_{\mu 2} B^{n_{\mu 2}}}$$

$$l = (1 - \alpha_m) \tau_p + \pi(r_i + r_o)$$

$$A = \pi(r_o^2 - r_i^2)$$

$$B = \frac{\hat{\Phi}_{ct}}{A}$$

$$\text{and : } \hat{\Phi}_{ct} = \frac{\hat{\Phi}_o - \hat{\Phi}_i}{2}$$

$$\therefore \mathcal{R}_{ct} = \frac{l}{\mu_0 A} \cdot \frac{k_{\mu 1} B^{n_{\mu 1}} + k_{\mu 2} B^{n_{\mu 2}}}{1}$$

$$= \frac{l}{\mu_0} \left[\frac{k_{\mu 1} \hat{\Phi}_{ct}^{n_{\mu 1}}}{A^{n_{\mu 1} + 1}} + \frac{k_{\mu 2} \hat{\Phi}_{ct}^{n_{\mu 2}}}{A^{n_{\mu 2} + 1}} \right]$$

The Stator Core Reluctances

Like the translator core, the flux is able to distribute relatively uniformly in the ferromagnetic core. The regions for which expressions for reluctances will be derived are shown in Figure 4.16. There exist four regions through which the flux passes, A through D. It is evi-

dent however that regions A and D are identical and regions B and C are likewise identical. The total reluctance of the core may thus be shown to be $\mathcal{R}_c = 2 \times (\mathcal{R}_A + \mathcal{R}_B)$.

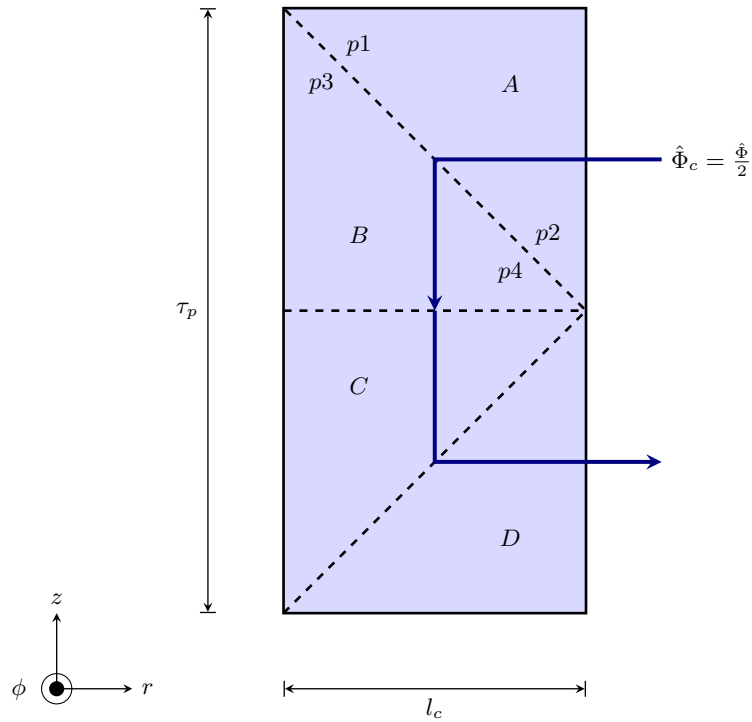


Figure 4.16: Model of the Flux Path through the Stator Core.

In the calculation of \mathcal{R}_A we use one simplification. The radial nature of the machine means that the saturation at points $p1$ and $p2$ are not linearly different. Thus the mean path does not exactly lead to the mean reluctance. However, this is in the region of the core which will experience the lowest flux density. The stator cores are restricted in their radial length l_c , and so the axial flux density will be significantly larger than than radial flux density. The radial flux density will be approximately the same as the air-gap flux density, concentrated only by the ratio of the radii at which they exist. It is therefore unlikely that regions A and D would in fact saturate, but it is noted here for completeness. The reluctances \mathcal{R}_A and \mathcal{R}_B are given in Equations 4.82 and 4.83 respectively, resulting in the total core reluctance

in Equation 4.84.

$$\begin{aligned}
\mathcal{R}_A &= \int_{r_1}^{r_2} \frac{dr}{\mu_0 \mu_r(B(r)) \times A(r)} \\
&= \frac{1}{\mu_0} \int_{r_1}^{r_2} \frac{1}{A(r)} \cdot \frac{k_{\mu 1} B(r)^{n_{\mu 1}} + k_{\mu 2} B(r)^{n_{\mu 2}}}{1} dr \\
B(r) &= \frac{\hat{\Phi}_c}{A(r)} = \frac{\hat{\Phi}}{2A(r)} \\
\therefore \mathcal{R}_A &= \frac{1}{\mu_0} \left[\int_{r_1}^{r_2} \frac{k_{\mu 1} \hat{\Phi}^{n_{\mu 1}}}{2^{n_{\mu 1}} A(r)^{n_{\mu 1}+1}} dr + \int_{r_1}^{r_2} \frac{k_{\mu 2} \hat{\Phi}^{n_{\mu 2}}}{2^{n_{\mu 2}} A(r)^{n_{\mu 2}+1}} dr \right] \\
&= \frac{k_{\mu 1} \hat{\Phi}^{n_{\mu 1}}}{2^{n_{\mu 1}} \mu_0} \int_{r_1}^{r_2} \frac{dr}{A(r)^{n_{\mu 1}+1}} + \frac{k_{\mu 2} \hat{\Phi}^{n_{\mu 2}}}{2^{n_{\mu 2}} \mu_0} \int_{r_1}^{r_2} \frac{dr}{A(r)^{n_{\mu 2}+1}} \\
\text{Given : } A(r) &= 2\pi r k_{st} \left(\frac{\tau_p}{2} \right) = \pi \tau_p r k_{st} \\
\mathcal{R}_A &= \frac{k_{\mu 1} \hat{\Phi}^{n_{\mu 1}}}{2^{n_{\mu 1}} \mu_0 (\pi \tau_p k_{st})^{n_{\mu 1}+1}} \int_{r_1}^{r_2} \frac{dr}{r^{n_{\mu 1}+1}} + \frac{k_{\mu 2} \hat{\Phi}^{n_{\mu 2}}}{2^{n_{\mu 2}} \mu_0 (\pi \tau_p k_{st})^{n_{\mu 2}+1}} \int_{r_1}^{r_2} \frac{dr}{r^{n_{\mu 2}+1}} \\
\mathcal{R}_A &= \frac{-k_{\mu 1} \hat{\Phi}^{n_{\mu 1}} \left[r_2^{-n_{\mu 1}} - r_1^{-n_{\mu 1}} \right]}{2^{n_{\mu 1}} n_{\mu 1} \mu_0 (\pi \tau_p k_{st})^{n_{\mu 1}+1}} + \frac{-k_{\mu 2} \hat{\Phi}^{n_{\mu 2}} \left[r_2^{-n_{\mu 2}} - r_1^{-n_{\mu 2}} \right]}{2^{n_{\mu 2}} n_{\mu 2} \mu_0 (\pi \tau_p k_{st})^{n_{\mu 2}+1}} \quad (4.82)
\end{aligned}$$

$$\text{For } \mathcal{R}_{Ai}: r_1 = r_i - l_m - l_g - k_{li} Q_i - \frac{l_{ci}}{2}$$

$$r_2 = r_i - l_m - l_g - k_{li} Q_i$$

$$\text{For } \mathcal{R}_{Ao}: r_1 = r_o + l_m + l_g + k_{lo} Q_o$$

$$r_2 = r_o + l_m + l_g + k_{lo} Q_o + \frac{l_{co}}{2}$$

Unlike \mathcal{R}_A , the flux passing through region B flows axially. The flux is therefore not concentrated as the radius changes. This suggests that the permeability does not differ through region B, ie: the permeability at $p3$ and $p4$ is equal. We can therefore reduce the area to a mean length of $l = \tau_p/4$ and a mean area of $A = \pi(r_4^2 - r_3^2)$:

$$\begin{aligned}
\mathcal{R}_B &= \frac{l}{\mu_0 \mu_r(B) A} \\
B &= \frac{\hat{\Phi}_c}{A} = \frac{\hat{\Phi}}{2A} \\
\therefore \mathcal{R}_B &= \frac{l}{\mu_0 A} \cdot \frac{k_{\mu 1} B^{n_{\mu 1}} + k_{\mu 2} B^{n_{\mu 2}}}{1} \\
&= \frac{l}{\mu_0} \left[\frac{k_{\mu 1} \hat{\Phi}^{n_{\mu 1}}}{2^{n_{\mu 1}} A^{n_{\mu 1}+1}} + \frac{k_{\mu 2} \hat{\Phi}^{n_{\mu 2}}}{2^{n_{\mu 2}} A^{n_{\mu 2}+1}} \right] \quad (4.83)
\end{aligned}$$

$$\text{where : } A = \pi(r_4^2 - r_3^2) k_{st}$$

$$l = \frac{\tau_p}{4}$$

$$\text{For } \mathcal{R}_{Bi}: r_3 = r_i - l_m - l_g - k_{li} Q_i - l_{ci}$$

$$r_4 = r_i - l_m - l_g - k_{li} Q_i$$

$$\text{For } \mathcal{R}_{Bo}: r_3 = r_o + l_m + l_g + k_{lo} Q_o$$

$$r_4 = r_o + l_m + l_g + k_{lo} Q_o + l_{co}$$

Finally, the combination of these reluctances forms the complete reluctance for each stator core:

$$\mathcal{R}_c = 2(\mathcal{R}_A + \mathcal{R}_B) \tag{4.84}$$

The Teeth Reluctances

The magnetic flux density in the teeth is assumed to vary only with radius. The distribution along the z axis is considered uniform. This is not entirely accurate. However, the flux will redistribute to a certain extent to achieve a mostly uniform distribution in z .

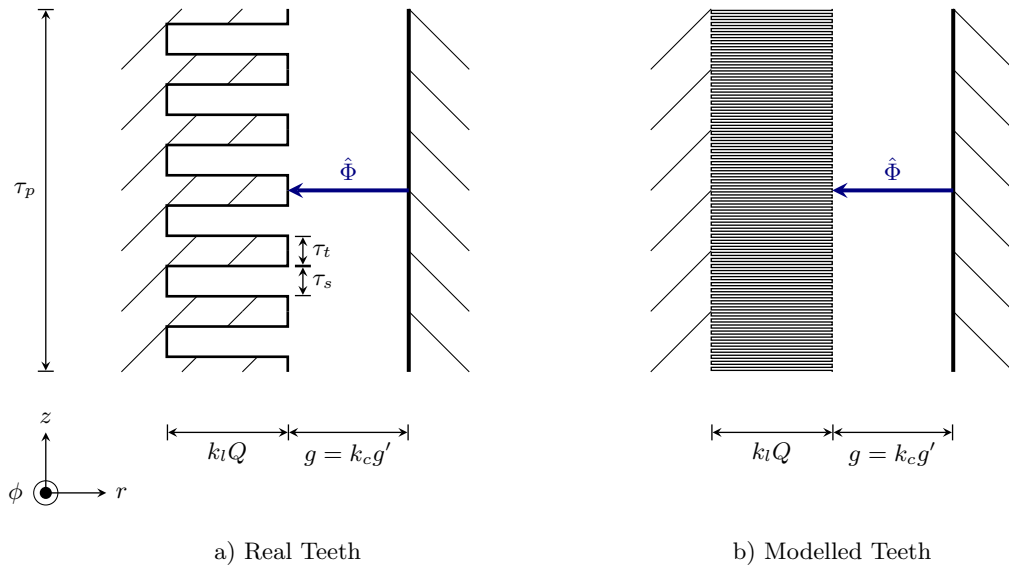


Figure 4.17: Model of the Stator Teeth Reluctance. The flux density varies with r but is considered uniform in z . The teeth are shown as discrete entities in a) but as infinitesimally small teeth in b) with a constant ratio of α_t defining the relationship between the teeth and the slots.

Figure 4.17 a) shows the region to be modelled. This model is obviously very dependant on the slot configuration. In order to develop a more generic description of the teeth reluctance, the teeth region is simplified to a region of infinitesimally small teeth, as shown in Figure 4.17 b). The ratio of $\alpha_t = \frac{\tau_t}{\tau_{sl} + \tau_t}$ is maintained in the analysis to show the effective area.

The reluctance of the teeth may now be described analytically beginning, as with the other reluctances, from first principles:

$$\mathcal{R}_t = \int_{r_1}^{r_2} \frac{dr}{\mu_0 \mu_r(B) \times A(r)}$$

$$\mathcal{R}_t = \frac{1}{\mu_0} \int_{r_1}^{r_2} \frac{1}{A(r)} \cdot \frac{k_{\mu 1} B(r)^{n_{\mu 1}} + k_{\mu 2} B(r)^{n_{\mu 2}}}{1} dr$$

$$\text{Where : } B(r) = \frac{\hat{\Phi}}{A(r)}$$

$$A(r) = 2\pi r \times \alpha_t k_{st} \tau_p$$

$$\therefore \mathcal{R}_t = \frac{1}{\mu_0} \left[\frac{k_{\mu 1} \hat{\Phi}^{n_{\mu 1}}}{(2\pi \alpha_t k_{st} \tau_p)^{n_{\mu 1} + 1}} \int_{r_1}^{r_2} \frac{dr}{r^{n_{\mu 1} + 1}} + \frac{k_{\mu 2} \hat{\Phi}^{n_{\mu 2}}}{(2\pi \alpha_t k_{st} \tau_p)^{n_{\mu 2} + 1}} \int_{r_1}^{r_2} \frac{dr}{r^{n_{\mu 2} + 1}} \right]$$

$$\mathcal{R}_t = \frac{-1}{\mu_0} \left[\frac{k_{\mu 1} \hat{\Phi}^{n_{\mu 1}} (r_2^{-n_{\mu 1}} - r_1^{-n_{\mu 1}})}{n_{\mu 1} (2\pi \alpha_t k_{st} \tau_p)^{n_{\mu 1} + 1}} + \frac{k_{\mu 2} \hat{\Phi}^{n_{\mu 2}} (r_2^{-n_{\mu 2}} - r_1^{-n_{\mu 2}})}{n_{\mu 2} (2\pi \alpha_t k_{st} \tau_p)^{n_{\mu 2} + 1}} \right] \quad (4.85)$$

$$\text{For } \mathcal{R}_{ti}: r_1 = r_i - l_m - l_g - k_{li} Q_i$$

$$r_2 = r_i - l_m - l_g$$

$$\text{For } \mathcal{R}_{to}: r_1 = r_o + l_m + l_g$$

$$r_2 = r_o + l_m + l_g + k_{lo} Q_o$$

The Slot Leakage Reluctances

A typical semi-closed slot is comprised of four regions. This analysis is limited to a semi-closed slot as it is the most probable slot configuration which may be used in such a machine. The slot-leakage flux flows through and affects each slot individually. The contribution of the slot leakage per phase to the reduction of the active flux in the circuit is only through the slots which make up that phase. Therefore, the slot-leakage flux per phase is q (the number of slots per pole per phase) times that of the individual slot. The integration of this effect into an m -phase system is accounted for in the definitions of the harmonic *mmfs* for the poly-phase windings in Equations 4.49 and 4.50. Figure 4.18 shows the four regions and the parameters which are used in this derivation.

The total slot permeance is the sum of the permeances of the four regions. The resulting reluctance per pole is q times the inverse of the total permeance. The individual permeances are calculated in the following series of equations.

$$\Lambda_1 = \int_{r_4}^{r_5} \frac{\mu_0 \times 2\pi r dr}{\tau_o}$$

$$= \frac{\pi \mu_0}{\tau_o} (r_5^2 - r_4^2) \quad (4.86)$$

Region 2 is slightly more complex because of the tapering of the tooth. The tooth width may be represented by the equation of a straight line, $\tau = mr + c$, and incorporated into

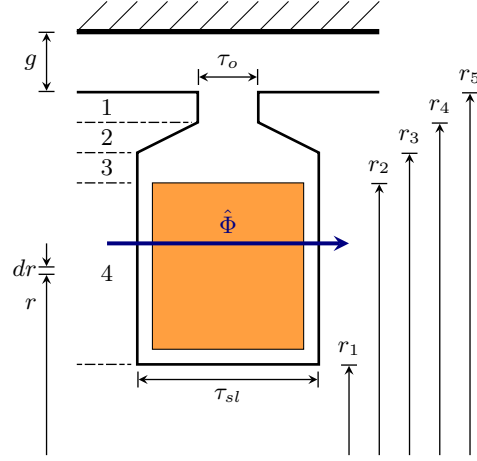


Figure 4.18: Model of a Stator Slot from Which the Equivalent Slot Permeance May Be Derived.

the calculation of Λ_2 . Integration by parts is used to arrive at the final solution:

$$\begin{aligned}\Lambda_2 &= \int_{r_3}^{r_4} \frac{\mu_0 \times 2\pi r dr}{mr + c} \\ &= \frac{2\pi\mu_0}{m^2} [\ln(mr + c)(2mr + c) - (mr + c)]_{r_3}^{r_4}\end{aligned}\quad (4.87)$$

$$\text{where : } m = \frac{\tau_{sl} - \tau_o}{r_3 - r_4}$$

$$\text{and : } c = \tau_{sl} - mr_3$$

The permeance of region 3 is derived in a similar fashion to Λ_1 :

$$\begin{aligned}\Lambda_3 &= \int_{r_2}^{r_3} \frac{\mu_0 \times 2\pi r dr}{\tau_{sl}} \\ &= \frac{\pi\mu_0}{\tau_{sl}} (r_3^2 - r_2^2)\end{aligned}\quad (4.88)$$

The region in which the coil exists, region 4, is the most complex. The amount of flux which links with the stator coil is proportional to the square of $(r - r_1)/(r_2 - r_1)$. This is because the mmf develops through the length of the conductor. The amount of flux passing through dr may be represented as[36]:

$$d\Phi = \mathcal{F}(r) \times d\Lambda = \frac{r - r_1}{r_2 - r_1} NI \times \frac{\mu_0 2\pi r dr}{\tau_{sl}}\quad (4.89)$$

This portion of magnetic flux only links with the stator coils between r_1 and r according to $d\lambda = (r - r_1)/(r_2 - r_1)N \times d\Phi$. The flux linkage is determined by integrating $d\lambda$ over r :

$$\begin{aligned}d\lambda &= \left(\frac{r - r_1}{r_2 - r_1} N \right)^2 I \times \frac{\mu_0 2\pi r dr}{\tau_{sl}} \\ \therefore \lambda &= \frac{2\pi\mu_0 N^2 I}{\tau_{sl} (r_2 - r_1)^2} \int_{r_1}^{r_2} r (r - r_1)^2 dr \\ &= \frac{2\pi\mu_0 N^2 I}{\tau_{sl} (r_2 - r_1)^2} \cdot \frac{(r - r_1)^3 (3r + r_1)}{12} \Big|_{r_1}^{r_2} \\ &= \frac{\pi\mu_0}{6\tau_{sl}} N^2 I (3r_2^2 - 2r_1 r_2 - r_1^2)\end{aligned}$$

The final expression for Λ_4 is found by extracting the N^2I factor out of the flux linkage, noting that $\lambda = N^2I\Lambda$:

$$\Lambda_4 = \frac{\pi\mu_0}{6\tau_{sl}}(3r_2^2 - 2r_1r_2 - r_1^2) \quad (4.90)$$

The total permeance of a single slot is $\Lambda_{sl} = \Lambda_1 + \Lambda_2 + \Lambda_3 + \Lambda_4$. There are q slots per pole per phase. Therefore, the total slot reluctance per pole is given by Equation 4.91:

$$\mathcal{R}_{sl} = \frac{q}{\Lambda_{sl}} = \frac{q}{\Lambda_1 + \Lambda_2 + \Lambda_3 + \Lambda_4} \quad (4.91)$$

4.5 Mechanical Considerations

4.5.1 Stator Core Constraints

To prevent saturation in the core, and to determine the slot and core dimensions, equations based on core saturation will be used. The peak flux density in the core, \hat{B}_c , is chosen to be roughly $1.5T - 1.8T$ so as to prevent excessive core saturation[36]. It follows that:

$$\hat{B}_c = \frac{\hat{\Phi}}{2A_c} \quad (4.92)$$

given:

$$A_{ci} = \pi (r_i - l_m - l_g - k_{li}Q_i)^2 - \pi (r_i - l_m - l_g - k_{li}Q_i - l_{ci})^2 \quad (4.93)$$

$$A_{co} = \pi (r_o + l_m + l_g + k_{lo}Q_o + l_{co})^2 - \pi (r_o + l_m + l_g + k_{lo}Q_o)^2 \quad (4.94)$$

These equations introduce four variables, k_{li} , k_{lo} , l_{ci} and l_{co} , which allow for the depths of the laminations, l_s , to be written in terms of Q . This is accomplished by relating the area of the slots to the current in the coils.

$$\begin{aligned} A_{st} &= \frac{I_{ph}}{J} \\ N_{sl} &= \frac{N_{ph}}{pq} \\ \therefore A_{sl} &= \frac{A_{st} \times N_{sl}}{k_{fill}} \end{aligned}$$

$$\text{But : } A_{sl} = l_{sl} \times \frac{\tau_p \alpha_{sl}}{mq}$$

$$\text{where : } \alpha_{sl} = 1 - \alpha_t$$

Using the definition of the Specific Electrical Loadings, we can equate the two expressions for slot area and eliminate the current and series-turns variables such that:

$$l_{sl} = \frac{1}{k_w k_{fill} J \alpha_{sl}} Q = k_l Q \quad (4.95)$$

The stator lengths are thus defined by Equation 4.96, where k_l may be calculated from given parameters for each stator, and l_{ci} and l_{co} are two of the variables to be solved for.

$$\begin{aligned} l_s &= \frac{1}{k_w k_{fill} J \alpha_{sl}} Q + l_c \\ l_s &= k_l Q + l_c \end{aligned} \quad (4.96)$$

4.5.2 Translator Core Constraints

The magnetic circuit is arranged so as to allow the flux to flow radially through the translator core. The small component of flux passing axially through the core is the only component which will be limited by the thickness of the translator core. The only other constraint on the core is therefore whether or not the tensile strength of the core is sufficient for the maximum force exerted on the translator. The mass of the translator, excluding external structures is:

$$m_t = \rho_m \times v_m + \rho_{ct} \times v_{ct} \quad (4.97)$$

$$\text{where : } v_{ct} = \pi \times (r_o^2 - r_i^2) \times L_t$$

$$v_m = \pi \{ [r_i^2 - (r_i - l_m)^2] + [(r_o + l_m)^2 - r_o^2] \} \alpha_m L_m$$

The largest tensile force on the translator occurs when the electromagnetic force is exerted vertically upwards on the translator. Thus, the peak force on the translator is $\hat{F}_{ct} = m_t g + \hat{F}$. A tensile pressure may be calculated according to Equation 4.98, and compared with the tensile strength of the steel, typically 350-840 MPa [46].

$$P_{ct} = \frac{F_{ct}}{\pi (r_o^2 - r_i^2)} \quad (4.98)$$

The densities of the steel and magnets may be taken as approximately 7850 Mg/m³[32] and 7400 Mg/m³[33] respectively. A suitable safety factor should be adopted. In the machine design presented in this research, a value of 25 MPa was chosen as the target tensile pressure in the translator core. Given that the quantification of torques on the translator are not considered, the direct quantification of the torsional effects is beyond the scope of the research.

4.6 Machine Design Procedure Using The Performance Calculations

The length of the machine is often determined by the application. In all cases, the pole-pitch should be as small as mechanically possible to maintain a high electrical frequency. Thus the axial dimensions are not of concern in the optimisation of a design, and are limited by the application.

The radial dimensions of the machine may however be optimised depending on the objective of the optimisation. At various radii, the electrical and magnetic loadings of the machine (Q and $\hat{\Phi}$ respectively) will vary. To accommodate this, the stator dimensions must be varied to maintain a suitable level of magnetic flux density in the teeth and cores, and current density in the slots.

Given a predefined force requirement, the magnetic flux per pole for the inner and outer stator will increase with increasing radius. The outer electrical loading Q_o will decrease with increasing radius and the inner electrical loading will increase with increasing radius. The machine's material volume will vary from a large value when the radius is smaller and the outer stator excessively large, through a minimum, and back toward another large value when the inner stator is excessively large.

Considering this characteristic, there are only two feasible objectives which may be chosen in the optimisation of any design:

- To achieve equality between the electrical loadings of the two stators ($Q_i = Q_o$), and
- To achieve the lowest machine volume, which will typically result in $Q_o > Q_i$.

The design script was programmed in the Mathematica[®] language, primarily because of the reliability of the *Solve* method which it implements[47]. The inner translator radius was parametrised such that various designs were produced for each value of r_i . The outer translator radius was related to the inner radius by the mechanical requirements as set out in Equation 4.98. The fundamental algorithm which was used in the design is presented in the following section of pseudo-code.

```

Input:  rmin - The minimum value of ri
        rmax - The maximum value of ri
        rstep - The amount by which ri increments
        IC - Initial conditions for ksats and ksl
Output: Factors - Final values for ksats and ksl
        Performance - Final values for machine variables

```

```

For each ri between rmin and rmax in steps of rstep

```

```

  Factors <- IC
  step <- 1.0
  while step > 0 do
    Performance <- Function of Factors
    FactorsOld <- Factors
    Factors <- Function of Performance
    step <- Sum(Factors) - Sum(FactorsOld)
  end while
end for

```

For each value of r_i , a set of initial conditions were assumed for the slot leakage factors and the saturation factors, and used in the first calculations. The results of the first calculations

were fed back into the equations for these two sets of factors. The recalculated factors were then used again in the performance calculations. This was repeated until an accuracy of 10^{-6} was achieved, and the factors no longer varied with each successive iteration.

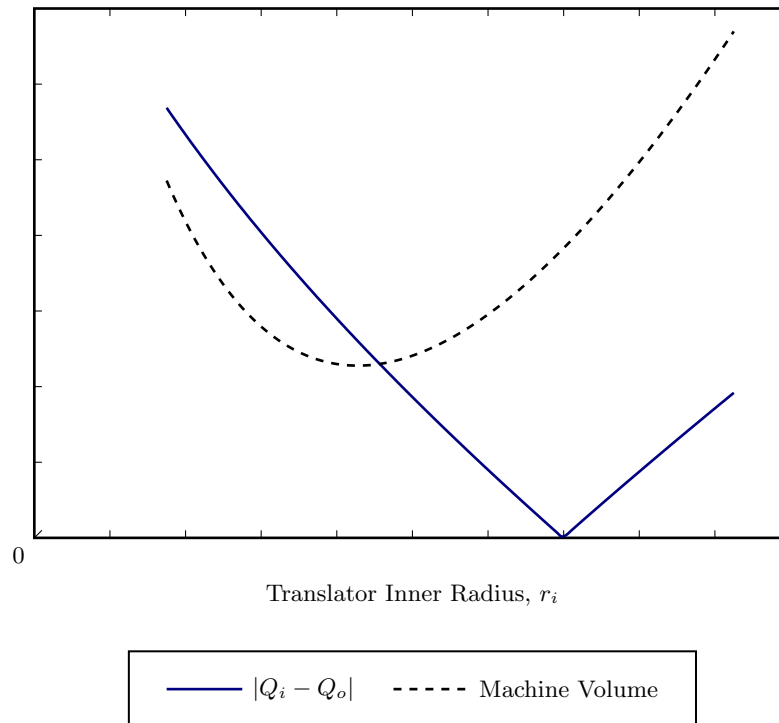


Figure 4.19: Characteristic Design Optimisation Curves for the Volume of the Machine and the Difference between the Stators' Specific Electrical Loadings.

Figure 4.19 shows a typical set of optimisation curves. Depending on the objective of the optimisation, one may choose the design which results in the lowest machine volume, or the design which maintains the best equality between the inner and outer stators' electrical loadings.

4.7 Conclusions

The mechanical actuation of a wave-energy converter is sinusoidal in nature. This sinusoidal actuation modulates the electrical output frequency and voltage, and changes the fundamental equations of the machine.

The electromechanical operation of wave energy devices is discussed in this chapter, and these effects carried through the subsequent derivation of the machine's performance equations.

The force generation of the machine is dealt with by way of the interaction of the stators' magnetic fields with an equivalent coil representing the permanent-magnets. This however yields an overly optimistic performance if considered alone because the parasitic magnetic losses in the system are neglected.

To account for this, a magnetic circuit model is developed which considers the magnetic flux path of the active flux in the circuit. Through an analytical model of the permeability of ferromagnetic materials, the non-linear characteristic of these materials is accounted for in the development of the magnetic reluctances.

These two sections complement one another in that the force calculation may be used to determine the magnetic flux, and the magnetic flux may be used to determine the parasitic losses which reduces the force capability of the machine.

Obviously this suggests that a suitable design algorithm must be followed to iteratively determine these values. A discussion on the objectives of a machine design is presented which includes such an algorithm. In this manner two possible objectives are identified.

Firstly, a designer may wish to ensure that the inner and outer stator sections exhibit equal electrical loadings. Secondly, the designer may wish to optimise the volume of the machine. These two are typically mutually exclusive. An optimised loading will result in a larger machine, while a smaller machine will result in a disparity between the electrical loadings.

Chapter 5

Validation of the Performance Calculations

***Introduction:** The mathematical description of the Double-Sided Tubular Permanent-Magnet Linear Synchronous Generator was developed in Chapter 4. The accuracy of this mathematical analysis is validated in this chapter. Initially, the validation takes the form of a simulated result using Finite-Element Analysis. Two machines were designed to match the performance of the AWS' pilot plant machine, each with a different optimisation objective. Thereafter, a physical implementation of a prototype machine is described. The machine specifications are presented. Finite-Element Analysis of this machine was also performed. The results from the analytical model, Finite-Element Analysis and physical measurements are presented. The results indicate a suitable accuracy in the analytical description of the machine developed in Chapter 4.*

5.1 Validating the Mathematical Model using Finite Element Analysis

The machines were simulated using two-dimensional Finite-Element Analysis (FEA). For each position in the stoke over four pole-pitches, the force was calculated using the package's built-in Maxwell Stress-Tensor Method. The simulation used FEMM's "US Steel Type 2-S 0.018 Inch Thickness" material as the electro-technical steel for machine[35].

The results were imported into Octave and Fourier analysis was performed on the force-distributions. The force-distributions were decomposed into the first nine harmonics. The harmonics beyond this order were negligible.

5.1.1 Analysis of the AWS Machine

The system parameters, which define the boundary conditions for the machine design, are presented in Table 5.1[48].

Table 5.1: System Parameters of the AWS

Parameter	Parameter Definition	Design Value
L_{stroke}	Stroke Length	7 m
\hat{F}	Peak Linear Force	1 MN
\hat{v}	Peak Linear Velocity	2.2 m/s

Given the peak velocity of 2.2 m/s and the peak force of 1 MN, and assuming a mechanical power factor of unity, one can see that the peak power production is 2.2 MW. The average power is 1.1 MW for the fundamental of the actuation. The machine which has been designed and incorporated into the AWS pilot plant is a double-sided flat permanent-magnet linear synchronous machine. The magnets move on the outside of a double-sided stator section. The specifications of the machine may be sourced from the literature[48]. The air-gap length was limited to 5 mm by the mechanical limitations of the bearing system. The available specifications of the machine are given in Table 5.2.

Table 5.2: Design Specifications of the AWS' Linear Synchronous Generator

Parameter	Parameter Definition	Design Value
L	Stator Length	5 m
L_t	Translator Length	8 m
τ_p	Pole-pitch	0.1 m
τ_m	Magnet-pitch	0.08 m
L_s	Stack Length	1 m
J	Conductor Current Density	4 A/mm ²
l_g	Air-gap length	5 mm
l_m	Magnet length	15 mm
k_Λ	Permeance Coefficient	2.4

From these specifications, a Finite-Element model was developed for the AWS' machine. The only unknown was the energy product of the permanent-magnets. However, to reduce the number of variables for the comparison between the two layouts, the same permanent-magnet material was simulated for both layouts, as well as the same operating temperature of 30°C. The final FEA model is shown in Figure 5.1.

The AWS device employs two of these double-sided flat machines. Therefore, the expected force production of one machine is 500 kN. The simulated force-distribution of a single device, and harmonic components thereof, are shown in Figures 5.2 and 5.3 respectively.

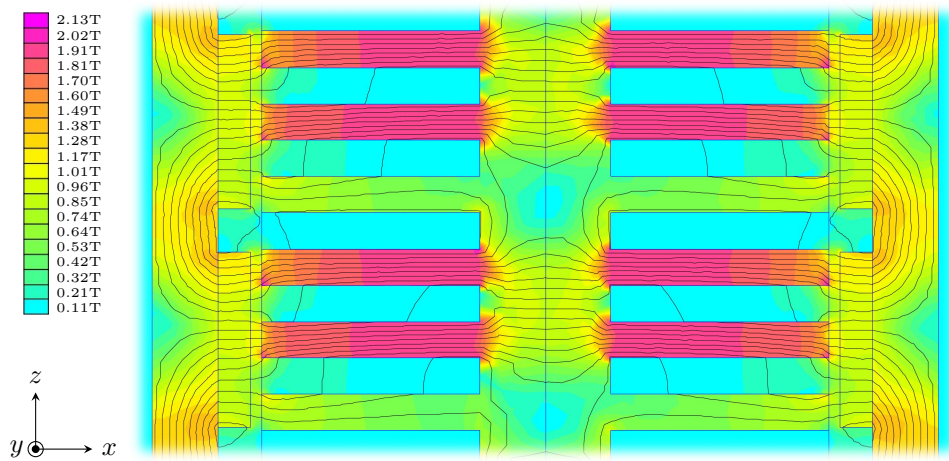


Figure 5.1: FEA Model of the AWS' Machine. All parameters are sourced from the literature regarding the machine's design. This is a planar simulation of a single machine. The AWS' device uses two such machines, each absorbing a total force of 500 kN.

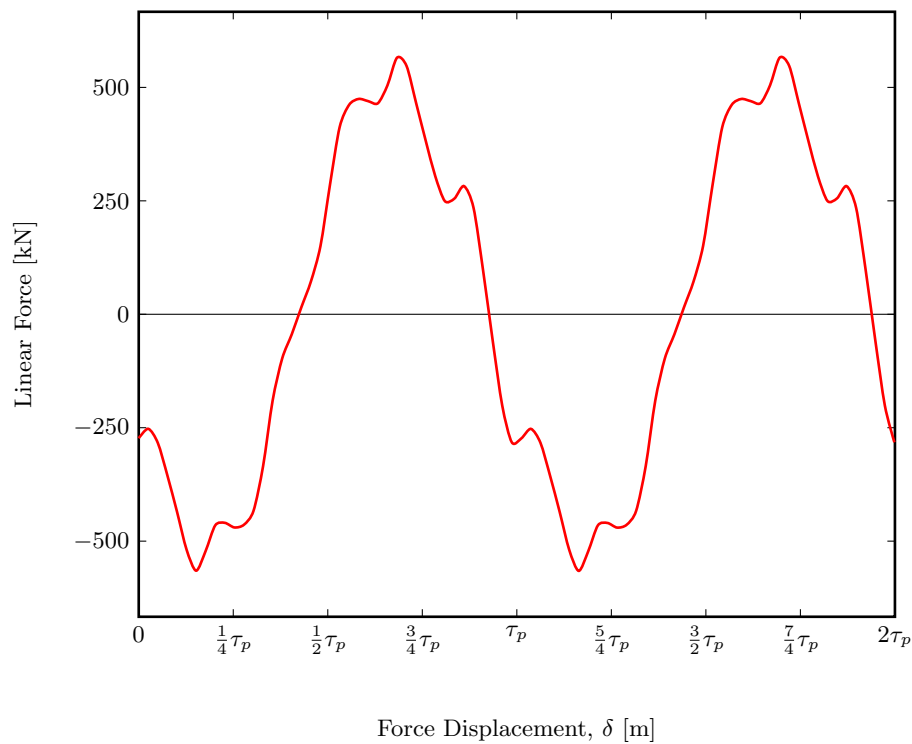


Figure 5.2: Simulated Force Distribution of the AWS' Machine (Peak of 5.65 kN).

The fundamental harmonic has a peak value of 517 kN. The second harmonic, which results from the reluctance variations at the end of the stators is 5.6% of this fundamental at 29 kN. The sixth harmonic, which represents the slot-cogging force is 12.4% of the fundamental at 64 kN. These are the results of a single machine; the total force produced by two machines is therefore a simply doubling of the results. The total synchronous force

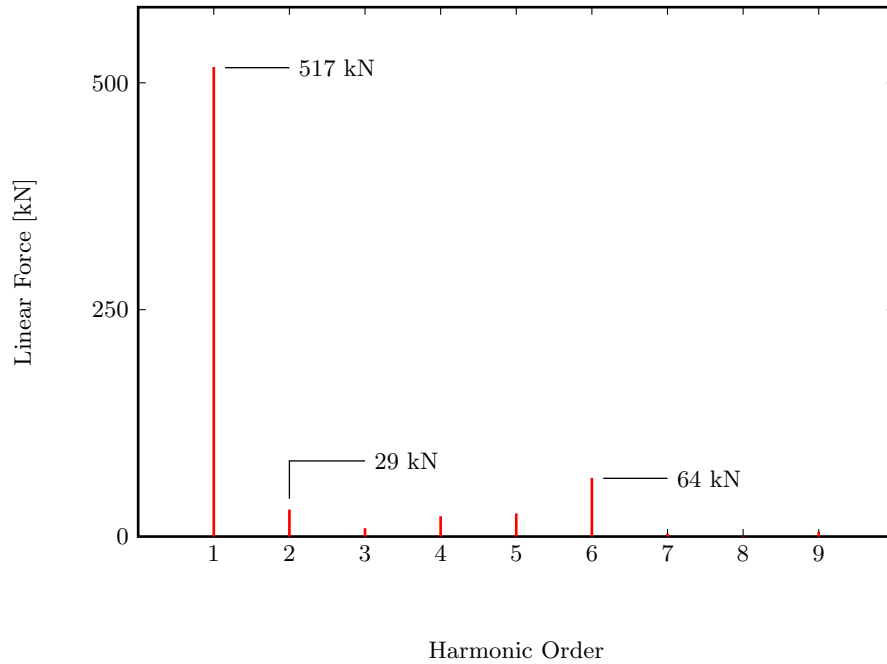


Figure 5.3: Harmonics Components of the Force Distribution of the AWS' Machine

capability of the AWS machine is 1.034 MN in this static force simulation. By including the power factors and efficiency, it is conceivable for this value to reduce to the desired 1 MN during oscillatory wave actuation. The simulations confirm that the design of the AWS machine will achieve the required 1 MN, and confirm that the analytical techniques which are employed in the FEA modelling studies are appropriate for the forgoing analysis.

5.1.2 Analysis of the Double-Sided Tubular Machine

To allow for a more realistic evaluation of the double-sided tubular machine when compared to the AWS' machine, the boundary conditions were chosen to match that of the AWS' machine from Tables 5.1 and 5.2. Two designs were produced, based on the two optimisation criteria which are discussed in Section 4.6. The first design achieves equality between the inner and outer specific electrical loadings. The second design was produced so as to minimise the machine's volume. The parameters of these two exemplary machines are given in Table 5.3.

The machines were simulated using 2D axially-symmetric Finite-Element Analysis. A section of each of the machines is shown in a flux-density plot in Figure 5.4. Figure 5.4, in conjunction with Table 5.3, illustrates the key difference between the two design objectives. The radii of the first design are larger than those of the second, but the stators' electrical loadings are equal. This is evident from the equal slot dimensions in Figure 5.4 a). Conversely, the higher electrical loading of the outer stator in the second design is evident

Table 5.3: Exemplary Full-Scale Machine Specifications

Parameter	Parameter Definition	Design 1	Design 2
L	Stator Length	5 m	5 m
L_t	Translator Length	8 m	8 m
τ_p	Pole-pitch	0.1 m	0.1 m
τ_m	Magnet-pitch	0.08 m	0.08 m
k_w	Winding Factor	1.0	1.0
q	Slots/pole/phase	1	1
r_o	Translator Outer radius	0.306 m	0.281 m
r_i	Translator Inner radius	0.283 m	0.256 m
l_m	Magnet length	15 mm	15 mm
l_g	Air-gap length	5 mm	5 mm
l_{si}	Inner Stator Length	0.082 m	0.074 m
l_{so}	Outer Stator Length	0.068 m	0.084 m
l_{ci}	Inner Core Length	0.032 m	0.032 m
l_{co}	Outer Core Length	0.019 m	0.017 m
Q_i	Inner Specific Electrical Loading	58 316 A/m	48 770 A/m
Q_o	Outer Specific Electrical Loading	58 101 A/m	78 053 A/m
J	Conductor Current Density	4 A/mm ²	4 A/mm ²
\hat{B}_c	Peak Core Flux Density	1.5 T	1.5 T
\hat{B}_t	Peak Teeth Flux Density	1.8 T	1.8 T
T_{op}	Magnet Operating Temperature	30°C	30°C

from the larger outer slot area in Figure 5.4 b). The resulting force-distributions for the two designs are shown in Figure 5.5. The resulting harmonic components of these force-distributions are shown in Figure 5.6 for the first nine harmonics.

One can readily determine the most significant harmonics in the force-distributions. The fundamental components are 997 kN and 988 kN respectively, signifying the designed synchronous force. The errors between these results and the required design force of 1 MN are -0.84% and -0.19% respectively.

The second harmonics are reluctance forces of 38 kN and 47 kN respectively which are produced by the action of the magnets passing by the ends of the stator sections. Given that this machine is much longer than it is wide, the contributions here are only 3.8% and 4.7% of the fundamentals respectively, and are negligible. A shorter machine would exhibit significantly higher contributions from the second harmonic.

Finally, the sixth harmonic forces are present because of the slot-cogging. These values

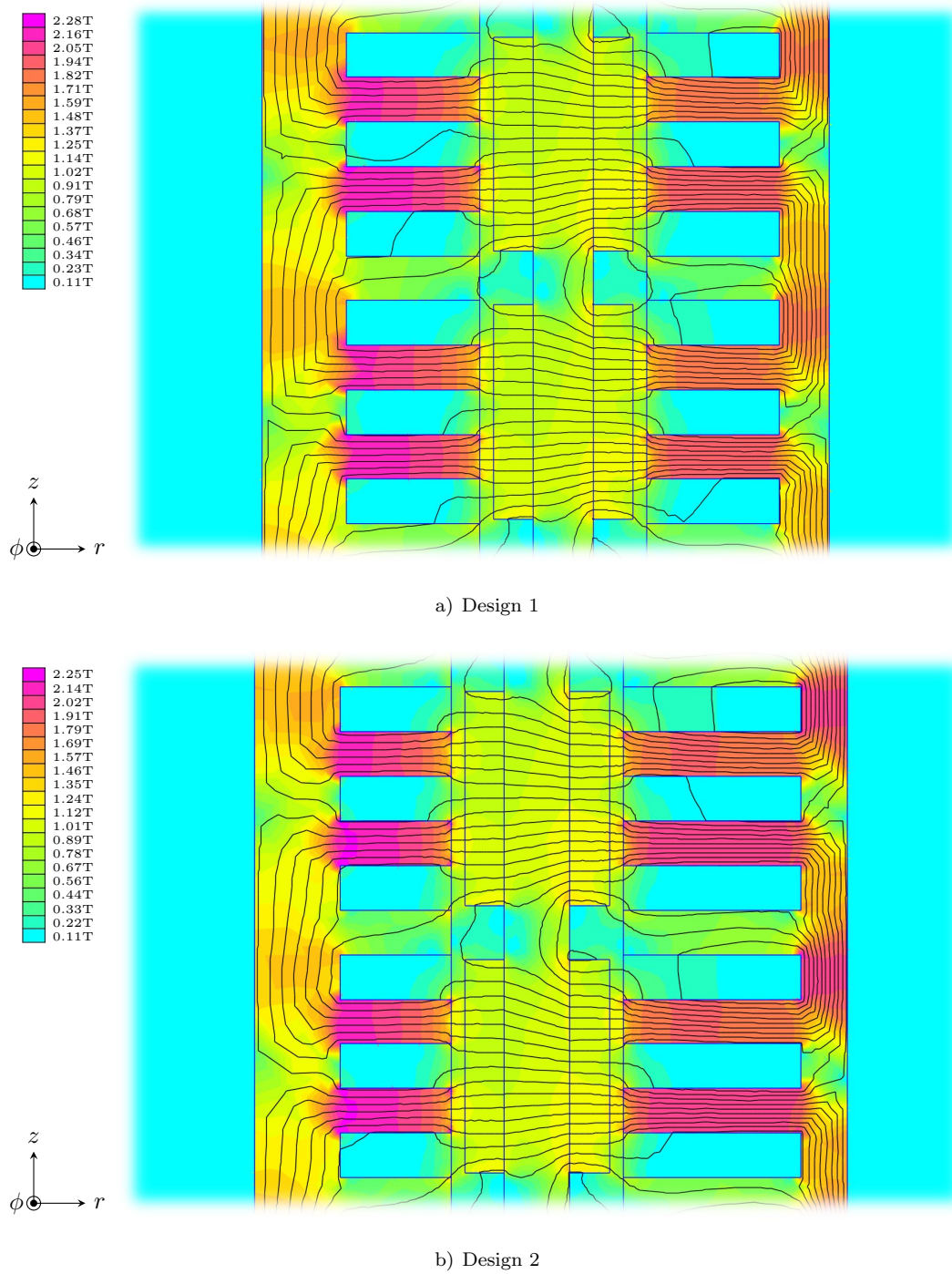


Figure 5.4: FEA Models of the Full-scale Double-Sided Tubular Machine Designs.

are 111 kN and 104 kN respectively, representing 11.1% and 10.4% of the fundamentals respectively. One can see that these are quite significant. The sixth harmonic results from having open slots. Different slot designs would reduce this component significantly and should be considered for commercial designs. It must be noted however, that Carter's coefficient, k_c , will change according to the slot design.



Figure 5.5: Full-scale Designs' Force Distributions (Plot Peaks of 1.089 MN and 1.090 MN respectively).

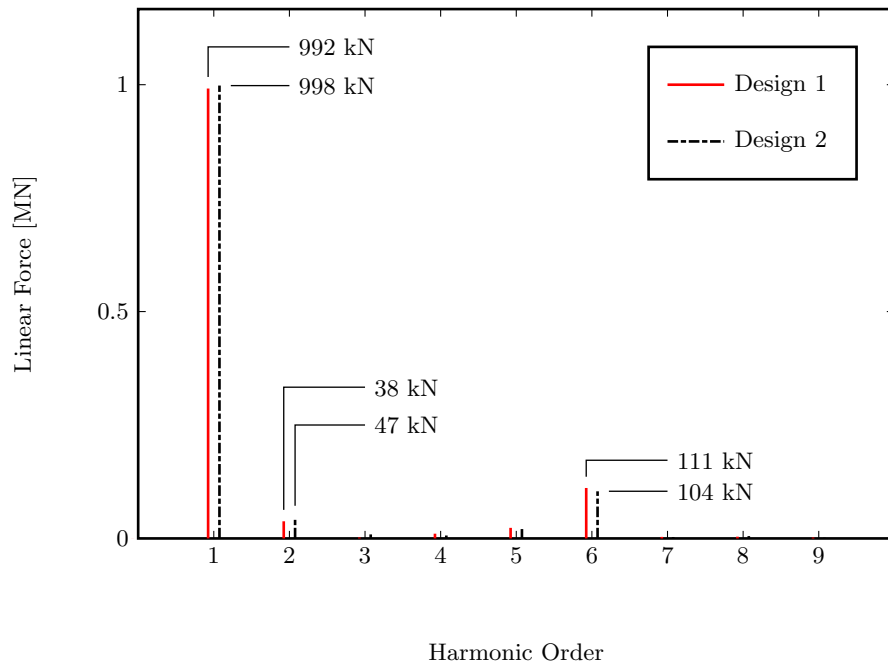


Figure 5.6: Full-scale Designs' Harmonic Force Components.

5.2 Validating the Mathematical Model through Prototype Construction

In order to validate the analytical description of the machine more comprehensively, a representative machine was designed, constructed and tested. The machine was not a proportionally scaled version of the full-scale machines proposed in Section 5.1. Instead, the design had its own mechanical specifications. Few of the original dimensions were maintained. This was advantageous because the analytical model could be tested on vastly different design requirements. The system was designed to test the force capability of the machine; dynamic testing of the machine was beyond the scope of this research.

The machine was designed using the mathematical model and methodology developed in this research. The design was then modified to suit the available materials, budget and mechanical constraints. The result was a sub-optimal design, but one suitable for the purposes of this research. The final machine specifications are given in Table 5.4. A photograph of the machine is presented in Figure 5.7 and a section of the FEA model is shown in Figure 5.8.

The machine was tested by passing DC current through the stator windings and pulling the translator upwards through the machine. The DC resistance of the outer stator was roughly two orders of magnitude less than the DC resistance of the inner stator. Both were driven from the same DC generator. To split the current such that the current density was equal in both stators, a set of rheostats was connected in series to the outer stator. The DC voltage was set to achieve the 5 A/mm^2 in the inner stator; the rheostats were set to achieve the same in the outer stator. The rheostat arrangement is shown in Figure 5.9.

A load-cell based scale was attached between the translator's lifting eye and the crane which was used to pull the translator upwards. A simple translator measurement was achieved by attaching a pointer to the lifting eye, which passed by metre-rules which were attached to the top of the support structure. In this way, the distance measurement and scale measurement were recorded simultaneously on a video-camera. This setup is shown in Figure 5.10.

The video footage was analysed and the scale readings recorded with their respective translator positions. The testing apparatus was not ideal, but served its purpose very well. By using Fourier analysis of the resulting force-distribution, the noise in the signal, which was attributable to the measurement technique, was filtered out.

The machine was tested in both the unexcited state and the excited state. In the unexcited state, no current was passed through the windings. In the excited state, four relevant current densities were developed in the stator windings. The stators were excited with 25%, 50%, 75% and 100% of the full-load current for the excited trials. This combination of the excited and unexcited tests allowed for the magnetic, electromagnetic and mechanical



Figure 5.7: Photograph of the Prototype Machine, Constructed at the Machines Research Laboratory, University of the Witwatersrand.

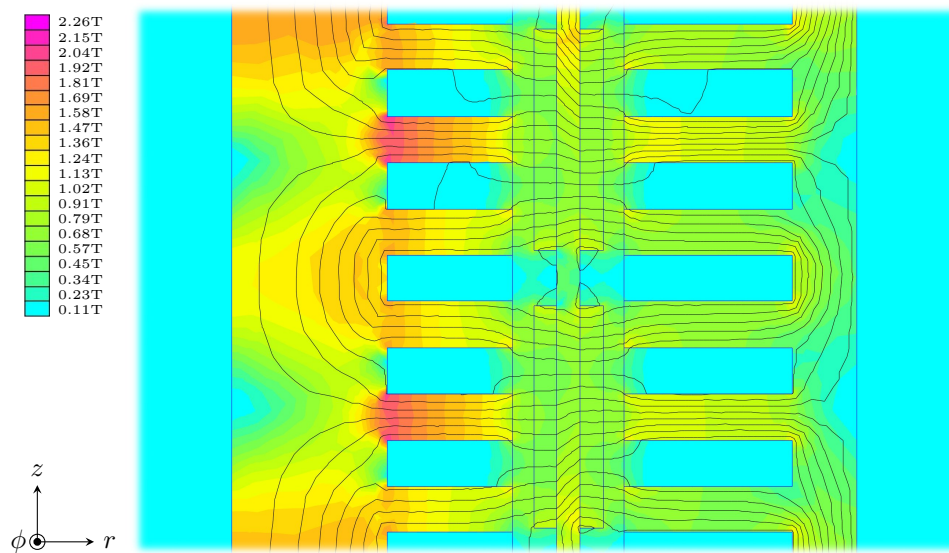


Figure 5.8: FEA Model of the Prototype Machine.

Table 5.4: Specifications of the Prototype Machine

Parameter	Parameter Definition	Design Value
L	Stator Length	0.36 m
L_t	Translator Length	1.00 m
L_m	Magnet Array Length	0.60 m
τ_p	Pole-pitch	0.06 m
τ_m	Magnet-pitch	0.048 m
k_w	Winding Factor	1.0
q	Slots/pole/phase	1
r_o	Translator Outer radius	0.078 m
r_i	Translator Inner radius	0.073 m
l_m	Magnet length	5.0 mm
l_g	Air-gap length	4.5 mm
l_{si}	Inner Stator Length	0.0605 m
l_{so}	Outer Stator Length	0.0503 m
l_{ci}	Inner Core Length	0.0335 m
l_{co}	Outer Core Length	0.0140 m
Q_i	Inner Specific Electrical Loading	8 400 A/m
Q_o	Outer Specific Electrical Loading	14 000 A/m
J	Conductor Current Density	5 A/mm ²
\hat{B}_c	Peak Core Flux Density	1.5 T
\hat{B}_t	Peak Teeth Flux Density	1.8 T
T_{op}	Magnet Operating Temperature	25°C

components of the force-distribution to be isolated from each other.

For each current density, a positive and negative DC polarity test was performed. This was done because the test apparatus could only measure the downward force exerted by the stator on the translator. When the translator slipped a pole, the force exerted on it was vertically upward, which could not be measured. By reversing the polarity, the force-distribution shifted by 180°, thus the ‘negative’ half-cycle of the force-distribution could be measured.

Table 5.5 lists the results of the analysis for the fundamental component at the four stator excitation levels. The measured and simulated values were derived through Fourier analysis of the force-distributions, and the calculated values were derived using the performance equations set out in Chapter 4.

The measured values were chosen as the base case from which the relative errors of the



Figure 5.9: The rheostat arrangement was used to produce full-load current densities of $5\text{A}/\text{mm}^2$ in each of the stators from a single DC generator supply.



Figure 5.10: Static Force Testing Apparatus. The load-cell based scale measured the force exerted on the translator by the stator field, which opposed the upward force that the crane exerted on the translator.

simulated and calculated values were established. Positive and negative percentage error values indicate an over- and under-estimation of the force respectively.

Table 5.5: Prototype Machine Performance - Comparison between the Simulated, Calculated and Measured Values at the Four Levels of Stator Excitation.

Excitation:	25%	50%	75%	100%
Measured	650.4 N	1474.0 N	1977.2 N	2619.6 N
Simulated	653.5 N	1469.4 N	1988.5 N	2593.9 N
	0.49%	-0.31%	0.58%	-0.98%
Calculated	657.8 N	1492.4 N	2007.7 N	2639.5 N
	1.14%	1.25%	1.54%	0.75%

It is important to note that the structure of the teeth sections of the stators included steel laminated in the r - ϕ plane. As such, the slot leakage was significantly reduced. In a mechanically excited system this would not be appropriate because of the associated eddy-current losses. However, this was sufficient for the purposes of the static force testing.

5.3 Conclusions

The Finite-Element Analysis of the AWS' pilot plant machine confirms that the machine could produce the desired 500 kN. This portion of the study also confirmed the validity of the techniques used in the analysis of the Finite-Element Analysis results.

Two double-sided tubular machines were designed, and simulated using Finite-Element Analysis. They were designed to match the 1 MN requirement of the AWS platform. The first design was optimised to achieve equal specific electrical loadings in the stators. The second design was optimised to minimise the volume of the machine. The resulting designs produce forces of 992 kN and 998 kN respectively, which represent errors of -0.84% and -0.19% respectively, relative to the 1 MN design requirement.

The design, construction, simulation and testing of a prototype machine provided further validation of the analytical model of the machine, as developed in Chapter 4. At full stator excitation, the measured fundamental force component was 2619.6 N. The simulations and calculations indicated forces of 2593.9 N and 2639.5 N respectively, which deviate from the measured value by -0.98% and 0.75% respectively. For other values of stator excitation, the deviation of the calculated force capacity ranged between 1.14% and 1.54% which are acceptable errors.

The primary reason for the inaccuracy may be attributed to the difficulty in accurately modelling the magnetic circuit, most notably the quantification of the slot leakage and the magnetic saturation.

The contribution of the slot harmonics to the final force-distribution is significant. This may be reduced by using semi-closed slot designs.

Chapter 6

Conclusions

Force density and flux utilisation are key characteristics of double-sided flat and single-sided tubular layouts respectively. The hypothesis of this research was that through combining the two layouts into a double-sided tubular machine, a significant increase in these two metrics may be achieved, beyond the possibilities of each layout in its own right.

In considering the value of such a layout when compared to a double-sided flat layout, we may wish to compare the footprint, machine volume and permanent-magnet volume of this versus the AWS' machine. Table 6.1 presents a comparison between the double-sided flat layout, which was employed in the AWS System, and the two double-sided tubular machines which were designed and simulated in Chapter 5.

Table 6.1: Comparison between the Double-Sided Flat Machine of the AWS and the Double-Sided Tubular Machine Designs of Chapter 5

Metric	AWS Machine	Design 1	Design 2
Footprint	0.720 m ²	0.487 m ²	0.465 m ²
Machine Volume	3.60 m ³	1.92 m ³	1.90 m ³
PM Volume per Pole	4.8 dm ³	4.4 dm ³	4.0 dm ³

The objective of the first double-sided tubular machine design was to maintain equality between the inner and outer stators' specific electrical loadings. The objective of the second design was to minimise the material volume of the machine. The latter results in a smaller volume than the former at the expense of the equality between the stators' electrical loadings. This is not problematic except that the relative contributions of each stator to the total force production is not equal.

Regardless of the design objective, it is evident from Table 6.1 that the double-sided tubular machine layout exhibits a significantly higher force density and material utilisation

than the flat alternative.

In the case of the first design, with equal specific electrical loadings of the two stators, the footprint of the double-sided machine is 32% smaller than the AWS' machine. This is accompanied by a 47% smaller volume with only 92% of the permanent-magnet material compared to the AWS' machine. The second design achieves better results with a 35% smaller footprint, 47% less volume and 83% of the permanent-magnet material.

By all metrics it is evident that the research hypothesis is verified. The research has also provided an analytical model for the design and analysis of such machines. The accuracy of this model has been proved to within 1.54% for the prototype machine, increasing in accuracy to a 0.84% error for the full-scale machines. The accuracy of the analytical model may be attributed to the inclusion of magnetic saturation and leakage in the analysis.

6.1 Guidelines for Future Investigations

Although the present research has proved successful in its objectives, the new layout warrants further investigation. Further research should consider the mechanical and the magnetic designs. Both of these are important in their own right and must be optimised without compromising the electromagnetic performance of the machine.

6.1.1 Mechanical Considerations

The bearing mechanics of a tubular machine are not trivial. In the prototype machine, the short stator length allowed for support bearings to be placed at the top and bottom of the stators. On longer stators, this would not be an effective bearing solution. Alternative designs which may be effective include:

- To integrate the bearings into the translator system. The author proposes that a pole-pair be skipped every so often to accommodate a bearing assembly on-board the translator. This would have an additional advantage of preventing eddy-currents from being induced in the bearings as the magnets move past the stator sections.
- To integrate the bearings into the stator assembly by creating vertically sectioned stators. In this fashion, the total five metre stator section may comprise five individual one metre sections, spaced such that bearings assemblies may be placed in-between them, one pole-pair apart. The primary disadvantage of this system is that the second harmonic reluctance force would increase according to the number of stator sections.

The interior stator is surrounded by the translator. Thermal modelling is required to establish what cooling mechanisms may be employed to cool the inner stator, or to what extent the dimensions of the machine must change to accommodate adequate cooling of the

inner stator. The translator may lend itself to use as an air-piston in a forced-air cooling application. This is because the reciprocating motion may be used, with appropriate air-valves in place, to push air past the inner stator or through appropriately designed cooling ducts. A comprehensive thermal model will contribute to the understanding of the thermal limits of the double-sided tubular machine.

6.1.2 Magnetic Considerations

The application of wave-energy conversion demands a low Total Force Ripple. However, linear machines by nature will exhibit a relatively large second harmonic arising from the end-effects of the stator sections. A means of mitigating these effects is required.

One recommendation is to design tapered stator ends. This will provide a more gradual change in reluctance, which will lead to a lower second harmonic.

The migration from static force testing to dynamic actuation will introduce the normal machine losses associated with eddy-currents and hysteresis. The design of the magnetic material to be used in the cores is of importance.

Although laminations may be used to the same end as in rotary machines, these will need to be tapered. This introduces extensive tooling costs and is not suitable for small machines. Large machine designs may warrant the additional expense.

However, a significant advantage may be gained through the use of Soft Magnetic Composites (SMC). Although the lamination effect will be lost through their use, and an associated reduction in machine performance is to be expected, the material also makes possible:

- The near elimination of eddy-current losses,
- The simple development of semi-closed slots which would aid in reducing the sixth harmonic component of the electromagnetic force, and
- A simple assembly procedure as the SMC teeth sections may be produced such that the coils and teeth may be stacked with relative ease and without hydraulic stack compression.

6.2 Contribution of the Present Research to the Scientific Community

The primary contribution of this research has been to identify a fourth possible linear machine layout to the field. This adds to the tubular, single-sided flat and double-sided flat layouts which are documented in the literature.

The present research has focussed on the use of surface mounted permanent-magnet synchronous machines. However, the layout may be used for other magnetic designs including transverse-flux, buried permanent-magnet, and linear induction machines, where applicable.

The presented analytical model of this machine may be used for design or analysis purposes. The primary design considerations and objectives have been documented which may be applied to different applications.

These tools, presented here, may contribute to the understanding and development of direct-drive linear generators for ocean wave-energy conversion systems.

References

- [1] AWS Ocean Energy Ltd. Archimedes WaveswingTM, 2004. URL <http://www.awsoccean.com>. Last Accessed: 19 November 2009.
- [2] International Bible Society. *Life Application Study Bible, New International Version*. Tyndale House Publishers, Inc., 351 Executive Drive, Carol Stream, IL 60188, United States of America, 1997. ISBN 0-8423-4892-1.
- [3] S. Fred Singer, editor. *Energy*. Readings from Scientific America. W.H. Freeman and Company, 660 Market Street, San Francisco, California, 94104, United States of America, 1976. ISBN 0-7167-1082-X.
- [4] Raymond A. Serway and Robert J. Beichner. *Physics for Scientists and Engineers with Modern Physics*. Harcourt College Publishers, 6277 Sea Harbor Drive, Orlando, Florida, 32887-6777, United States of America, fifth edition, 2000. ISBN 0-03-022657-0.
- [5] Chris Hails, editor. *Living Planet Report 2008*. World Wildlife Fund International, Avenue du Mont-Blanc, CH-1196 Gland, Switzerland, 2008. ISBN 978-2-88085-292-4.
- [6] Jean-Romain Frisch. *Future Stresses For Energy Resources. Energy Abundance: Myth or Reality?* Graham & Trotman Limited, Sterling House, 66 Wilton Road, London, SW1 1DE, United Kingdom, 1986. ISBN 0-86010-824-40.
- [7] James P. Hartnett. *Alternative Energy Sources*. Academic Press, Inc., 24-28 Oval Road, London, NW1 7DX, United Kingdom, 1976. ISBN 0-12-328550-X, 0-89116-017-5.
- [8] World Energy Council. *Survey of Energy Resources*. Elsevier Ltd., The Boulevard, Langford Lane, Kidlington, Oxford, OX5 1GB, United Kingdom, twentieth edition, 2004. ISBN 0-08-044410-5.
- [9] Kenneth S. Deffeyes. *Hubbert's Peak: The Impending World Oil Shortage*. Princeton University Press, 41 William Street, Princeton, New Jersey, 08540, United States of America, 2003. ISBN 0-691-11625-3.

- [10] Bjørn Lomborg. *The skeptical environmentalist: Measuring the Real State of the World*. Cambridge University Press, The Edinburgh Building, Cambridge, CB2 2RU, United Kingdom, 2001. ISBN 0-521-01068-7.
- [11] John Brooke. *Wave Energy Conversion*, volume 6 of *Elsevier Ocean Engineering Book Series*. Elsevier Science Ltd., The Boulevard, Langford Lane, Kidlington, Oxford, OX5 1GB, United Kingdom, 2003. ISBN 008-044212-9.
- [12] Sargent & Lundy LLC Consulting Group. Executive Summary: Assessment of parabolic trough and power tower solar technology cost and performance forecasts. Technical Report NREL/SR-550-34440, National Renewable Energy Laboratory, 1617 Cole Boulevard, Golden, Colorado, 80401-3393, United States of America, October 2003. Prepared under Subcontract No. LAA-2-32458-01.
- [13] Tom Denniss, Tom Thorpe, Tim Finnigan, and Tom Engelsman. The use of normalized power output curves for wave energy applications, February 2005. URL <http://energetech.com.au/attachments/NormalizedPowerOutput.pdf>. Last Accessed: 27 June 2009.
- [14] George Hagerman, Roger Bedard, and Mirko Previsic. E2I EPRI survey and characterization of potential offshore wave energy sites in washington. Technical Report E2I EPRI WP WA 003, Electric Power Research Institute, Inc., May 2004. URL http://oceanenergy.epri.com/attachments/wave/reports/003_Washington_Site_Report.pdf. Last Accessed: 27 June 2009.
- [15] Renewable Energy Policy Network for the 21st Century. Renewables - global status report: Update 2009, May 2009. URL <http://www.ren21.net>. Last Accessed: 06 May 2010.
- [16] Cristina L. Archer and Mark Z. Jacobson. Evaluation of global wind power. In *Journal of Geophysical Research - Atmospheres*, volume 110, D12110, doi:10.1029/2004JD005462. American Geophysical Union, 2000 Florida Avenue N.W., Washington, DC 20009-1277, United States of America, June 2005. ISSN 0148-0227.
- [17] Wikipedia, The Free Encyclopedia. Capacity factor, February 2006. URL http://en.wikipedia.org/wiki/Capacity_factor. Last Accessed: 19 November 2009.
- [18] Carnegie Wave Energy Limited. Wave energy as a base load power resource, 2010. URL <http://www.carnegiewave.com>. Last Accessed: 06 May 2010.
- [19] Tom Thorpe. A brief review of wave energy. Technical Report R120, The UK Department of Trade and Industry, B 154, Harwell, Didcot, Oxfordshire, OX11 0RA, United Kingdom, May 1999.

- [20] Albert Einstein and Leopold Infeld. *The Evolution of Physics*. Simon & Schuster, Inc., Rockefeller Center, 1230 Avenue of the Americas, New York, NY, 10020, United States of America, 1966. ISBN 0-671-20156-5.
- [21] William S. von Arx. *An Introduction to Physical Oceanography*. Addison-Wesley Publishing Co. Inc., 1 Jacob Way, Reading, MA 01867-3932, United States of America, 1962. ISBN 978-0-201-08174-9, 0-201-08174-1.
- [22] Catherine Soanes and Angus Stevenson, editors. *Concise Oxford English Dictionary*. Oxford University Press, Great Clarendon Street, Oxford, OX2 6DP, United Kingdom, eleventh revised edition, 2008. ISBN 978-0-19-954841-5.
- [23] Alain Clément et al. Wave energy in europe: Current status and perspectives. In L. Kazmerski, editor, *Renewable and Sustainable Energy Reviews*, volume 6, Issue. 5, pages 405–431. Elsevier Ltd., The Boulevard, Langford Lane, Kidlington, Oxford, OX5 1GB, United Kingdom, October 2002. ISSN 1364-0321.
- [24] George Hagerman. Wave power. In Attilio Bisio and Sharon Boots, editors, *Encyclopedia of Energy Technology and the Environment*, Wiley Encyclopedia Series in Environmental Science, pages 2859–2907. John Wiley & Sons, Inc., The Atrium, Southern Gate, Chichester, West Sussex, PO19 8SQ, United Kingdom, May 1995. ISBN 978-0-471-54458-6.
- [25] M. A. Mueller. Electrical generators for direct drive wave energy converters. In *Generation, Transmission and Distribution, IEE Proceedings*, volume 149, Issue. 4, pages 446–456. The Institution of Engineering and Technology, Michael Faraday House, Six Hills Way, Stevenage, SG1 2AY, United Kingdom, July 2002. ISSN: 1350-2360.
- [26] Jacek F. Gieras and Zbigniew J. Piech. *Linear Synchronous Motors - Transportation and Automation Systems*. CRC Press LLC, 2000 N.W Corporate Boulevard, Boca Raton, Florida, 33431, United States of America, 2000. ISBN 0-8493-1859-9.
- [27] H. Polinder, B.C. Mecrow, A.G. Jack, P. Dickinson, and M.A. Mueller. Linear generators for direct-drive wave energy conversion. In *International Electric Machines and Drives Conference IEMDC2003*, pages 798–804. Institute of Electrical and Electronics Engineers, Inc., 445 Hoes Lane, Piscataway, NJ 08854-4141, United States of America, 2003. ISBN 978-0-780-37818-6, 0-78037-818-0.
- [28] N. Baker, M. Mueller, and E. Spooner. Permanent magnet air-cored tubular linear generator for marine energy converters. In *Proceedings of the 2nd IEE International Conference on Power Electronics, Machines and Drives*, volume 2, pages 862–867. Institution of Electrical Engineers, Michael Faraday House, Stevenage, Herts, SG1 2AY, United Kingdom, April 2004. ISBN 978-0-86341-383-4, 0-86341-383-8. ISSN: 0537-9989.

- [29] A. W. van Zyl and C. F. Landy. Optimisation of the secondary design for a modified tubular linear synchronous motor. In *Proceedings on the 4th International Symposium on Linear Drives for Industry Applications, LDIA2003*, pages 375–378. University of Sheffield, Western Bank, Sheffield S10 2TN, United Kingdom, September 2003. ISBN 978-0-953-52281-1, 0-9535-2281-4.
- [30] Jacek F. Gieras and Mitchell Wing. *Permanent Magnet Motor Technology*. Electrical and Computer Engineering. Marcel Dekker, Inc., 270 Madison Avenue, New York, NY 10016, United States of America, 2002. ISBN 0-8247-0739-7.
- [31] Peter Campbell. *Permanent Magnet Materials and their Applications*. Cambridge University Press, The Pitt Building, Trumpington Street, Cambridge, CB2 1RP, United Kingdom, 1994. ISBN 0-521-24996-1.
- [32] Richard M. Bozorth. *Ferromagnetism*. IEEE Press, 445 Hoes Lane, PO BOX 1331, Piscataway, NJ 08855-1331, United States of America, 1993. ISBN 0-7803-1032-2.
- [33] J.R. Hendershot, Jr. and T.J.E Miller. *Design of Brushless Permanent-Magnet Motors*. Monographs in Electrical and Electronic Engineering. Oxford University Press, Walton Street, Oxford, OX2 6DP, United Kingdom, 1994. ISBN 0-19-859389-9.
- [34] Charles L. Phillips and John M. Parr. *Signals, Systems, and Transforms*. Prentice Hall, Inc., Upper Saddle River, New Jersey, 07458, United States of America, second edition, 1999. ISBN 0-13-095322-9.
- [35] David C. Meeker. *Finite Element Method Magnetics*, May 2008. URL <http://www.femm.info>. Version 4.2.
- [36] M. G. Say. *Alternating Current Machines*. Pitman Publishing Limited, 128 Long Acre, London, WC2E 9AN, United Kingdom, fifth edition, 1984. ISBN 0-273-01968-6.
- [37] A.E. Fitzgerald, Charles Kingsley, Jr, and Stephen D. Umans. *Electric Machinery*. Electrical Engineering Series. The McGraw-Hill Companies, Inc., 1221 Avenue of the Americas, New York, NY 10020, United States of America, fourth SI metric edition, 1988. ISBN 0-07-Y66279-7.
- [38] P.R.M. Brooking and M.A. Mueller. Power conditioning of the output from a linear vernier hybrid permanent magnet generator for use in direct drive wave energy converters. In *Generation, Transmission and Distribution, IEE Proceedings*, volume 152, Issue. 5, pages 673–681. The Institution of Engineering and Technology, Michael Faraday House, Six Hills Way, Stevenage, SG1 2AY, United Kingdom, September 2005. ISSN: 1350-2360.

- [39] Dr. Duane Hanselman. *Brushless Permanent Magnet Motor Design*. The Writer's Collective, Cranston, Rhode Island, second edition, 2003. ISBN 1-932133-63-1.
- [40] Harit Majmudar. *Electromechanical Energy Converters*. Allyn and Bacon Series in Electrical Engineering. Allyn and Bacon, Inc., 470 Atlantic Avenue, Boston, MA 02110, United States of America, 1969. Library of Congress Catalog Card Number: 65-17867.
- [41] Helmut Mosebach. Direct two-dimensional analytical thrust calculation of permanent magnet excited linear synchronous machines. In *Proceedings on the 2nd International Symposium on Linear Drives for Industry Applications, LDIA1998*, pages 396–399. Institute of Electrical Engineers of Japan, 6-2 Goban-cho, Chiyoda-ku, Tokyo 102-0076, Japan, April 1998.
- [42] Jiabin Wang, Geraint W. Jewell, and David Howe. A general framework for the analysis and design of tubular linear permanent magnet machines. In *IEEE Transactions on Magnetics*, volume 35, no. 3, pages 1986–2000. Institute of Electrical and Electronics Engineers, Inc., 445 Hoes Lane, Piscataway, NJ 08854-4141, United States of America, May 1999. ISSN: 0018-9464.
- [43] Umran S. Inan and Aziz A. Inan. *Engineering Electromagnetics*. Addison Wesley Longman, Inc., 2725 Sand Hill Road, Menlo Park, California, 94025, United States of America, 1999. ISBN 0-201-47473-5.
- [44] George B. Arfken and Hans J. Weber. *Mathematical Methods for Physicists*. Elsevier Academic Press, 84 Theobald's Road, London WC1X 8RR, United Kingdom, sixth edition, 2005. ISBN 978-0-12-088584-8, 0-12-088584-0.
- [45] J. Wang, G.W. Jewell, and D. Howe. Analysis and design optimisation of slotless tubular permanent magnet linear motors. In *Proceedings on the 3rd International Symposium on Linear Drives for Industry Applications, LDIA2001*, pages 84–89. Institute of Electrical Engineers of Japan, 6-2 Goban-cho, Chiyoda-ku, Tokyo 102-0076, Japan, October 2001.
- [46] F. J. Camm, editor. *Newnes Engineer's Reference Book*. George Newnes Limited, 15-17 Long Acre, London, WC2, United Kingdom, ninth edition, 1960.
- [47] Wolfram Research, Inc. *Mathematica*. Wolfram Research, Inc., 100 Trade Center Drive, Champaign, IL 61820-7237, United States of America, seventh edition, 2008.
- [48] Henk Polinder, Michiel E. C. Damen, and Fred Gardner. Linear PM generator system for wave energy conversion in the AWS. In *IEEE Transactions on Energy Conversion*, volume 19, no. 3, pages 583–589. Institute of Electrical and Electronics Engineers, Inc., 445 Hoes Lane, Piscataway, NJ 08854-4141, United States of America, September 2004. ISSN: 0885-8969.

- [49] John W. Eaton, David Bateman, and Søren Hauberg. *GNU Octave Manual*. Network Theory Limited, United Kingdom, third edition, 2008. ISBN 978-0-9546120-6-1, 0-9546120-6-X.

Appendices

Appendix A

Design, Simulation and Analysis Scripts

***Introduction:** Three programming languages were used in the design, simulation and analysis of the linear generators. Mathematica[®] was used in the design and the calculation of the performance of the double-sided tubular machines[47]. This mathematical engine has an advanced symbolic solver which reliably solves systems of simultaneous equations.*

The Finite-Element Analysis of the machines was performed using FEMM which has an embedded Lua console[35]. Thus the machine simulation and data extraction was performed using the Lua language.

Finally, the analysis of the resulting simulation data, as well as the analysis of the measured prototype performance was performed using the Octave numerical mathematics language[49].

The following sections list the source code for the various tasks which were performed throughout the research. Section A.1 provides the Mathematica scripts, Section A.2 the Lua scripts and Section A.3 the Octave analysis scripts. Section A.4 provides some utilities, written in Octave, which were used by the Octave analysis scripts.

A.1 Mathematica Design and Performance Calculation Scripts

Script A.1: Machine Performance Calculation Script

```

1  (*%%%%%%%%%%%%%%%%%%%%%%%%%%%%%%%%%%%%%%%%%%%%%%%%%%%%%%%%%%%%%%%%%%%%%%%%%%
% Performance Calculations of Prototype Machine: Performance.nb      %
% Author:Danson Michael Joseph                                     %
% Modified: 24 November 2009                                       %
5  %-----%
% Comments: Change Section 3 for a different design                 %
%                                                                     %
%%%%%%%%%%%%%%%%%%%%%%%%%%%%%%%%%%%%%%%%%%%%%%%%%%%%%%%%%%%%%%%%%%%%%%%%%%*)

10 (*%%%%%%%%%%%%%%%%%%%%%%%%%%%%%%%%%%%%%%%%%%%%%%%%%%%%%%%%%%%%%%%%%%%%%%%%%%
% Section 1: Function Definitions                                     %
%-----*)
ClearAll["Global '*"];

15 (* Bessel Functions -----*)
I0[n_]:=BesselI[0,n];
I1[n_]:=BesselI[1,n];
K0[n_]:=BesselK[0,n];
K1[n_]:=BesselK[1,n];

20 (* Carter's Coefficient -----*)
Carter[gap_,q_]:= (
  spp=m*q;
  spp=m*q;
  Tsl=Tp/spp;
  To=Tsl/2;
  y=To/(2*gap);
  gamma=(4/Pi)*(y*ArcTan[y]-Log[Sqrt[1+y^2]]);
  kc=Tsl/(Tsl-gamma*gap)
30 );
%%%%%%%%%%%%%%%%%%%%%%%%%%%%%%%%%%%%%%%%%%%%%%%%%%%%%%%%%%%%%%%%%%%%%%%%%%*)

35 (*%%%%%%%%%%%%%%%%%%%%%%%%%%%%%%%%%%%%%%%%%%%%%%%%%%%%%%%%%%%%%%%%%%%%%%%%%%
% Section 2: Design Independent Parameters                           %
%-----*)
(* Constants -----*)
u0=4*Pi*10^-7;

40 (* Demagnetisation Curve -----*)
Hcb=960000;
urrecb=1.034;
Tbase=20;
ah=-0.69;
ab=-0.13;

45 (* Saturation Model -----*)
ku1=1.35*10^-4;
nu1=-0.35;
ku2=2.0*10^-6;
50 nu2=12.75;
%%%%%%%%%%%%%%%%%%%%%%%%%%%%%%%%%%%%%%%%%%%%%%%%%%%%%%%%%%%%%%%%%%%%%%%%%%*)

55 (*%%%%%%%%%%%%%%%%%%%%%%%%%%%%%%%%%%%%%%%%%%%%%%%%%%%%%%%%%%%%%%%%%%%%%%%%%%
% Section 3: Design Specific Parameters                             %
%-----*)

```

```

(* Operational Parameters -----*)
Topr=25;
Pc=0.005*0.8/0.0045;

60 (* Electrical Parameters -----*)
m=3;
qi=1;
qo=1;
aci=1.0;
65 aco=1.0;
(* 100% *)
Qi1100=8400;
Qo1100=14000;
(* 75% *)
70 Qi175=6400;
Qo175=10640;
(* 50% *)
Qi150=5400;
Qo150=7350;
75 (* 25% *)
Qi125=2000;
Qo125=3570;
Qi1=Qi1100;
Qo1=Qo1100;

80 (* Mechanical Parameters -----*)
ri=0.073;
Tp=0.06;
am=0.8;
85 Tm=am*Tp;
L=0.36;
kst=0.98;
lg=0.0045;
ltrans=0.005;
90 delta=Tp/2;
p=L/Tp;
lci=0.0335;
lco=0.014;
lsi=0.0605;
95 lso=0.0503;
lsli=lsi-lci;
lslo=lso-lco;
alphasl=0.5;
alphan=1-alphasl;
100 kfilli=0.125;
kfillo=0.155;
(*%%%%%%%%%%%%%%%%%%%%%%%%%%%%%%%%%%%%%%%%%%%%%%%%%%%%%%%%%%%%%%%%%%%%%%%%*)

(*%%%%%%%%%%%%%%%%%%%%%%%%%%%%%%%%%%%%%%%%%%%%%%%%%%%%%%%%%%%%%%%%%%%%%%%%
105 % Section 4: Initial Calculations %
%-----*)
(* Mechanical Dimensions -----*)
ro=ri+ltrans;
lm=lg*Pc/am;
110 b=Pi/Tp;
rmi=ri-lm;
rti=ri;
rsi=ri-lm-lgimvp;
rmo=ro+lm;
115 rto=ro;
rso=ro+lm+lgomvp;

```

```

(* Magnetic Operating Coercivity and Remnant Flux -----*)
120 Brb=u0*urrecb*Hcb;
Hc=Hcb*(1+ah*(Topr-Tbase)/100);
Br=Brb*(1+ab*(Topr-Tbase)/100);
urrec=Br/(u0*Hc);
kf=(4/Pi)*Sin[am*Pi/2];

125 (* Winding Factors -----*)
kwi=Sin[Pi/(2*m)]/(qi*Sin[Pi/(2*qi*m)])*Sin[Pi*aci*Tp/(2*Tp)];
kwo=Sin[Pi/(2*m)]/(qo*Sin[Pi/(2*qo*m)])*Sin[Pi*aco*Tp/(2*Tp)];

130 (* Slot-Depth Coefficient -----*)
kli=1/(kwi*kfilli*J*alphasl);
klo=1/(kwo*kfillo*J*alphasl);

(* Equivalent Air-gaps -----*)
135 kcomvp=Carter[lg,qo];
kcimvp=Carter[lg,qi];
lgomvp=kcomvp*lg;
lgimvp=kcimvp*lg;
kcor=Carter[lg+lm/urrec,qo];
kcir=Carter[lg+lm/urrec,qi];
140 lgor=kcor*(lg+lm/urrec);
lgir=kcir*(lg+lm/urrec);

(* Force Coefficients and Bessel Functions -----*)
145 kforce=Pi*L/(2*Tp);
ChIINum=rm rs rt (I1[b h rm] KO[b h rm]+IO[b h rm] K1[b h rm]);
ChIIDen=(IO[b h rt]+b h rt I1[b h rt]) (-(-1+urrec) IO[b h rs] KO[b h
rm] (KO[b h rm]-b h rm K1[b h rm])+b h rs (-1+urrec) I1[b h rs] KO
[b h rm] (-KO[b h rm]+b h rm K1[b h rm]))+(b h rm urrec I1[b h rm]
KO[b h rm]+IO[b h rm] ((-1+urrec) KO[b h rm]+b h rm K1[b h rm])) (
KO[b h rs]-b h rs K1[b h rs]))-(-b h rm I1[b h rm] (IO[b h rs]+b h
rs I1[b h rs]) KO[b h rm]-(-1+urrec) IO[b h rm]^2 (KO[b h rs]-b h
rs K1[b h rs])+IO[b h rm] (IO[b h rs] ((-1+urrec) KO[b h rm]-b h
rm urrec K1[b h rm])-b h (rs I1[b h rs] (-(-1+urrec) KO[b h rm]+b
h rm urrec K1[b h rm])+rm (-1+urrec) I1[b h rm] (KO[b h rs]-b h rs
K1[b h rs]))) (-KO[b h rt]+b h rt K1[b h rt]);
AhII=2 b h Qh u0 urrec/
(ksl*ksat)*ChII*(KO[h b r]/r-h*b*K1[h b r])/r->rt;
BhII=-2 b h Qh u0 urrec/
(ksl*ksat)*ChII*(IO[h b r]/r+h*b*I1[h b r])/r->rt;
150 KhII=AhII (rm I1[h b rm]-rt I1[h b rt])
+BhII (rt K1[h b rt]-rm K1[h b rm]);
Jm = Br/(u0*urrec);
RCi={rm->rmi,rt->rmi,rs->rmi,ksl->ksli,ksat->ksati,Qh->Qih};
155 RCo={rm->rmo,rt->rto,rs->rso,ksl->kslo,ksat->ksato,Qh->Qoh};

(* Magneto-Motive Forces -----*)
Fmp=Hc*lm*kf;
Fsip=2*Tp*Qih/(h*Pi);
160 Fsop=2*Tp*Qoh/(h*Pi);
Fip=Sqrt[Fmp^2+Fsip^2-2*Fmp*Fsip*Cos[b*delta]];
Fop=Sqrt[Fmp^2+Fsop^2-2*Fmp*Fsop*Cos[b*delta]];
Pfi=Fmp*Sin[b*delta]/Fip;
Pfo=Fmp*Sin[b*delta]/Fop;
165 (%%%%%%%%%%%%%%%%%%%%%%%%%%%%%%%%%%%%%%%%%%%%%%%%%%%%%%%%%%)
(%%%%%%%%%%%%%%%%%%%%%%%%%%%%%%%%%%%%%%%%%%%%%%%%%%%%%%%%%%)
% Section 5: Fundamental Performance Equations %

```

```

%-----*)
170 (* MVP Force -----*)
Fh =-4*Pi*p*Jm*KhII*Sin[h*am*Pi/2]*Sin[h*b*delta];
Fiph=Fh/.RCi;
Foph=Fh/.RCo;
EqnForce=Fhp==(Fiph+Foph)/.h->1;

175 (* Magnetic Saturation -----*)
EqnBti=Bt==Phip/(2*Pi*(ri-lm-lg-lsli)*alphan*Tp*kst);
EqnBci=Bc==(Phip/2)/(Pi*((ri-lm-lg-lsli)^2-(ri-lm-lg-lsli-lci)^2));
EqnBco=Bc==(Phop/2)/(Pi*((ro+lm+lg+lslo+lco)^2-(ro+lm+lg+lslo)^2));

180 (* Harmonic Flux Linkage -----*)
Phiph=Fiph/(kforce*Qih);
Phoph=Foph/(kforce*Qoh);

185 (* Total Flux Linkage -----*)
kflux=Sum[Phiph/.h->hh,{hh,1,3,2}]/Phiph/.h->1;
Phip=kflux*Phiph;
Phop=kflux*Phoph;

190 (* Reluctances -----*)
(* Air-gaps *)
Rai=Log[ri/(ri-lgir)]/(2*u0*Pi*Tp);
Rao=Log[(ro+lgor)/ro]/(2*u0*Pi*Tp);

195 (* Translator Core *)
A=Pi*(ro^2-ri^2);
l=(1-am)*Tp+Pi*(ri+ro);
Phict=(Phop-Phip)/2;
Rct=1/(u0)*( ku1*Phict^nu1/A^(nu1+1) + ku2*Phict^nu2/A^(nu2+1));

200 (* Inner Core *)
r1=ri-lm-lg-lsli-lci/2;
r2=ri-lm-lg-lsli;
RAi=(-ku1*Phip^nu1)/
205 (2^nu1*u0*nu1*(Pi*Tp*kst)^(nu1+1))*(r2^(-nu1)-r1^(-nu1))
+(-ku2*Phip^nu2)/
(2^nu2*u0*nu2*(Pi*Tp*kst)^(nu2+1))*(r2^(-nu2)-r1^(-nu2));
r3=ri-lm-lg-lsli-lci;
r4=ri-lm-lg-lsli;
210 A=Pi*(r4^2-r3^2)*kst;
l=Tp/4;
RBi=((1/u0)*( ku1*Phip^nu1/(2^nu1*A^(nu1+1))
+ku2*Phip^nu2/(2^nu2*A^(nu2+1)) ));
Rci=2*(RAi+RBi);

215 (* Outer Core *)
r1=ro+lm+lg+lslo;
r2=ro+lm+lg+lslo+lco/2;
RAo=(-ku1*Phop^nu1)/
220 (2^nu1*u0*nu1*(Pi*Tp*kst)^(nu1+1))*(r2^(-nu1)-r1^(-nu1))
+(-ku2*Phop^nu2)/
(2^nu2*u0*nu2*(Pi*Tp*kst)^(nu2+1))*(r2^(-nu2)-r1^(-nu2));
r3=ro+lm+lg+lslo;
r4=ro+lm+lg+lslo+lco;
225 A=Pi*(r4^2-r3^2)*kst;
l=Tp/4;
RBo=((1/u0)*( ku1*Phop^nu1/(2^nu1*A^(nu1+1))
+ku2*Phop^nu2/(2^nu2*A^(nu2+1)) ));
Rco=2*(RAo+RBo);

```

```

230 (* Inner Teeth *)
    r1=ri-lm-lg-lsli;
    r2=ri-lm-lg;
    kai=2*Pi*alphan*alpha*tp*kst;
235 Rti=((ku1*Phip^nu1)/(-nu1*u0*kai^(nu1+1))*(r2^(-nu1)-r1^(-nu1))
        +(ku2*Phip^nu2)/(-nu2*u0*kai^(nu2+1))*(r2^(-nu2)-r1^(-nu2)));

    (* Outer Teeth *)
    r1=ro+lm+lg;
240 r2=ro+lm+lg+lslo;
    kao=2*Pi*alphan*alpha*tp*kst;
    Rto=((ku1*Phop^nu1)/(-nu1*u0*kao^(nu1+1))*(r2^(-nu1)-r1^(-nu1))
        +(ku2*Phop^nu2)/(-nu2*u0*kao^(nu2+1))*(r2^(-nu2)-r1^(-nu2)));

245 (* Slot *)
    r1=ri-lm-lg-lsli;
    r2=ri-lm-lg;
    Gsli=(Pi*u0)/(6*tp)*(3*r2^2-2*r2*r1-r1^2);
    Rsli=qi/Gsli;
250 r1=ro+lm+lg;
    r2=ro+lm+lg+lslo;
    Gslo=(Pi*u0)/(6*tp)*(3*r2^2-2*r2*r1-r1^2);
    Rslo=qo/Gslo;

255 (* Saturation Factors -----*)
    Cflux = Phop/Phip;
    Ksati=1+(4*Rti+Rci+(1-Cflux)*Rct)/(4*Rai);
    Ksato=1+(4*Rto+Rco+(1-1/Cflux)*Rct)/(4*Rao);

260 (* Slot Leakage Factors -----*)
    Ksli=(Rsli+4*Rai)/Rsli;
    Kslo=(Rslo+4*Rao)/Rslo;
    (%%%%%%%%%%%%%%%%%%%%%%%%%%%%%%%%%%%%%%%%%%%%%%%%%%%%%%%%%%)

265 (%%%%%%%%%%%%%%%%%%%%%%%%%%%%%%%%%%%%%%%%%%%%%%%%%%%%%%%%%%)
    % Section 6: Performance Calculation %
    %-----*)
    (* Calculate Slot-Leakage and Saturation Factors -----*)
    IC={ksati->1.05,ksato->1.05,ksli->1.1,kslo->1.1};
270 sum1=Round[(ksati+ksato+ksli+kslo)*1000000/.IC];
    step=1.0;
    While[step>0,
        CC=Join[IC,{Qoh->Qo1,Qih->Qi1,h->1}];
        IC={ksati->((ksati+Ksati)/2/.CC),
275         ksato->((ksato+Ksato)/2/.CC),
            ksli->(Ksli/.CC),kslo->(Kslo/.CC)
        };
        sum2=Round[(ksati+ksato+ksli+kslo)*1000000/.IC];
        step=sum1-sum2;
280 sum1=sum2;
    ]

    (* Calculate the Force-----*)
    FC=CC;
285 Print["Saturation and Slot Leakage Factors: ",IC]
    (*Excluding Slot Leakage and Saturation*)
    Fi1=Fiph*ksli*ksati/.FC;
    Fo1=Foph*kslo*ksato/.FC;
    F=Fi1+Fo1;
290 Print["Force Excluding Saturation and Slot Leakage: ", F, " N"];

```


Script A.2: Machine Design Script

```

1  (*%%%%%%%%%%%%%%%%%%%%%%%%%%%%%%%%%%%%%%%%%%%%%%%%%%%%%%%%%%%%%%%%%%%%%%%%%
% Full-Scale Machine Design : Design.nb
% Author:Danson Michael Joseph
% Modified: 24 November 2009
5  %-----%
% Comments: Change Section 3 for a different design
%
%%%%%%%%%%%%%%%%%%%%%%%%%%%%%%%%%%%%%%%%%%%%%%%%%%%%%%%%%%%%%%%%%%%%%%%%%*)

10 (*%%%%%%%%%%%%%%%%%%%%%%%%%%%%%%%%%%%%%%%%%%%%%%%%%%%%%%%%%%%%%%%%%%%%%%%%%
% Section 1: Function Definitions
%-----*)
ClearAll["Global '*"];

15 (* Bessel Functions -----*)
I0[n_]:=BesselI[0,n];
I1[n_]:=BesselI[1,n];
K0[n_]:=BesselK[0,n];
K1[n_]:=BesselK[1,n];

20 (* Carter's Coefficient -----*)
Carter[gap_,q_]:= (
    spp=m*q;
    spp=m*q;
25    Tsl=Tp/spp;
    To=Tsl/2;
    y=To/(2*gap);
    gamma=(4/Pi)*(y*ArcTan[y]-Log[Sqrt[1+y^2]]);
    kc=Tsl/(Tsl-gamma*gap)
30 );
%%%%%%%%%%%%%%%%%%%%%%%%%%%%%%%%%%%%%%%%%%%%%%%%%%%%%%%%%%%%%%%%%%%%%%%%%

35 (*%%%%%%%%%%%%%%%%%%%%%%%%%%%%%%%%%%%%%%%%%%%%%%%%%%%%%%%%%%%%%%%%%%%%%%%%%
% Section 2: Design Independent Parameters
%-----*)
(* Constants -----*)
u0=4*Pi*10^-7;

40 (* Demagnetisation Curve -----*)
Hcb=960000;
urrecb=1.034;
Tbase=20;
ah=-0.69;
ab=-0.13;

45 (* Saturation Model -----*)
ku1=1.35*10^-4;
nu1=-0.35;
ku2=2.0*10^-6;
50 nu2=12.75;
%%%%%%%%%%%%%%%%%%%%%%%%%%%%%%%%%%%%%%%%%%%%%%%%%%%%%%%%%%%%%%%%%%%%%%%%%

55 (*%%%%%%%%%%%%%%%%%%%%%%%%%%%%%%%%%%%%%%%%%%%%%%%%%%%%%%%%%%%%%%%%%%%%%%%%%
% Section 3: Design Specific Parameters
%-----*)
(* Operational Parameters -----*)
Topr=30;
Fhp=1000000;

60 (* Magnetic Parameters -----*)

```

```

Bc=1.5;
Bt=1.8;
Pc=2.4;

65 (* Electrical Parameters -----*)
m=3;
qi=1;
qo=1;
kfilli=0.585;
70 kfillo=0.585;
J=4*10^6;
aci=1.0;
aco=1.0;

75 (* Mechanical Parameters -----*)
rmin=0.225;
rmax=0.325;
rstep=0.001;

80 rr=Table[r,{r,rmin,rmax,rstep}];
Tp=0.1;
am=0.8;
Tm=am*Tp;
L=5;
85 kst=0.98;
lg=0.005;
delta=Tp/2;
p=L/Tp;
at=0.5;
90 alphasl=0.5;
alphanat=1-alphasl;

rhosteel=7850;
rhomag=7400;
95 Lmag=7;
g=9.8;
Pdesign=25*10^6;
Ltransmin=0.010;
(*%%%%%%%%%%%%%%%%%%%%%%%%%%%%%%%%%%%%%%%%%%%%%%%%%%%%%%%%%%%%%%%%%%%%%%%%*)
100 (*%%%%%%%%%%%%%%%%%%%%%%%%%%%%%%%%%%%%%%%%%%%%%%%%%%%%%%%%%%%%%%%%%%%%%%%%*)
% Section 4: Initial Calculations %
%-----*)
(* Mechanical Dimensions -----*)
105 (*ro=ri+ltrans;*)
lm=lg*Pc/am;
b=Pi/Tp;
rmi=ri-lm;
rti=ri;
110 rsi=ri-lm-lgimvp;
rmo=ro+lm;
rto=ro;
rso=ro+lm+lgomvp;

115 (* Magnetic Operating Coercivity and Remnant Flux -----*)
Brb=u0*urrecb*Hcb;
Hc=Hcb*(1+ah*(Topr-Tbase)/100);
Br=Brb*(1+ab*(Topr-Tbase)/100);
urrec=Br/(u0*Hc);
120 kf=(4/Pi)*Sin[am*Pi/2];

```

```

(* Winding Factors -----*)
kwi=Sin[Pi/(2*m)]/(qi*Sin[Pi/(2*qi*m)])*Sin[Pi*aci*Tp/(2*Tp)];
kwo=Sin[Pi/(2*m)]/(qo*Sin[Pi/(2*qo*m)])*Sin[Pi*aco*Tp/(2*Tp)];
125
(* Slot-Depth Coefficient -----*)
kli=1/(kwi*kfilli*J*alphasl);
klo=1/(kwo*kfillo*J*alphasl);
lsli=If[ValueQ[lsli],lsli,kli*Qih];
130 lslo=If[ValueQ[lslo],lslo,klo*Qoh];

(* Equivalent Air-gaps -----*)
kcomvp=Carter[lg,qo];
kcimvp=Carter[lg,qi];
135 lgomvp=kcomvp*lg;
lgimvp=kcimvp*lg;
kcor=Carter[lg+lm/urrec,qo];
kcir=Carter[lg+lm/urrec,qi];
lgor=kcor*(lg+lm/urrec);
140 lgir=kcir*(lg+lm/urrec);

(* Force Coefficients and Bessel Functions -----*)
kforce=Pi*L/(2*Tp);
ChIINum=rm rs rt (I1[b h rm] KO[b h rm]+IO[b h rm] K1[b h rm]);
145 ChIIDen=(IO[b h rt]+b h rt I1[b h rt]) (-(-1+urrec) IO[b h rs] KO[b h
rm] (KO[b h rm]-b h rm K1[b h rm])+b h rs (-1+urrec) I1[b h rs] KO
[b h rm] (-KO[b h rm]+b h rm K1[b h rm]))+(b h rm urrec I1[b h rm]
KO[b h rm]+IO[b h rm] ((-1+urrec) KO[b h rm]+b h rm K1[b h rm])) (
KO[b h rs]-b h rs K1[b h rs]))-(-b h rm I1[b h rm] (IO[b h rs]+b h
rs I1[b h rs]) KO[b h rm]-(-1+urrec) IO[b h rm]^2 (KO[b h rs]-b h
rm urrec K1[b h rs])+IO[b h rm] (IO[b h rs] ((-1+urrec) KO[b h rm]-b h
rm urrec K1[b h rm])-b h (rs I1[b h rs] (-(-1+urrec) KO[b h rm]+b
h rm urrec K1[b h rm]))+rm (-1+urrec) I1[b h rm] (KO[b h rs]-b h rs
K1[b h rs])))) (-KO[b h rt]+b h rt K1[b h rt]);
ChII=ChIINum/ChIIDen;
AhII=2 b h Qh u0 urrec/
(ksl*ksat)*ChII*(KO[h b r]/r-h*b*K1[h b r])/r->rt;
BhII=-2 b h Qh u0 urrec/
150 (ksl*ksat)*ChII*(IO[h b r]/r+h*b*I1[h b r])/r->rt;
KhII=AhII (rm I1[h b rm]-rt I1[h b rt])
+BhII (rt K1[h b rt]-rm K1[h b rm]);
Jm = Br/(u0*urrec);
RCi={rm->rmi,rt->rmi,rs->rmi,ksl->ksli,ksat->ksati,Qh->Qih};
155 RCo={rm->rmo,rt->rto,rs->rso,ksl->kslo,ksat->ksato,Qh->Qoh};

(* Magneto-Motive Forces -----*)
Fmp=Hc*lm*kf;
Fsip=2*Tp*Qih/(h*Pi);
160 Fsop=2*Tp*Qoh/(h*Pi);
Fip=Sqrt[Fmp^2+Fsip^2-2*Fmp*Fsip*Cos[b*delta]];
Fop=Sqrt[Fmp^2+Fsop^2-2*Fmp*Fsop*Cos[b*delta]];
PFI=Fmp*Sin[b*delta]/Fip;
PFo=Fmp*Sin[b*delta]/Fop;
165

(* Translator Core Thickness -----*)
Acore=Pi*(ro^2-ri^2);
Vcore=Lmag*Acore;
Mcore=rhosteel*Vcore;
170
Amag =Pi*( (ri^2-(ri-lm)^2) +((ro+lm)^2-ro^2));
Vmag = Amag*Lmag/Tp*Tm;
Mmag = rhomag*Vmag;

```

```

175 Mt=Mmag+Mcore;
    Ft =Fhp+Mt*g;
    P=Ft/Acore;
    (*%%%%%%%%%%%%%%%%%%%%%%%%%%%%%%%%%%%%%%%%%%%%%%%%%%%%%%%%%%%%%%%%%%%%%%%%*)

180 (*%%%%%%%%%%%%%%%%%%%%%%%%%%%%%%%%%%%%%%%%%%%%%%%%%%%%%%%%%%%%%%%%%%%%%%%%
    % Section 5: Fundamental Performance Equations %
    %-----*)
    (* Translator Mechanical Thickness -----*)
    EqnMech=Pdesign==P;

185 (* MVP Force -----*)
    Fh =-4*Pi*p*Jm*KhII*Sin[h*am*Pi/2]*Sin[h*b*delta];
    Fiph=Fh/.RCi;
    Foph=Fh/.RCo;
190 EqnForce=Fhp==(Fiph+Foph)/.h->1;

    (* Magnetic Saturation -----*)
    EqnBti=Bt==Phip/(2*Pi*(ri-lm-lg-lsli)*alphan*Tp*kst);
    EqnBci=Bc==(Phip/2)/(Pi*((ri-lm-lg-lsli)^2-(ri-lm-lg-lsli-lci)^2));
195 EqnBco=Bc==(Phop/2)/(Pi*((ro+lm+lg+lslo+lco)^2-(ro+lm+lg+lslo)^2));

    (* Harmonic Flux Linkage -----*)
    Phiph=Fiph/(kforce*Qih);
    Phoph=Foph/(kforce*Qoh);

200 (* Total Flux Linkage -----*)
    kflux=Sum[Phiph/.h->hh,{hh,1,3,2}]/Phiph/.h->1;
    Phip=kflux*Phiph;
    Phop=kflux*Phoph;

205 (* Reluctances -----*)
    (* Air-gaps *)
    Rai=Log[ri/(ri-lgir)]/(2*u0*Pi*Tp);
    Rao=Log[(ro+lgor)/ro]/(2*u0*Pi*Tp);

210 (* Translator Core *)
    A=Pi*(ro^2-ri^2);
    l=(1-am)*Tp+Pi*(ri+ro);
    Phict=(Phop-Phip)/2;
215 Rct=1/(u0)*( ku1*Phict^nu1/A^(nu1+1) + ku2*Phict^nu2/A^(nu2+1));

    (* Inner Core *)
    r1=ri-lm-lg-lsli-lci/2;
    r2=ri-lm-lg-lsli;
220 RAi=((-ku1*Phip^nu1)/
        (2^nu1*u0*nu1*(Pi*Tp*kst)^(nu1+1))*(r2^(-nu1)-r1^(-nu1))
        +(-ku2*Phip^nu2)/
        (2^nu2*u0*nu2*(Pi*Tp*kst)^(nu2+1))*(r2^(-nu2)-r1^(-nu2)));
    r3=ri-lm-lg-lsli-lci;
225 r4=ri-lm-lg-lsli;
    A=Pi*(r4^2-r3^2)*kst;
    l=Tp/4;
    RBi=((1/u0)*( ku1*Phip^nu1/(2^nu1*A^(nu1+1))
        +ku2*Phip^nu2/(2^nu2*A^(nu2+1)) ));
230 Rci=2*(RAi+RBi);

    (* Outer Core *)
    r1=ro+lm+lg+lslo;
    r2=ro+lm+lg+lslo+lco/2;

```

```

235 | RAo=((-ku1*Phop^nu1)/
      |      (2^nu1*u0*nu1*(Pi*Tp*kst)^(nu1+1))*(r2^(-nu1)-r1^(-nu1))
      |      +(-ku2*Phop^nu2)/
      |      (2^nu2*u0*nu2*(Pi*Tp*kst)^(nu2+1))*(r2^(-nu2)-r1^(-nu2)));
      | r3=ro+lm+lg+lslo;
240 | r4=ro+lm+lg+lslo+lco;
      | A=Pi*(r4^2-r3^2)*kst;
      | l=Tp/4;
      | RBo=((1/u0)*( ku1*Phop^nu1/(2^nu1*A^(nu1+1))
      |      +ku2*Phop^nu2/(2^nu2*A^(nu2+1)) ));
245 | Rco=2*(RAo+RBo);

      | (* Inner Teeth *)
      | r1=ri-lm-lg-lsli;
      | r2=ri-lm-lg;
250 | kai=2*Pi*alphan*Tp*kst;
      | Rti=((ku1*Phip^nu1)/(-nu1*u0*kai^(nu1+1))*(r2^(-nu1)-r1^(-nu1))
      |      +(ku2*Phip^nu2)/(-nu2*u0*kai^(nu2+1))*(r2^(-nu2)-r1^(-nu2)));

      | (* Outer Teeth *)
255 | r1=ro+lm+lg;
      | r2=ro+lm+lg+lslo;
      | kao=2*Pi*alphan*Tp*kst;
      | Rto=((ku1*Phop^nu1)/(-nu1*u0*kao^(nu1+1))*(r2^(-nu1)-r1^(-nu1))
      |      +(ku2*Phop^nu2)/(-nu2*u0*kao^(nu2+1))*(r2^(-nu2)-r1^(-nu2)));
260 |

      | (* Slot *)
      | r1=ri-lm-lg-lsli;
      | r2=ri-lm-lg;
      | Gsli=(Pi*u0)/(6*Tp)*(3*r2^2-2*r2*r1-r1^2);
265 | Rsli=qi/Gsli;
      | r1=ro+lm+lg;
      | r2=ro+lm+lg+lslo;
      | Gslo=(Pi*u0)/(6*Tp)*(3*r2^2-2*r2*r1-r1^2);
      | Rslo=qo/Gslo;
270 |

      | (* Saturation Factors -----*)
      | Cflux = Phop/Phip;
      | Ksati=1+(4*Rti+Rci+(1-Cflux)*Rct)/(4*Rai);
      | Ksato=1+(4*Rto+Rco+(1-1/Cflux)*Rct)/(4*Rao);
275 |

      | (* Slot Leakage Factors -----*)
      | Ksli=(Rsli+4*Rai)/Rsli;
      | Kslo=(Rslo+4*Rao)/Rslo;

280 | (%%%%%%%%%%%%%%%%%%%%%%%%%%%%%%%%%%%%%%%%%%%%%%%%%%%%%%%%%%%%%%%%%%%%%%%%%)
      |
      | (%%%%%%%%%%%%%%%%%%%%%%%%%%%%%%%%%%%%%%%%%%%%%%%%%%%%%%%%%%%%%%%%%%%%%%%%%)
      | % Section 6: Design Calculations %
      | %-----*)
285 | solutions={};
      | area={};
      | magvolume={};
      | volume={};
      | footprint={};
290 | Qis={};
      | Qos={};
      | QiQo={};
      | Phips={};
      | Phops={};
295 | PFis={};

```

```

PFos={};

(* For loop through the various radii values -----*)
For[r=rmin,r<=rmax,r=r+rstep,
300  IC={ksati->1.02,ksato->1.02,ksli->1.2,kslo->1.2};
    sum1=Round[(ksati+ksato+ksli+kslo)*1000000/.IC];
    step=1.0;
    solnro=Solve[EqnMech/.ri->r][[2]];
    (* While loop to determine ksatz and kslx -----*)
305  While[step>0,
    CC=Join[IC,{h->1},{ri->r},solnro];
    eqns={EqnForce/.CC,EqnBti/.CC,EqnBci/.CC};
    Solns=Solve[eqns][[1]];
    res=Append[Solns,Solve[EqnBco/.Solns/.CC][[2]][[1]]];
310  IC={ksati->((ksati+Ksati)/2/.CC),
    ksato->((ksato+Ksato)/2/.CC),
    ksli->(Ksli/.CC),kslo->(Kslo/.CC)
    }/.res;
    sum2=Round[(ksati+ksato+ksli+kslo)*1000000/.IC];
315  step=sum1-sum2;
    sum1=sum2;
];

(* Generate the design lists -----*)
res=Join[res,CC];
320  design=Append[design,ros->(ro/.res)];
    design=Append[design,lsi->((kli*Qih+lci)/.res)];
    design=Append[design,lso->((klo*Qoh+lco)/.res)];
    design=Append[design,lsli->((kli*Qih)/.res)];
    design=Append[design,lslos->((klo*Qoh)/.res)];
325  solutions=Append[solutions,design];
    area=Append[area,
    (Pi*((ro+lm+lg+lso)^2-(ri-lm-lg-lsi)^2)/.design];
    footprint=Append[footprint,
    (Pi*(ro+lm+lg+lso)^2)/.design];
330  volume=Append[volume,
    (L*Pi*((ro+lm+lg+lso)^2-(ri-lm-lg-lsi)^2)/.design];
    magvolume=Append[magvolume,
    (p*Tm*Pi*(ri^2-(ri-lm)^2+((ro+lm)^2-ro^2))/.design];
    Qis=Append[Qis,(Qih/.design)];
335  Qos=Append[Qos,(Qoh/.design)];
    QiQo=Append[QiQo,(Abs[Qih-Qoh]/.design)];
    Phips=Append[Phips,(Phiph/.design)];
    Phops=Append[Phops,(Phiph/.design)];
    PFis=Append[PFis,(PFI/.design)];
340  PFos=Append[PFos,(PFo/.design)];
]

(*%%%%%%%%%%%%%%%%%%%%%%%%%%%%%%%%%%%%%%%%%%%%%%%%%%%%%%%%%%%%%%%%%%%%%%%%%%%%%%*)

(*%%%%%%%%%%%%%%%%%%%%%%%%%%%%%%%%%%%%%%%%%%%%%%%%%%%%%%%%%%%%%%%%%%%%%%%%%%%%%%
345 % Section 7: Design Plots and Exports to File %
%-----*)

SetDirectory[NotebookDirectory[]];

(* Electrical Loadings: Qi, Qo and |Qi-Qo| -----*)
350 Export["Qi.txt",Table[{rr[[n]],Qis[[n]]},
    {n,1,Length[rr]}],"TSV"];
ListLinePlot[
    Table[{rr[[n]],Qis[[n]]},{n,1,Length[rr]}],
    AxesOrigin->{rmin,0.9*Min[Qis]},PlotLabel->"Qi vs. ri"
355 ]
Export["Qo.txt",Table[{rr[[n]],Qos[[n]]},

```

```

    {n,1,Length[rr]}], "TSV"];
ListLinePlot[
  Table[{rr[[n]], Qos[[n]]}, {n,1,Length[rr]}],
360 AxesOrigin->{rmin,0.9*Min[Qos]}, PlotLabel->"Qo vs. ri"
]
Export["QiQo.txt", Table[{rr[[n]], QiQo[[n]]},
  {n,1,Length[rr]}], "TSV"];
ListLinePlot[
365 Table[{rr[[n]], QiQo[[n]]}, {n,1,Length[rr]}],
  AxesOrigin->{rmin,0}, PlotLabel->"|Qi-Qo| vs. ri"
]

(* Inner and Outer Power Factor -----*)
370 Export["PFI.txt", Table[{rr[[n]], PFis[[n]]},
  {n,1,Length[rr]}], "TSV"];
ListLinePlot[
  Table[{rr[[n]], PFis[[n]]}, {n,1,Length[rr]}],
375 AxesOrigin->{rmin,0.9*Min[PFis]},
  PlotLabel->"PFI vs. ri"
]
Export["PFO.txt", Table[{rr[[n]], PFos[[n]]},
  {n,1,Length[rr]}], "TSV"];
ListLinePlot[
380 Table[{rr[[n]], PFos[[n]]}, {n,1,Length[rr]}],
  AxesOrigin->{rmin,0.9*Min[PFos]},
  PlotLabel->"PFO vs. ri"
]

385 (* Inner and Outer Magnetic Flux -----*)
Export["Phip.txt", Table[{rr[[n]], Phips[[n]]},
  {n,1,Length[rr]}], "TSV"];
ListLinePlot[
  Table[{rr[[n]], Phips[[n]]}, {n,1,Length[rr]}],
390 AxesOrigin->{rmin,0.9*Min[Phips]},
  PlotLabel->"Phip vs. ri"
]
Export["Phop.txt", Table[{rr[[n]], Phops[[n]]},
  {n,1,Length[rr]}], "TSV"];
395 ListLinePlot[
  Table[{rr[[n]], Phops[[n]]}, {n,1,Length[rr]}],
  AxesOrigin->{rmin,0.9*Min[Phops]},
  PlotLabel->"Phop vs. ri"
]
400

(* Area, Volume, Magnet Volume and Footprint -----*)
Export["MagVolume.txt", Table[{rr[[n]], magvolume[[n]]},
  {n,1,Length[rr]}], "TSV"];
ListLinePlot[
405 Table[{rr[[n]], magvolume[[n]]}, {n,1,Length[rr]}],
  AxesOrigin->{rmin,0.9*Min[magvolume]},
  PlotLabel->"Magnet Volume vs. ri"
]
Export["Volume.txt", Table[{rr[[n]], volume[[n]]},
  {n,1,Length[rr]}], "TSV"];
410 ListLinePlot[
  Table[{rr[[n]], volume[[n]]}, {n,1,Length[rr]}],
  AxesOrigin->{rmin,0.9*Min[volume]},
  PlotLabel->"Machine Volume vs. ri"
]
415
Export["Area.txt", Table[{rr[[n]], area[[n]]},
  {n,1,Length[rr]}], "TSV"];

```


A.2 FEMM Lua Simulation Scripts

Script A.4: System Construction & Simulation: Double-Sided Tubular Machine

```

1  --%%%%%%%%%%%%%%%%%%%%%%%%%%%%%%%%%%%%%%%%%%%%%%%%%%%%%%%%%%%%%%%%%%%%%%%%%%%%%%--
-- Simulation Script: Double-Sided Tubular Version: simulation.lua --
-- Author: Danson Michael Joseph --
-- Modified: 24 November 2009 --
5  -----
-- Comments: --
--     1) This file relies on symbolic links and files: --
--         a) parameters.lua --> parameters.xxx.lua --
--         b) functions.lua --
10 -----
--%%%%%%%%%%%%%%%%%%%%%%%%%%%%%%%%%%%%%%%%%%%%%%%%%%%%%%%%%%%%%%%%%%%%%%%%%%%%%%--
-- Section 1: Load Parameters From File --
15 -----
dofile("parameters.lua");
dofile("functions.lua");
--%%%%%%%%%%%%%%%%%%%%%%%%%%%%%%%%%%%%%%%%%%%%%%%%%%%%%%%%%%%%%%%%%%%%%%%%%%%%%%--
20 -----
-- Section 2: System Construction --
-----
-- Setup the Simulation -----
clearconsole();
25 open("template.fem");
mi_probdef(simfrequency, simunits, simtype, simprecision, simdepth,
           simminangle);

-- Set the Magnets' Operating Values -----
30 mi_modifymaterial("Mag",1,urrec);
mi_modifymaterial("Mag",2,urrec);
mi_modifymaterial("Mag",3,Hc);

-- Create the Boundary Box -----
build_box(left,right,bottom,top,"A=0","Air",0,left+0.1,bottom+0.1,
           air_automesh,air_meshsize,0);
35 -----
-- Build Magnet Array -----
build_box(ri,ro,bottom_start_mag,bottom_start_mag +Lmag,"",steel,0,(ri
+ro)/2,bottom_start_mag+Lmag/2,core_automesh,core_meshsize,900);
for m=0,no_magnets-1,1 do
40     build_magnet(m,ri-lm);
     build_magnet(m,ro);
end

-- Build Stators -----
Nc=Ni;
45 build_lam(ri - lm - lg,ri - lm - lg - lsi, -lsi,"Ai","Bi","Ci");
Nc=No;
build_lam(ro + lm + lg,ro + lm + lg + lso,lslo,"Ao","Bo","Co");

--Build the Air-gaps -----
50 build_airgap(bottom_start_mag,bottom_start_mag+Lmag,bottom_start_lam,
              bottom_start_lam+L,ri,ri-lm-lg,"A=0","Air",0,ri-lm-lg+0.5,
              bottom_start_mag+0.5,airgap_automesh,airgap_meshsize,900);
build_airgap(bottom_start_mag,bottom_start_mag+Lmag,bottom_start_lam,
              bottom_start_lam+L,ro,ro+lm+lg,"A=0","Air",0,ro+lm+lg-0.5,

```


Script A.6: Simulation Post-Processing: Double-Sided Tubular Machine

```

1  --%%%%%%%%%%%%%%%%%%%%%%%%%%%%%%%%%%%%%%%%%%%%%%%%%%%%%%%%%%%%%%%%%%%%%%%%%%%%%%--
-- Postprocessing: Double-Sided Tubular Version: postprocessing.lua --
-- Author: Danson Michael Joseph --
-- Modified: 24 November 2009 --
5  -----
-- Comments: Requires parameters.lua --> parameters.xxx.lua --
-- -----
--%%%%%%%%%%%%%%%%%%%%%%%%%%%%%%%%%%%%%%%%%%%%%%%%%%%%%%%%%%%%%%%%%%%%%%%%%%%%%%--
10 --%%%%%%%%%%%%%%%%%%%%%%%%%%%%%%%%%%%%%%%%%%%%%%%%%%%%%%%%%%%%%%%%%%%%%%%%%%%%%%--
-- Section 1: Load Parameters From File --
-----
dofile("parameters.lua");
--%%%%%%%%%%%%%%%%%%%%%%%%%%%%%%%%%%%%%%%%%%%%%%%%%%%%%%%%%%%%%%%%%%%%%%%%%%%%%%--
15 --%%%%%%%%%%%%%%%%%%%%%%%%%%%%%%%%%%%%%%%%%%%%%%%%%%%%%%%%%%%%%%%%%%%%%%%%%%%%%%--
-- Section 2: Process Simulated Data --
-----
clearconsole();
20 ForceString = "";
CoreFluxString = "";
CoreFluxDensityString = "";
ToothFluxString = "";
ToothFluxDensityString = "";
25 FluxAo = "";
FluxBo = "";
FluxCo = "";
FluxAi = "";
FluxBi = "";
30 FluxCi = "";

-- Processing of each Simulation -----
for n=1,numi,1 do -- Current configuration
  SimString = "";
35  for i=0,periods*steps-1,1 do -- Axial step
    -- Load Solution File -----
    bottom2 = bottom_start_mag+i*Tp/steps;
    open("SimulationFiles/Simulation"..n.."..i"..fem");
    mi_loadsolution();
40
    -- Extract Forces -----
    mo_seteditmode("block");
    mo_selectblock((ri+ro)/2,bottom2+maggap);
    for m=0,no_magnets-1,1 do
45      mo_selectblock((ri+ro)/2+biw,bottom2+Tp/2+Tp*m);
      mo_selectblock((ri+ro)/2-biw,bottom2+Tp/2+Tp*m);
    end
    SimString = (SimString..i.." ");
    ForceString = (ForceString..mo_blockintegral(19).." ");
50
    -- Stator Core Flux -----
    mo_seteditmode("segments");
    mo_clearcontour();
    mo_addcontour(ri-lm-lg-lsli,bottom_start_lam+Tp*p/2);
55  mo_addcontour(ri-lm-lg-lsli-lci,bottom_start_lam+Tp*p/2);
    CoreFlux,CoreFluxDensity = mo_lineintegral(0);
    CoreFluxString = (CoreFluxString..CoreFlux.." ");
    CoreFluxDensityString = (CoreFluxDensityString..
      CoreFluxDensity.." ");
    mo_clearcontour();

```

```

60     mo_addcontour(ri-lm-lg-lsli,bottom_start_lam+Tp*p/2+Tp*alphan
        /6);
    mo_addcontour(ri-lm-lg-lsli,bottom_start_lam+Tp*p/2-Tp*alphan
        /6);
    ToothFlux,ToothFluxDensity = mo_lineintegral(0);
    ToothFluxString = (ToothFluxString..CoreFlux.." ");
    ToothFluxDensityString = (ToothFluxDensityString..
        ToothFluxDensity.." ");
65     mo_clearcontour();

    -- Flux Linkage -----
    dummy1,dummy2,LinkAo = mo_getcircuitproperties("Ao")
    FluxAo = (FluxAo..LinkAo.." ");
70     dummy1,dummy2,LinkBo = mo_getcircuitproperties("Bo")
    FluxBo = (FluxBo..LinkBo.." ");
    dummy1,dummy2,LinkCo = mo_getcircuitproperties("Co")
    FluxCo = (FluxCo..LinkCo.." ");
    dummy1,dummy2,LinkAi = mo_getcircuitproperties("Ai")
75     FluxAi = (FluxAi..LinkAi.." ");
    dummy1,dummy2,LinkBi = mo_getcircuitproperties("Bi")
    FluxBi = (FluxBi..LinkBi.." ");
    dummy1,dummy2,LinkCi = mo_getcircuitproperties("Ci")
    FluxCi = (FluxCi..LinkCi.." ");
80

    mo_close();
    mi_close();
    end -- End of axial step
    -- Prepare for the next current configuration -----
85     ForceString = (ForceString.."\\n");
    CoreFluxString = (CoreFluxString.."\\n");
    CoreFluxDensityString = (CoreFluxDensityString.."\\n");
    ToothFluxString = (ToothFluxString.."\\n");
    ToothFluxDensityString = (ToothFluxDensityString.."\\n");
90     FluxAo = (FluxAo.."\\n");
    FluxBo = (FluxBo.."\\n");
    FluxCo = (FluxCo.."\\n");
    FluxAi = (FluxAi.."\\n");
    FluxBi = (FluxBi.."\\n");
95     FluxCi = (FluxCi.."\\n");
    end -- End of current configuration

    -- Write Data to File in Octave Format -----
    forcefile = openfile("simulations.octave","w+");
100    write(forcefile, "# name: S\\n# type: matrix\\n# rows: "..(11*numi+1)..
        "\\n# columns: "..periods*steps.."\\n");
    write(forcefile, SimString,"\\n");
    write(forcefile, ForceString,"\\n");
    write(forcefile, CoreFluxString,"\\n");
    write(forcefile, CoreFluxDensityString,"\\n");
105    write(forcefile, ToothFluxString,"\\n");
    write(forcefile, ToothFluxDensityString,"\\n");
    write(forcefile, FluxAo,"\\n");
    write(forcefile, FluxBo,"\\n");
    write(forcefile, FluxCo,"\\n");
110    write(forcefile, FluxAi,"\\n");
    write(forcefile, FluxBi,"\\n");
    write(forcefile, FluxCi,"\\n");
    closefile(forcefile);
    messagebox("Done");
115    --%%%%%%%%%%

```


Script A.8: Lua Function Definitions

```

1  --%%%%%%%%%%%%%%%%%%%%%%%%%%%%%%%%%%%%%%%%%%%%%%%%%%%%%%%%%%%%%%%%%%%%%%%%%%%%%%
-- Lua Simulation Functions: functions.lua
-- Author: Danson Michael Joseph
-- Modified: 24 November 2009
5  -----
-- Comments:
--     1) This is called by the simulation script, and
--     the post-processing script
--
10  --%%%%%%%%%%%%%%%%%%%%%%%%%%%%%%%%%%%%%%%%%%%%%%%%%%%%%%%%%%%%%%%%%%%%%%%%%%%%%%

--%%%%%%%%%%%%%%%%%%%%%%%%%%%%%%%%%%%%%%%%%%%%%%%%%%%%%%%%%%%%%%%%%%%%%%%%%%%%%%
-- Section 1: Build a Box
-----
15  function build_box(lt,rt,bt,tp,potential ,material ,mag ,xregion ,yregion ,
    mesh,meshsize ,group)
    -- Points -----
    mi_clearselected();
    mi_addnode(lt,bt);
    mi_addnode(rt,bt);
20  mi_addnode(lt,tp);
    mi_addnode(rt,tp);
    mi_selectnode(lt,bt);
    mi_selectnode(rt,bt);
    mi_selectnode(lt,tp);
25  mi_selectnode(rt,tp);
    mi_setnodeprop(potential ,group);

    -- Line Segments -----
    mi_clearselected();
30  mi_addsegment(lt,bt,lt,tp);
    mi_addsegment(lt,bt,rt,bt);
    mi_addsegment(rt,tp,lt,tp);
    mi_addsegment(rt,bt,rt,tp);
    mi_selectsegment(lt,bt+0.001*L);
35  mi_selectsegment(lt+0.001*lm,bt);
    mi_selectsegment(rt-0.001*lm,tp);
    mi_selectsegment(rt,tp-0.001*L);
    mi_setsegmentprop(potential ,0,1,0,group);

40  -- Region -----
    mi_clearselected();
    mi_addblocklabel(xregion ,yregion);
    mi_selectlabel(xregion ,yregion);
    mi_setblockprop(material ,mesh ,meshsize ," " ,mag ,group ,0);
45  end
--%%%%%%%%%%%%%%%%%%%%%%%%%%%%%%%%%%%%%%%%%%%%%%%%%%%%%%%%%%%%%%%%%%%%%%%%%%%%%%

--%%%%%%%%%%%%%%%%%%%%%%%%%%%%%%%%%%%%%%%%%%%%%%%%%%%%%%%%%%%%%%%%%%%%%%%%%%%%%%
-- Section 2: Build an Air-gap
-----
50  function build_airgap(tb,tt,sb,st,e1,e2,potential ,material ,mag ,xregion
    ,yregion ,mesh ,meshsize ,group)
    -- Points -----
    mi_clearselected();
    mi_addnode(e2,tb);
55  mi_addnode(e2,tt);
    mi_selectnode(e2,tb);
    mi_selectnode(e2,tt);
    mi_setnodeprop(potential ,group);

```

```

60  -- Line Segments -----
mi_clearselected();
mi_addsegment(e1,tb,e2,tb);
mi_addsegment(e2,tb,e2,sb);
mi_addsegment(e1,tt,e2,tt);
65  mi_addsegment(e2,tt,e2,st);

-- Region -----
mi_clearselected();
mi_addblocklabel(xregion,yregion);
70  mi_selectlabel(xregion,yregion);
mi_setblockprop(material,mesh,meshsize,"",mag,group,0);
end
--%%%%%%%%%%%%%%%%%%%%%%%%%%%%%%%%%%%%%%%%%%%%%%%%%%%%%%%%%%%%%%%%%%%%%%%%-----
75  --%%%%%%%%%%%%%%%%%%%%%%%%%%%%%%%%%%%%%%%%%%%%%%%%%%%%%%%%%%%%%%%%%%%%%%%%-----
-- Section 3: Build a Magnet -----

function build_magnet(n,left_start_mag)
-- Local Variables -----
80  bot = bottom_start_mag + Tp*n + maggap;
tp = bot + Tm;
x_middle = left_start_mag+lm/2;
mag_dir = mag_start + n*mag_rot;
right_end_mag = left_start_mag + lm;
85  while mag_dir < -360 do
    mag_dir = mag_dir + 360;
end
    build_box(left_start_mag,right_end_mag,bot,tp,"","Mag",mag_dir,
        x_middle,bot+Tm/2,mag_automesh,mag_meshsize,900)
end
90  --%%%%%%%%%%%%%%%%%%%%%%%%%%%%%%%%%%%%%%%%%%%%%%%%%%%%%%%%%%%%%%%%%%%%%%%%-----
--%%%%%%%%%%%%%%%%%%%%%%%%%%%%%%%%%%%%%%%%%%%%%%%%%%%%%%%%%%%%%%%%%%%%%%%%-----
-- Section 4: Build a Tooth -----

95  function build_tooth(bot,side,lsl,m)
-- Local Variables -----
    unit_width = Tp/12;
    end_point = side + lsl;
    lipp = 0.05;
100  lip = 0;

-- Points -----
mi_addnode(side,bot);
mi_addnode(end_point,bot+unit_width);
105  mi_addnode(end_point,bot+3*unit_width);
mi_addnode(side,bot+4*unit_width);
mi_addnode(side,bot+(1+lip)*unit_width);
mi_addnode(side,bot+(3-lip)*unit_width);
mi_addnode(side+lsl*lipp,bot+(1+lip)*unit_width);
110  mi_addnode(side+lsl*lipp,bot+(3-lip)*unit_width);
mi_addnode(side+lsl*lipp,bot+unit_width);
mi_addnode(side+lsl*lipp,bot+3*unit_width);

-- Line Segments -----
115  mi_addsegment(side,bot,side,bot+(1+lip)*unit_width);
mi_addsegment(side,bot+(3-lip)*unit_width,side,bot+4*unit_width);
mi_addsegment(end_point,bot+unit_width,side+lsl*lipp,bot+
    unit_width);

```

```

mi_addsegment(end_point, bot+3*unit_width, side+lsl*lipp, bot+3*
    unit_width);
mi_addsegment(end_point, bot+unit_width, end_point, bot+3*unit_width)
;
120 mi_addsegment(side, bot+3*unit_width, side, bot+unit_width);
mi_addsegment(side+lsl*lipp, bot+(3-lip)*unit_width, side, bot+(3-lip)
    )*unit_width);
mi_addsegment(side+lsl*lipp, bot+(1+lip)*unit_width, side, bot+(1+lip)
    )*unit_width);
mi_addsegment(side+lsl*lipp, bot+(1+lip)*unit_width, side+lsl*lipp,
    bot+unit_width);
mi_addsegment(side+lsl*lipp, bot+(3-lip)*unit_width, side+lsl*lipp,
    bot+3*unit_width);
125 end
--%%%%%%%%%%%%%%%%%%%%%%%%%%%%%%%%%%%%%%%%%%%%%%%%%%%%%%%%%%%%%%%%%%%%%%%%%%--
--%%%%%%%%%%%%%%%%%%%%%%%%%%%%%%%%%%%%%%%%%%%%%%%%%%%%%%%%%%%%%%%%%%%%%%%%%%--
-- Section 5: Set Current Values in the Circuits --
-----
130 function set_currents(i,o,n)
    mi_modifycircprop("Ai",1,i*Ii[n]);
    mi_modifycircprop("Bi",1,-i*Ii[n]/2);
    mi_modifycircprop("Ci",1,-i*Ii[n]/2);
135 mi_modifycircprop("Ao",1,o*Io[n]);
    mi_modifycircprop("Bo",1,-o*Io[n]/2);
    mi_modifycircprop("Co",1,-o*Io[n]/2);
end
--%%%%%%%%%%%%%%%%%%%%%%%%%%%%%%%%%%%%%%%%%%%%%%%%%%%%%%%%%%%%%%%%%%%%%%%%%%--
140 --%%%%%%%%%%%%%%%%%%%%%%%%%%%%%%%%%%%%%%%%%%%%%%%%%%%%%%%%%%%%%%%%%%%%%%%%%%--
-- Section 6: Build a Lamination --
-----
145 function build_lam(side, side2,lsl,circA,circB,circC)
    build_box(side,side2,bottom_start_lam,bottom_start_lam+L,"",steel
        ,0,side+(side2-side+lsl)/2,bottom_start_lam+L/2,
        stator_automesh,stator_meshsize,0)

    -- Set bottoms to group 222 -----
    mi_selectnode(side2,bottom_start_lam);
    mi_selectnode(side,bottom_start_lam);
150 mi_setnodeprop("",222);
    mi_clearselected();

    -- Set tops to group 333 -----
    mi_selectnode(side2,bottom_start_lam+L);
155 mi_selectnode(side,bottom_start_lam+L);
    mi_setnodeprop("",333);
    mi_clearselected();

    -- Build the Teeth -----
160 for m=0,3*L/Tp-1,1 do
        build_tooth(bottom_start_lam+m*Tp/3,side,lsl,m);
    end

    -- Add the Phases -----
165 xc1 = side+lsl/2;
    -- Phase A
    region_step = Tp/6;
    starts = bottom_start_lam + 5*region_step;
    N = Nc;
170 for m = 0,L/Tp-1,1 do

```


Script A.9: Simulation Input Parameter File: Double-Sided Tubular Machine

```

1  --%%%%%%%%%%%%%%%%%%%%%%%%%%%%%%%%%%%%%%%%%%%%%%%%%%%%%%%%%%%%%%%%%%%%%%%%%%%%%%
-- Parameters File: Full Scale Version: parameters.m
-- Author: Danson Michael Joseph
-- Modified: 24 November 2009
5  -----
-- Comments: This is called by the DST simulation and
--           post-processing scripts
--           -----
10  --%%%%%%%%%%%%%%%%%%%%%%%%%%%%%%%%%%%%%%%%%%%%%%%%%%%%%%%%%%%%%%%%%%%%%%%%%%%%%%
-- Section 1: Simulation Parameters
-----
mag_automesh=0;
15 mag_meshsize=4.0;
core_automesh=1;
core_meshsize=0;
stator_automesh=1;
stator_meshsize=0;
20 air_automesh=1;
air_meshsize=0;
airgap_automesh=0;
airgap_meshsize=1.5;
coils_automesh=0;
25 coils_meshsize=5;
support_automesh=1;
support_meshsize=0;
steel="US Steel Type 2-S 0.024 inch thickness";
steps = 20;
30 periods = 4;
simfrequency = 0;
simunits = "millimeters";
simtype = "axi";
simprecision = 1E-8;
35 simdepth = 0;
simminangle = 30;
--%%%%%%%%%%%%%%%%%%%%%%%%%%%%%%%%%%%%%%%%%%%%%%%%%%%%%%%%%%%%%%%%%%%%%%%%%%%%%%
-- Section 2: Mechanical Parameters
-----
40 ro = 305.6;
ri = 283;
lg = 5;
45 am = 0.8;
Tp = 100;
L = 5000;
p = L/Tp;
lsi = 81.6;
50 lso = 68.3;
lsli = 49.8;
lslo = 49.7;
lci = lsi - lsli;
lco = lso - lslo;
55 no_magnets = L/Tp+2*periods;
Lmag = no_magnets*Tp;
--%%%%%%%%%%%%%%%%%%%%%%%%%%%%%%%%%%%%%%%%%%%%%%%%%%%%%%%%%%%%%%%%%%%%%%%%%%%%%%
-- Section 3: Electrical Parameters
-----
60

```


Script A.10: Simulation Input Parameter File: AWS Machine

```

1  --%%%%%%%%%%%%%%%%%%%%%%%%%%%%%%%%%%%%%%%%%%%%%%%%%%%%%%%%%%%%%%%%%%%%%%%%%%%%%%
-- Parameters File: AWS Machine Version: parameters.aws.m
-- Author: Danson Michael Joseph
-- Modified: 24 November 2009
5  -----
-- Comments: This is called by the AWS simulation and
--           post-processing scripts
--           -----
10  --%%%%%%%%%%%%%%%%%%%%%%%%%%%%%%%%%%%%%%%%%%%%%%%%%%%%%%%%%%%%%%%%%%%%%%%%%%%%%%
-- Section 1: Simulation Parameters
-----
mag_automesh=0;
15 mag_meshsize=3.0;
core_automesh=1;
core_meshsize=1;
stator_automesh=1;
stator_meshsize=0;
20 air_automesh=1;
air_meshsize=1.5;
airgap_automesh=0;
airgap_meshsize=2.0;
coils_automesh=0;
25 coils_meshsize=5;
support_automesh=1;
support_meshsize=0;
steel="US Steel Type 2-S 0.024 inch thickness";
steps = 20;
30 periods = 4;
simfrequency = 0;
simunits = "millimeters";
simtype = "planar";
simprecision = 1E-8;
35 simdepth = 1000;
simminangle = 30;
--%%%%%%%%%%%%%%%%%%%%%%%%%%%%%%%%%%%%%%%%%%%%%%%%%%%%%%%%%%%%%%%%%%%%%%%%%%%%%%
-- Section 2: Mechanical Parameters
40 -----
lg = 5;
lm = 15;
hx = 30;
45 lsl = 100;
am = 0.8;
Tp = 100;
L = 5000;
p = L/Tp;
50 pp = p/2;
no_magnets = L/Tp+2*periods;
Lmag = no_magnets*Tp;
--%%%%%%%%%%%%%%%%%%%%%%%%%%%%%%%%%%%%%%%%%%%%%%%%%%%%%%%%%%%%%%%%%%%%%%%%%%%%%%
55  --%%%%%%%%%%%%%%%%%%%%%%%%%%%%%%%%%%%%%%%%%%%%%%%%%%%%%%%%%%%%%%%%%%%%%%%%%%%%%%
-- Section 3: Electrical Parameters
-----
J = 4*10^6;
Kfill = 0.585;
60 Nc = 100;

```


A.3 Octave Data Analysis & Signal Processing

Script A.11: Processing of Prototype Measurements

```

1  %%%%%%%%%%%%%%%%%%%%%%%%%%%%%%%%%%%%%%%%%%%%%%%%%%%%%%%%%%%
% Processing of Prototype Measurement Data: prototype.m           %
% Author: Danson Michael Joseph                                  %
% Modified: 12 August 2009                                       %
5  %-----%
% Comments: 0%    Tests = T1, T10, T17                            %
%             25%   Tests = T2, T3                               %
%             50%   Tests = T4, T5, T15, T16                     %
%             75%   Tests = T6, T7, T13, T14                     %
10 %             100% Tests = T8, T9, T11, T12                     %
%                                                                 %
%%%%%%%%%%%%%%%%%%%%%%%%%%%%%%%%%%%%%%%%%%%%%%%%%%%%%%%%%%%
15 % Section 0: Load Common Software Tools                          %
%-----%
addpath("../Software/Octave/");                                  %
addpath("../Software/Octave/g_xyz");                            %
%                                                                 %
20 %%%%%%%%%%%%%%%%%%%%%%%%%%%%%%%%%%%%%%%%%%%%%%%%%%%%%%%%%%%
% Section 1: Load Test Readings from File & Interpolate          %
%-----%
25 load -force readings.octave;    % Test Readings                %
load -force simulations.octave;   % FEA Simulated Forces         %
load -force calculations.octave; % Calculated Forces            %
%                                                                 %
%%%%%%%%%%%%%%%%%%%%%%%%%%%%%%%%%%%%%%%%%%%%%%%%%%%%%%%%%%%
30 % Section 2: Auxiliary Variables                                %
%-----%
% Points for Interpolation of the test readings -----%
35 posstep = 0.01;                                                %
posstart = 26;                                                    %
posend = 50;                                                      %
posi = [posstart:posstep:posend]; % Interpolation positions      %
points = [1:length(posi)];    % Points as numbers                %
40 %                                                                 %
% Generate Interpolated Data -----%
T1i=interp1(T1(1,:),T1(2,:),posi,"pchip",0);                    %
T2i=interp1(T2(1,:),T2(2,:),posi,"pchip",0);                    %
T3i=interp1(T3(1,:),T3(2,:),posi,"pchip",0);                    %
45 T4i=interp1(T4(1,:),T4(2,:),posi,"pchip",0);                    %
T5i=interp1(T5(1,:),T5(2,:),posi,"pchip",0);                    %
T6i=interp1(T6(1,:),T6(2,:),posi,"pchip",0);                    %
T7i=interp1(T7(1,:),T7(2,:),posi,"pchip",0);                    %
T8i=interp1(T8(1,:),T8(2,:),posi,"pchip",0);                    %
50 T9i=interp1(T9(1,:),T9(2,:),posi,"pchip",0);                    %
T10i=interp1(T10(1,:),T10(2,:),posi,"pchip",0);                 %
T11i=interp1(T11(1,:),T11(2,:),posi,"pchip",0);                 %
T12i=interp1(T12(1,:),T12(2,:),posi,"pchip",0);                 %
T13i=interp1(T13(1,:),T13(2,:),posi,"pchip",0);                 %
55 T14i=interp1(T14(1,:),T14(2,:),posi,"pchip",0);                 %
T15i=interp1(T15(1,:),T15(2,:),posi,"pchip",0);                 %
T16i=interp1(T16(1,:),T16(2,:),posi,"pchip",0);                 %

```

```

%
% Harmonic Analysis Variables -----%
60 harms = 20; % Number of harmonics %
dcharmonics = [0:1:harms]; % Harmonic orders %
harmonics = [0:1:harms-1]; % Harmonic orders, excl. DC %
emharmonics = [1 5 7 11 13 17 19]; % 2mk+-1 Electromagnetic harmonics%
%
65 %%%%%%%%%%%%%%%%%%%%%%%%%%%%%%%%%%%%%%%%%%%%%%%%%%%%%%%%%%%%%%%
% Section 3: Generate Stched Sample for Unexcited Tests %
%-----%
70 % Analyse the Unexcited System -----%
pstart.UE = 451; % Start position of a period %
pend.UE = 1650; % End position of a period %
UEi = [T1i;T10i]; % All unexcited measurements %
UEc = zeros(rows(UEi),harms+1); % Template matrix %
75 UE = UEi(1,:); % Select the first waveform %
for i = 2:rows(UEi) % Analyse each test run %
    UE = correlatedMean(UE,UEi(i,:)); % Correlate the readings %
endfor %
UEp = UE(pstart.UE:pend.UE); % Select a representative period %
80 UEf = subfilter(UEp); % Remove the subharmonic offset %
UEc = 2*abs(fourier(UEf,dcharmonics,length(UEf),1));% Harmonics calcs%
%
% Calculate the Non-Electro-magnetic force components -----%
weight = UEc(1); % Weight and constant friction %
85 reluctance = UEc(3); % End-effects reluctance force %
cogging = UEc(7); % Slot cogging %
%
% Section 4: Generate Stched Sample for the Excited Tests %
%-----%
90 % 100% Force Production %
pstart.E100 = 1296; % Start position of a period %
95 pend.E100 = 1895; % End position of a period %
E100p = correlatedMean(T8i,T9i);% Correlate two +DC readings %
E100n = correlatedMean(T11i,T12i); % Correlate two -DC readings %
E100 = correlatedMean(E100n,E100p);% Correlate +DC and -DC plots %
E100 = (E100-weight).*((E100-weight)>0); % Remove weight %
100 E100 = E100(pstart.E100:pend.E100); % Select one positive half-wave %
E100c = 2*abs(imag(fourier(E100,emharmonics,1200,4))); %Odd Fourier %
%
% 75% Force Production %
pstart.E75 = 1301; % Start position of a period %
105 pend.E75 = 1900; % End position of a period %
E75p = correlatedMean(T6i,T7i); % Correlate two +DC readings %
E75n = correlatedMean(T13i,T14i); % Correlate two -DC readings %
E75 = correlatedMean(E75n,E75p);% Correlate +DC and -DC plots %
E75 = (E75-weight).*((E75-weight)>0); % Remove weight %
110 E75 = E75(pstart.E75:pend.E75); % Select one positive half-wave %
E75c = 2*abs(imag(fourier(E75,emharmonics,1200,4))); %Odd Fourier %
%
% 50% Force Production %
pstart.E50 = 1409; % Start position of a period %
115 pend.E50 = 2008; % End position of a period %
E50p = correlatedMean(T4i,T5i); % Correlate two +DC readings %
E50n = correlatedMean(T15i,T16i); % Correlate two -DC readings %
E50 = correlatedMean(E50n,E50p);% Correlate +DC and -DC plots %

```

```

120 E50 = (E50-weight).*((E50-weight)>0); % Remove weight %
E50 = E50(pstart.E50:pend.E50); % Select one positive half-wave %
E50c = 2*abs(imag(fourier(E50,emharmonics,1200,4))); %Odd Fourier %
% %
% 25% Force Production %
125 pstart.E25 = 1277; % Start position of a period %
pend.E25 = 1876; % End position of a period %
E25 = correlatedMean(T2i,T3i); % Correlate +DC readings %
E25 = (E25-weight).*((E25-weight)>0); % Remove weight %
E25 = E25(pstart.E25:pend.E25); % Select one positive half-wave %
E25c = 2*abs(imag(fourier(E25,emharmonics,1200,4))); %Odd Fourier %
130 %%%%%%%%%%%%%%%%%%%%%%%%%%%%%%%%%%%%%%%%%%%%%%%%%%%%%%%%%%%%%%%%%%%%%%%%%%%
%%%%%%%%%%%%%%%%%%%%%%%%%%%%%%%%%%%%%%%%%%%%%%%%%%%%%%%%%%%%%%%%%%%%%%%%%%
% Section 5: Generate Plots on Screen and to File %
%-----%
135 % Plot the Unexcited System to Screen -----%
UEPlot = figure(); % A new figure %
subplot(2,1,1); % Plot the pattern %
plot(posi(pstart.UE:pend.UE),UEf);% %
subplot(2,1,2); % Plot the harmonics %
140 stem(dcharmonics,UEc); % %
axis([-1,harms,0,1200]); % Label the harmonic orders %
% %
% Plot the Unexcited System to File -----%
x = [1:length(UE)]; % X-axis %
145 saveplot((x/4)',(UE/1000)', "Test_UE_Pattern.table"); %
saveplot(dcharmonics',(UEc/1000)', "Test_UE_Harmonics.table"); %
% %
% Plot the Excited Systems to Screen -----%
EPlot = figure(); % A new figure %
150 subplot(5,1,1); % Plot the Pattern %
hold on; %
plot(posi(pstart.E100:pend.E100),E100); %
plot(posi(pstart.E75:pend.E75),E75); %
plot(posi(pstart.E50:pend.E50),E50); %
155 plot(posi(pstart.E25:pend.E25),E25); %
hold off; %
subplot(5,1,2); % Plot the pattern %
stem(harmonics,E100c); %
axis([0,harms,0,3000]); % Label the harmonic orders %
160 subplot(5,1,3); % Plot the pattern %
stem(harmonics,E75c); %
axis([0,harms,0,2500]); % Label the harmonic orders %
subplot(5,1,4); % Plot the pattern %
stem(harmonics,E50c); %
165 axis([0,harms,0,2000]); % Label the harmonic orders %
subplot(5,1,5); % Plot the pattern %
stem(harmonics,E25c); %
axis([0,harms,0,1500]); % Label the harmonic orders %
% %
170 % Plot the Excited Systems to File -----%
x = [1:length(E100)]; % X-axis %
saveplot((x/4)',(E100/1000)', "Test_E100_Pattern.table"); %
saveplot(harmonics',(E100c/1000)', "Test_E100_Harmonics.table"); %
x = [1:length(E75)]; % X-axis %
175 saveplot((x/4)',(E75/1000)', "Test_E75_Pattern.table"); %
saveplot(harmonics',(E75c/1000)', "Test_E75_Harmonics.table"); %
x = [1:length(E50)]; % X-axis %
saveplot((x/4)',(E50/1000)', "Test_E50_Pattern.table"); %
saveplot(harmonics',(E50c/1000)', "Test_E50_Harmonics.table"); %

```


Script A.17: Pattern Averaging and Correlation

```

1 %%%%%%%%%%%%%%%%%%%%%%%%%%%%%%%%%%%%%%%%%%%%%%%%%%%%%%%%%%%%%%%%%%%%%%%%%%%
% Get the Mean of Correlated Signals: correlatedMean.m
% Author: Danson Michael Joseph
% Modified: 14 August 2009
5 %-----%
% Comments:
%
%%%%%%%%%%%%%%%%%%%%%%%%%%%%%%%%%%%%%%%%%%%%%%%%%%%%%%%%%%%%%%%%%%%%%%%%%%
%
10 function y = correlatedMean(xi,yi)
    [a,b,R,lag] = correlate(xi,yi);
    y = (a+b)/2;
endfunction
%
15 %%%%%%%%%%%%%%%%%%%%%%%%%%%%%%%%%%%%%%%%%%%%%%%%%%%%%%%%%%%%%%%%%%%%%%%%%%%

```

Conclusions

The three different programming environments were uniquely suited to their respective tasks. The evaluation of complex symbolic equations in the design and performance calculation scripts was best achieved with the Mathematica engine.

The integration of Lua into FEMM made it the natural choice for simulation and data extraction. FEMM includes custom Lua functions which made the simulation setup and post-processing relatively simple and very effective.

Octave, being a comprehensive numerical mathematics package, was best suited to the numerical analysis of the resulting data sets. It is a matrix algebra environment by nature and so the analysis of large matrices of data was achieved with a high degree of confidence in the output results.

Appendix B

Solution to Laplace's Equation in Cylindrical Coordinates

***Introduction:** The determination of the magnetic flux in the air-gap, resulting from the stator windings, is achieved through the quantification of the magnetic vector potential in the air-gap. The magnetic vector potential, \vec{A} , is defined as the vector field whose curl is equal to the magnetic flux density field, \vec{B} , according to $\vec{B} = \nabla \times \vec{A}$. The definition of \vec{A} is found as the solution to Laplace's equation $\nabla^2 \vec{A} = 0$. The subtle difference between the following derivation and those in the literature is that this considers the solution to Laplace's equation in the polar-cylindrical coordinate space. The derivation to follow results in a definition of two general solutions to Laplace's equation in cylindrical coordinates, applicable to tubular linear machines. The methods used in this derivation are present in most mathematical reference books[44].*

Laplace's equation in cylindrical coordinates is defined in Equation B.1. The magnetic vector potential only has a component in the ϕ direction, A_ϕ , due to the symmetry of B in the ϕ dimension. The solution to Laplace's equation may be found by applying the method of separation of variables such that A_ϕ is represented as in Equation B.2.

$$\nabla^2 \vec{A} = \frac{1}{r} \frac{\partial}{\partial r} \left(r \frac{\partial \vec{A}}{\partial r} \right) + \frac{1}{r^2} \frac{\partial^2 \vec{A}}{\partial \phi^2} + \frac{\partial^2 \vec{A}}{\partial z^2} = 0 \quad (\text{B.1})$$

$$A_\phi(r, \phi, z) = R(r) \times \Phi(\phi) \times Z(z) \quad (\text{B.2})$$

Each separate function, R , Φ and Z is considered constant to the partial differentials with respect to the coordinates of which it is not a function. We may pull them through the partial differentials, multiply by $r^2/R(r)\Phi(\phi)Z(z)$, and represent the Laplace equation as in Equation B.3. Notice that the derivatives are no longer partial differentials.

$$\frac{r}{R(r)} \frac{d}{dr} \left(r \frac{dR(r)}{dr} \right) + \frac{1}{\Phi(\phi)} \frac{d^2 \Phi(\phi)}{d\phi^2} + \frac{r^2}{Z(z)} \frac{d^2 Z(z)}{dz^2} = 0 \quad (\text{B.3})$$

Rearranging the equation results in Equation B.4. The variables r , ϕ and z are independent variables. Therefore the equation can only be true if λ is a constant for all values of r , ϕ and z .

$$\frac{r}{R(r)} \frac{d}{dr} \left(r \frac{dR(r)}{dr} \right) + \frac{r^2}{Z(z)} \frac{d^2 Z(z)}{dz^2} = -\frac{1}{\Phi(\phi)} \frac{d^2 \Phi(\phi)}{d\phi^2} = \lambda \quad (\text{B.4})$$

We consider firstly only the azimuthal component of this equation as represented in Equation B.5. One possible general solution to this equation is presented in Equation B.6. This represents complex roots to the equation which indicates oscillatory behaviour and requires $\lambda = +n^2$. A second possible general solution to this equation is shown in Equation B.7. This represents real roots to the equation, indicating an exponentially decaying behaviour, and requiring $\lambda = -n^2$. Both solutions exclude the proportionality constant which will be introduced in the final definition of A_ϕ .

$$\begin{aligned} -\frac{1}{\Phi(\phi)} \frac{d^2 \Phi(\phi)}{d\phi^2} &= \lambda = \pm n^2 \\ \frac{d^2 \Phi(\phi)}{d\phi^2} \pm n^2 \Phi(\phi) &= 0 \end{aligned} \quad (\text{B.5})$$

$$\text{Complex Roots : } \Phi(\phi) \propto e^{\pm jn\phi} \quad (\text{B.6})$$

$$\text{Real Roots : } \Phi(\phi) \propto e^{\pm n\phi} \quad (\text{B.7})$$

Consider next the separation of the axial solution $Z(z)$. Equation B.4 may be rearranged and divided by r^2 to produce Equation B.8. The axial equation alone is represented in Equation B.9. Following the same logic as for the azimuthal solutions, two possible general solutions which satisfy the axial equation are given in Equations B.10 and B.11 for complex and real roots to the equation respectively.

$$\frac{1}{rR(r)} \frac{d}{dr} \left(r \frac{dR(r)}{dr} \right) - \frac{\lambda}{r^2} = -\frac{1}{Z(z)} \frac{d^2 Z(z)}{dz^2} = \kappa = \pm k^2 \quad (\text{B.8})$$

$$\begin{aligned} -\frac{1}{Z(z)} \frac{d^2 Z(z)}{dz^2} &= \kappa = \pm k^2 \\ \frac{d^2 Z(z)}{dz^2} \pm k^2 Z(z) &= 0 \end{aligned} \quad (\text{B.9})$$

$$\text{Complex Roots : } Z(z) \propto e^{\pm jkz} \quad (\text{B.10})$$

$$\text{Real Roots : } Z(z) \propto e^{\pm kz} \quad (\text{B.11})$$

We do not want to consider all possible radial solutions for all combinations of real and complex solutions to the axial and azimuthal equations. For now we will consider the limitations on these solutions in a tubular linear machine. The axial symmetry of the machine means that \vec{A} does not vary with ϕ . Therefore $\Phi(\phi)$ is a constant and the double-derivative thereof is equal to zero. This means that $n = 0$. We will maintain the variable n , but represent λ as n^2 which equals zero. The three-phase winding of stator coils which develops this magnetic vector potential \vec{A} is oscillatory in z . Therefore the complex solution to the axial equation is applicable such that $\kappa = k^2$.

Finally we consider the radial solution which is the most complex of the general solutions. After multiplying Equation B.8 by r^2 , we arrive at the radial equation, as presented in Equation B.12. Using a substitution of $u = kr$ we may simplify this equation to arrive at Equation B.13.

$$0 = r \frac{d}{dr} \left(r \frac{dR(r)}{dr} \right) - (k^2 r^2 + n^2) R(r) \quad (\text{B.12})$$

$$\text{let } u = kr$$

$$\therefore \frac{d}{dr} = k \frac{d}{du}$$

$$0 = u^2 \frac{d^2 R(u)}{du^2} + u \frac{dR(u)}{du} - (u^2 + n^2) R(u) \quad (\text{B.13})$$

The general solutions to Equation B.13 are the modified Bessel functions of the first and second kind, $I_n(u)$ and $K_n(u)$ respectively. Thus the general solutions may be in the form of Equations B.14 and B.15.

$$R(kr) \propto I_n(kr) \quad (\text{B.14})$$

$$R(kr) \propto K_n(kr) \quad (\text{B.15})$$

Before combining the three individual functions, $\Phi(\phi)$, $R(r)$ and $Z(z)$ to form the general solution to A_ϕ , the definitions of n and k may be interpreted more appropriately for the application of a linear tubular machine. It has already been discussed that $n = 0$ because of the axial symmetry of the machine.

However, k may also have a representation which is more appropriate. Remembering that the axial solution is periodic in z according to kz , k may be interpreted as $h\beta$, the ratio of π to the harmonic pole-pitch τ_p/h . Therefore we may replace all instances of k with $h\beta$. Equation B.2 may now be strung together from the individual functions to form the general solutions to $A_{\phi h}$ as presented in Equations B.16 and B.17 depending on the phase of the armature line current density.

$$A_{\phi h}(r, \phi, z) = R(r) \times \Phi(\phi) \times Z(z)$$

$$A_{\phi h}(r, z) = [A'_h I_0(h\beta r) + B'_h K_0(h\beta r)] [e^{jh\beta z} \pm e^{-jh\beta z}]$$

$$A_{\phi h}(r, z) = \sin(h\beta z) \{A_h I_0(h\beta r) + B_h K_0(h\beta r)\} \quad (\text{B.16})$$

$$\text{or : } A_{\phi h}(r, z) = \cos(h\beta z) \{A_h I_0(h\beta r) + B_h K_0(h\beta r)\} \quad (\text{B.17})$$

Conclusions

The stator windings develop a magnetic flux density in the air-gap which has components in r and z , but not in ϕ . Therefore the magnetic vector potential, \vec{A} is only defined in the ϕ dimension such that its *curl* may define the magnetic flux density according to $B = \nabla \times \vec{A}$.

Two general solutions are derived for Laplace's equation in cylindrical coordinates, $\nabla^2 \vec{A} = 0$. These solutions are peculiar to a tubular linear machine with the periodicity in z caused by the periodicity of the armature windings. The only difference between the two general solutions is the phase displacement in the z dimension which should be aligned to the phase of the armature line current density.

Appendix C

Prototype Construction

***Introduction:** A prototype of a Double-Sided Permanent-Magnet Linear Synchronous Generator was designed, built and tested. The objective of the prototype construction was to validate the mathematical description of the machine through measurement. This chapter documents the design specifications and construction procedure. Section C.1 details the specifications of the machine including the Computer-Aided Design drawings. Section C.2 presents the details of the machine construction procedure.*

C.1 Specifications and Design

C.1.1 Specifications

The machine was designed using the mathematical model and methodology developed in this research. The design was then modified to suit the available materials, budget and mechanical constraints. The result was a sub-optimal design, but one suitable for the purposes of this research. The final machine specifications are given in Table C.1.

A limited number of suppliers were used during the project. Most components were sourced locally. Most of the steel-work was performed at Electrical Engineering Workshop at the University of the Witwatersrand. A list of the suppliers is given in Table C.2.

Table C.1: Specifications of the Prototype Machine

Parameter	Parameter Definition	Design Value
L	Stator Length	0.36 m
L_t	Translator Length	1.00 m
L_m	Magnet Array Length	0.60 m
τ_p	Pole-pitch	0.06 m
τ_m	Magnet-pitch	0.048 m
k_w	Winding Factor	1.0
q	Slots/pole/phase	1
r_o	Translator Outer radius	0.078 m
r_i	Translator Inner radius	0.073 m
l_m	Magnet length	5.0 mm
l_g	Air-gap length	4.5 mm
l_{si}	Inner Stator Length	0.0605 m
l_{so}	Outer Stator Length	0.0503 m
l_{ci}	Inner Core Length	0.0335 m
l_{co}	Outer Core Length	0.0140 m
Q_i	Inner Specific Electrical Loading	8 400 A/m
Q_o	Outer Specific Electrical Loading	14 000 A/m
J	Conductor Current Density	5 A/mm ²
\hat{B}_c	Peak Core Flux Density	1.5 T
\hat{B}_t	Peak Teeth Flux Density	1.8 T
T_{op}	Magnet Operating Temperature	25°C

Table C.2: Supplier Information

Part	Supplier	Address
Permanent-Magnets	Ningbo Ketian	No.1 Chengxi West Road,
	Magnet Co., Ltd.	Cicheng Town, Ningbo,
	Tel: +86 574 8757-4888	Zhejiang, China, 315034
	Fax: +86 574 8759-7123	http://www.kt-magnet.com

Table C.2: Supplier Information (Continued...)

Part	Supplier	Address
Laminations	Alstom SA (Pty) Ltd Tel: +27 11 820-5111 Fax: +27 11 820-5100	2 Magnet Road, Knights, Boksburg, South Africa, 1413 http://www.alstom.co.za
Stator Coils	Transvaal Electric (Pty) Ltd Tel: +27 11 493-6480/1 Fax: +27 11 493-2340	4 Simmonds St, Selby, Johannesburg, South Africa, 2001 http://www.transelectric.co.za
Outsourced Machining	SIMA Turners (Pty) Ltd Tel: +27 11 683-2373/4 Fax: +27 11 434-1825	46 Marlborough Road, Springfield, Johannesburg, South Africa, 2190 http://www.sima.co.za
Bearings	Bearing Man Group (Pty) Ltd Tel: +27 11 620-1500 Fax: +27 11 620-1660	3 Droste Crescent, Droste Park Ext. 7, South Africa http://www.bearingman.co.za
Threaded Rod	Bascol (Pty) Ltd Tel: +27 11 493-1669 Fax: +27 11 493-1206	2a John St, Selby Johannesburg, South Africa, 2001 http://www.bascol.co.za
Vesconite [®]	Vesco Plastics Sales (Pty) Ltd Tel: +27 11 616-1111 Fax: +27 11 616-2222	2 Watkins Street, Denver Johannesburg, South Africa http://www.vesconite.co.za

Table C.2: Supplier Information (Continued...)

Part	Supplier	Address
Tufnol [®]	Tufnol (Pty) Ltd Tel: +27 11 613-2683 Fax: +27 11 613-2693	City Deep Production Park, City Deep, Johannesburg, South Africa, 2001 http://www.vesconite.co.za
Laser Cutting	General Profiling (Pty) Ltd Tel: +27 11 839-2917 Fax: +27 11 837-1617	115 Industrial Rd, Amalgam, Johannesburg, South Africa, 2092 http://www.generalprofiling.co.za

The larger machined components were outsourced. The engineering works, SIMA Turners (Pty) Ltd., and laser cutting fabricators, General Profiling (Pty) Ltd., sourced the raw materials on the University's behalf. This simplified the procurement procedure.

Table C.3 lists the major components of the final machine. Excluded from the list are those components which were commonly found in the workshop such as small nuts and bolts. Parts which were machined for the project from raw materials are referred to in the Computer Aided Design drawings in Section C.1.2.

Table C.3: Bill of Materials for the Prototype Machine

Part #	Description	Quantity
SIMA-01	Top System Support Figure C.2	1
SIMA-02	Outer Stator Supports Figure C.3	2
SIMA-03	Outer Core OD × ID × L = 275.6 mm × 247.65 mm × 365 mm	1
SIMA-04	Bottom System Support Figure C.4	1
SIMA-05	Inner Stator Support Column OD × ID × L = 60 mm × 32 mm × 550 mm	1

Table C.3: Bill of Materials for the Prototype Machine (Continued...)

Part #	Description	Quantity
EIE-01	Bearing Sleeve for the 66/22-2RS1 Bearings Figure C.5	18
EIE-02	Inner Stator Upper Support Figure C.6	1
EIE-03	Inner Stator Lower Support Figure C.7	1
EIE-04	Inner Stator Core OD \times ID \times L = 73.02 mm \times 8 mm \times 370 mm	1
EIE-05	Inner Coils 0.9mm Copper Wire	15kg
EIE-06	M10 Threaded Rod x 1m	3
EIE-07	M10 Nuts	12
EIE-08	M12 Threaded Rod x 1m	1
EIE-09	M12 Nuts	12
EIE-10	M30 Female Lifting Eye	1
LC-01	Translator Top Plate OD \times ID \times L = 120 mm \times 30 mm \times 16 mm	1
LC-02	Top Support Bearing Assembly Base Figure C.8 a)	3
LC-03	Top Support Bearing Assembly Upright Figure C.8 b)	6
LC-04	Outer Stator Bearing Assembly Base Figure C.9 a)	6
LC-05	Outer Stator Bearing Assembly Upright Figure C.9 b)	12
LC-06	Inner Stator Bearing Assembly Base Figure C.10 a)	1
LC-07	Inner Stator Bearing Assembly Upright Figure C.10 b)	3
BM-01	Outer Stator Bearings: 66/22-2RS1	6
BM-02	Inner Stator Bearings: UC-201	3
BM-03	Top Support Bearings: 66/22-2RS1	3

Table C.3: Bill of Materials for the Prototype Machine (Continued...)

Part #	Description	Quantity
KTM-01	N42 Outer Magnet Arc $r_o \times r_i \times \phi \times l = 83 \text{ mm} \times 78 \text{ mm} \times 45^\circ \times 48 \text{ mm}$	80
KTM-02	N42 Inner Magnet Arc $r_o \times r_i \times \phi \times l = 73 \text{ mm} \times 68 \text{ mm} \times 45^\circ \times 48 \text{ mm}$	80
AST-01	Outer Lamination OD \times ID \times L = 247.65 mm \times 175 mm \times 0.5 mm	360
AST-02	Inner Lamination OD \times ID \times L = 127 mm \times 73.02 mm \times 0.5 mm	360
TVE-01	Outer Pre-fabricated Coils (14 Turns in 2 Layers) 4mm square glass-insulated copper wire	18
BC-01	M30 Galvanised Threaded Rod x 3m	6
BC-02	M30 Galvanised Nuts	50
VC-01	Translator Outer Vesconite Ring Figure C.11 a)	11
VC-02	Translator Inner Vesconite Ring Figure C.11 b)	11
TUF-01	Outer Magnet Tufnol Sleeve OD \times ID \times L = 171 mm \times 166 mm \times 38 mm	10
TUF-02	Inner Magnet Tufnol Sleeve OD \times ID \times L = 136 mm \times 131 mm \times 38 mm	10
TUF-03	Translator Outer Tufnol Sleeve OD \times ID \times L = 171 mm \times 156 mm \times 368 mm	1
TUF-04	Translator Inner Tufnol Sleeve OD \times ID \times L = 146 mm \times 131 mm \times 352 mm	1

C.1.2 Computer Aided Design

The complete 3D CAD representation of the machine is shown in Figure C.1 along-side a photograph of the machine as built.

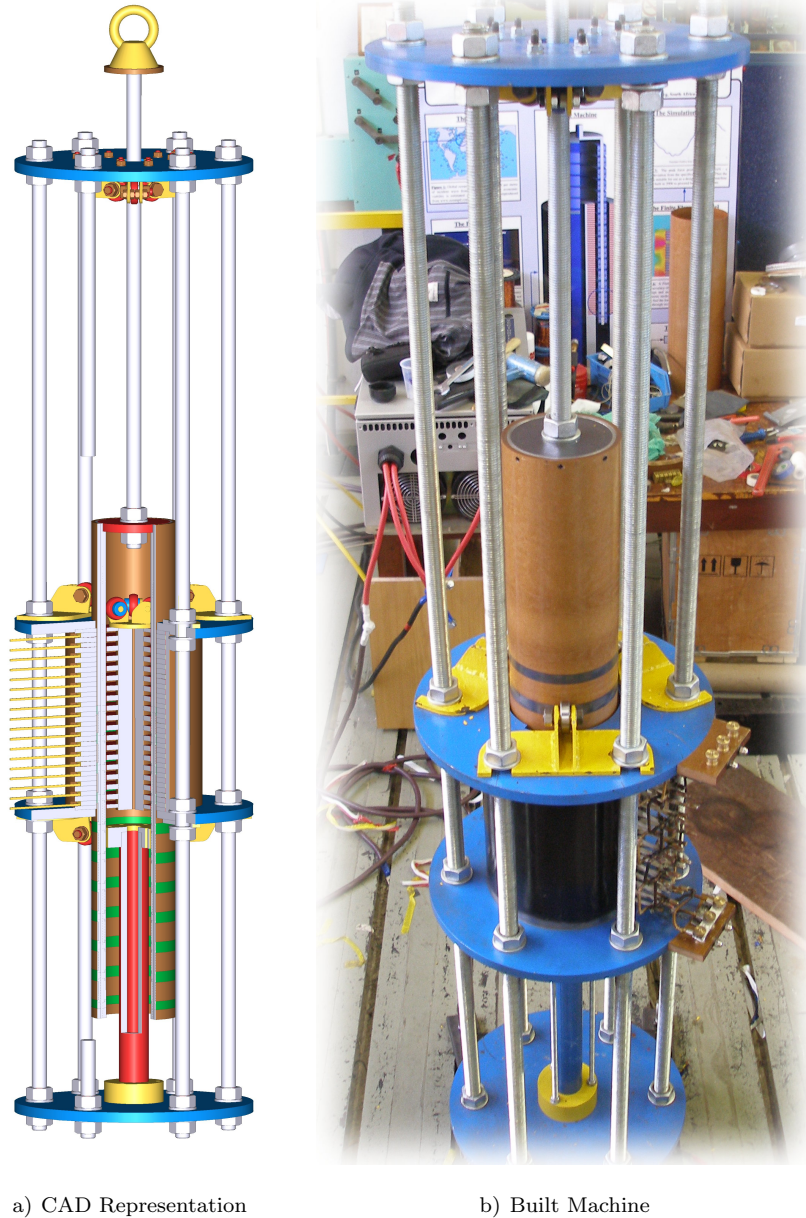


Figure C.1: 3D CAD Representation of the Prototype Machine and a Photograph of the Built Equivalent.

The mechanical drawings which follow specify the parts which were either machined or laser-cut for this project. Only parts which have not or cannot be expressed by simple dimensions of outer-diameter, inner-diameter and length are presented. All other components which may be expressed thus, are detailed accordingly in Table C.3.

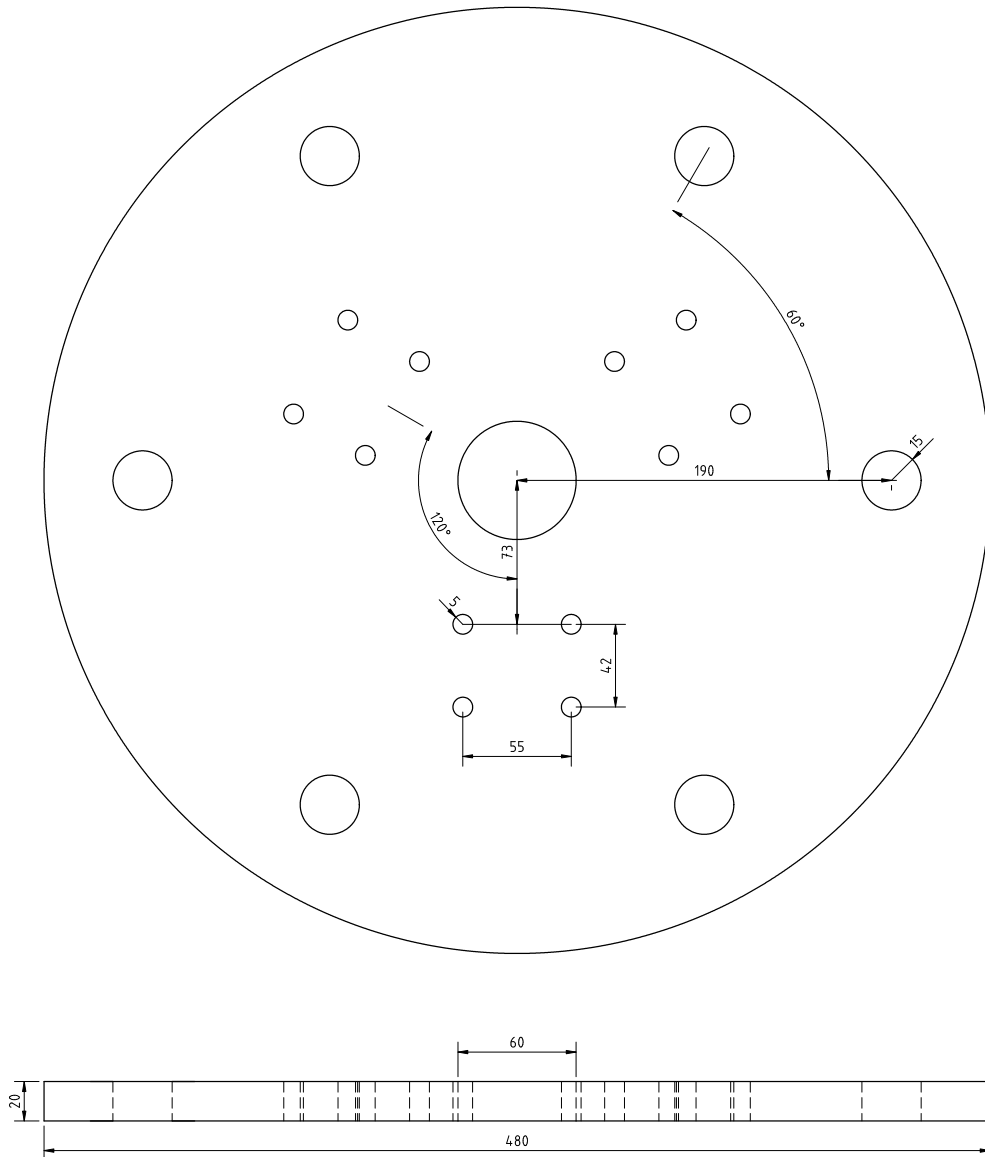


Figure C.2: Top System Support: SIMA-01

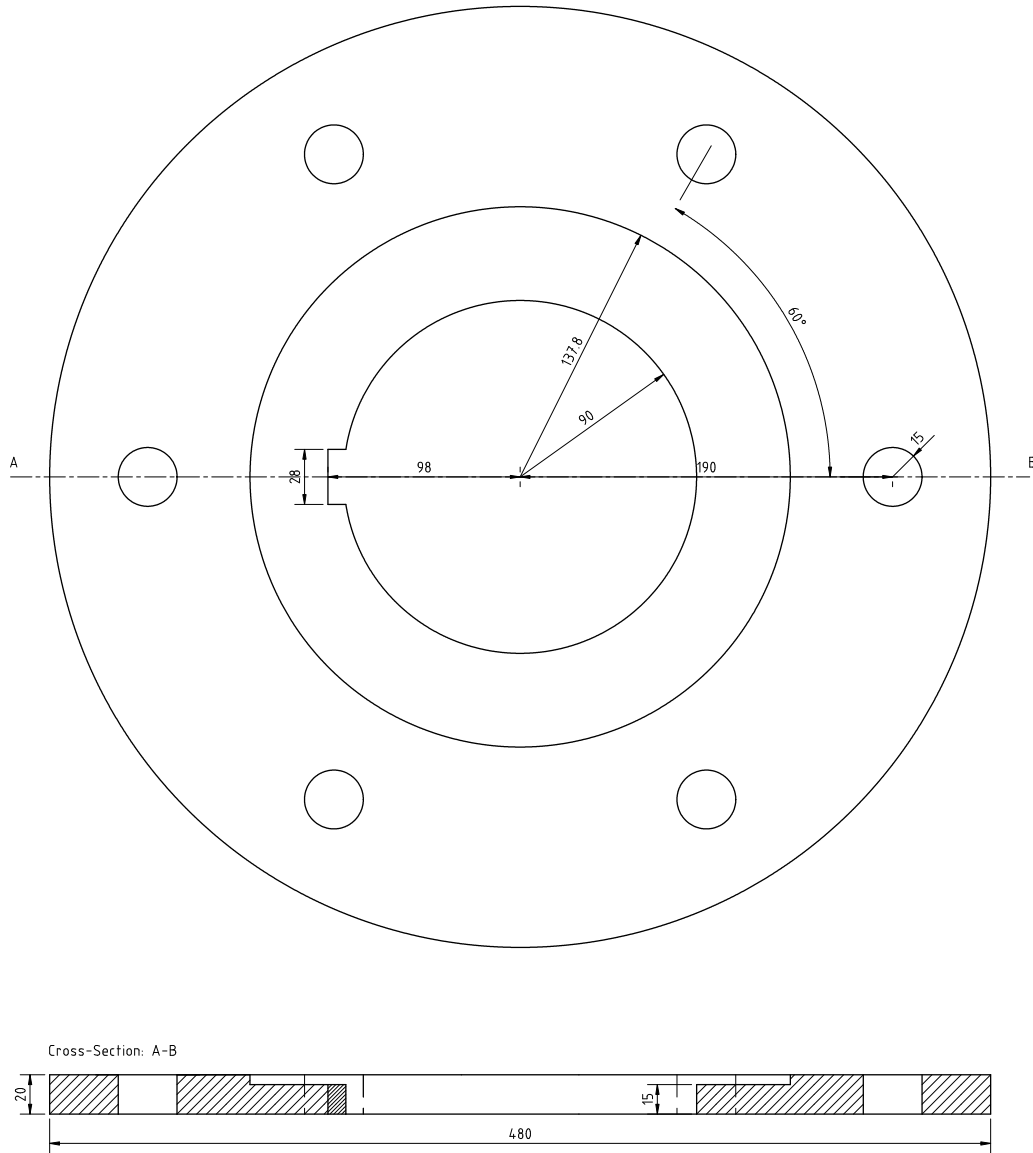


Figure C.3: Outer Stator Support: SIMA-02

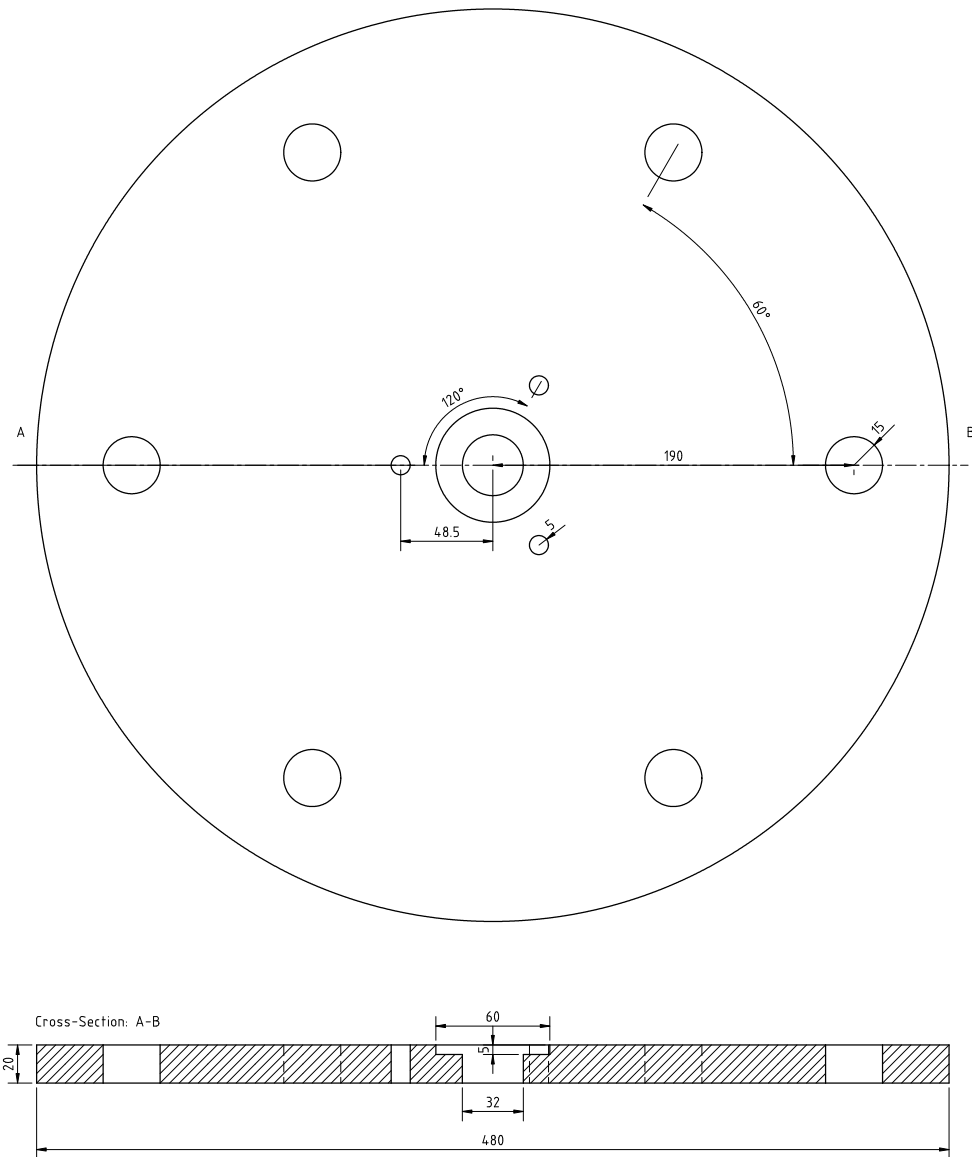


Figure C.4: Bottom System Support: SIMA-04

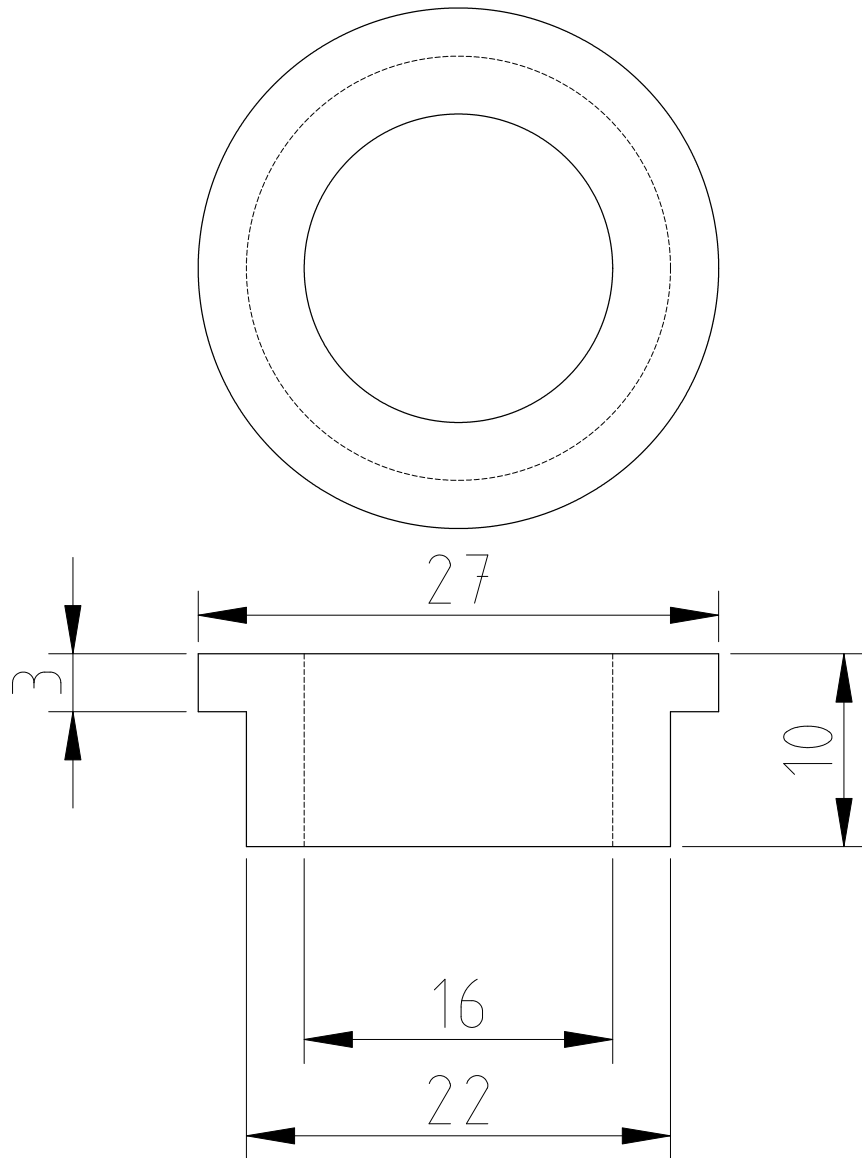
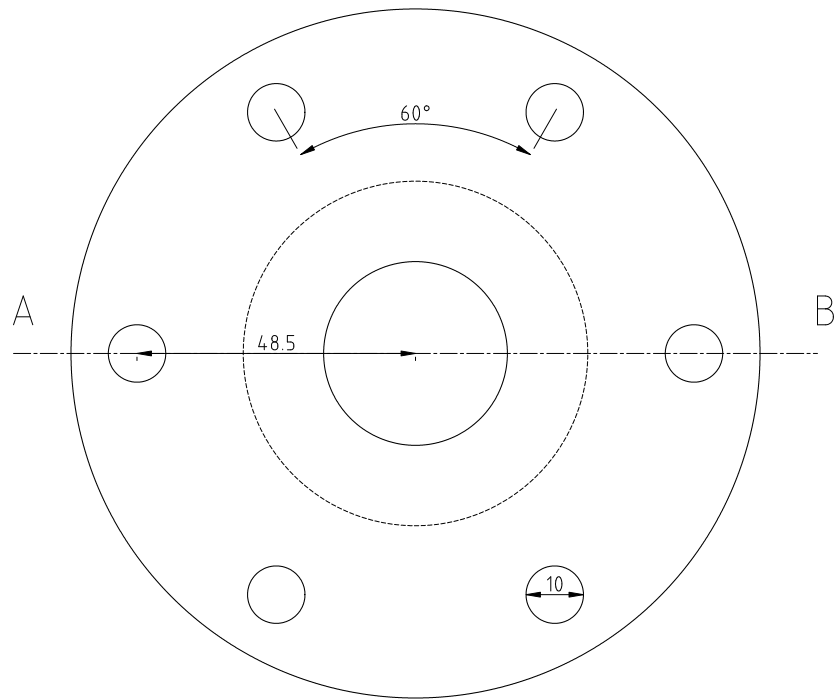


Figure C.5: Bearing Sleeve for the 66/22-2RS1 Bearings: EIE-01



Cross-Section: A-B

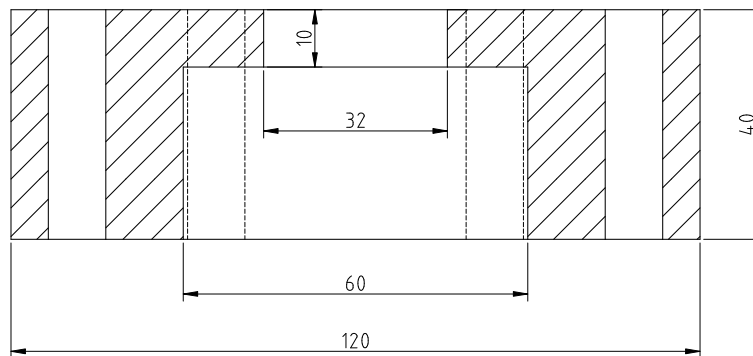
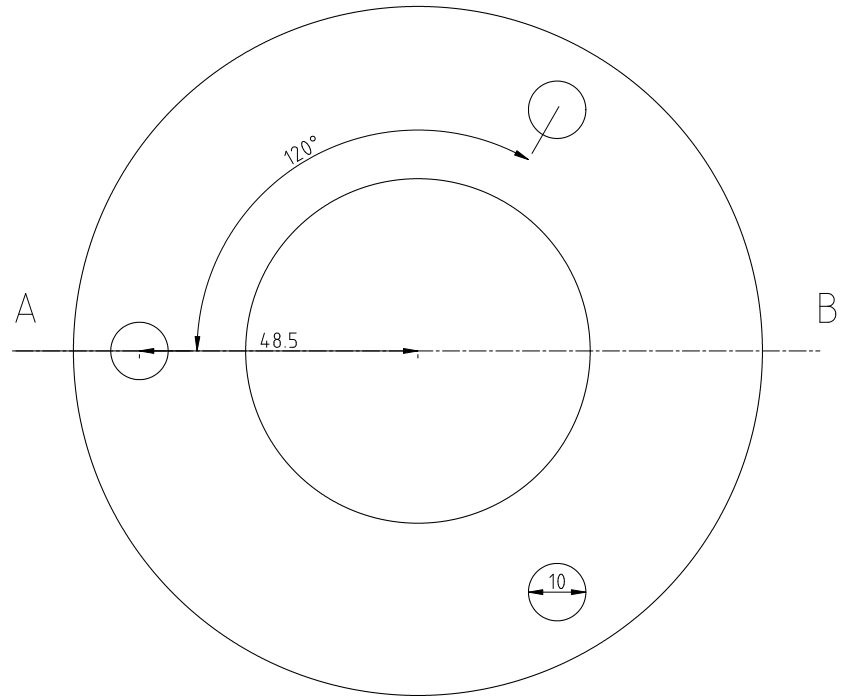


Figure C.6: Inner Stator Upper Support: EIE-02



Cross-Section: A-B

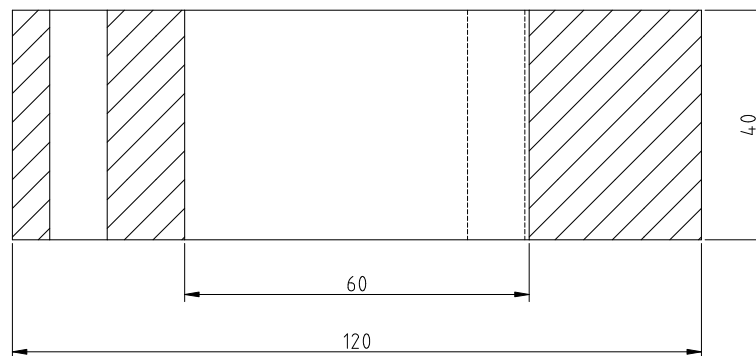
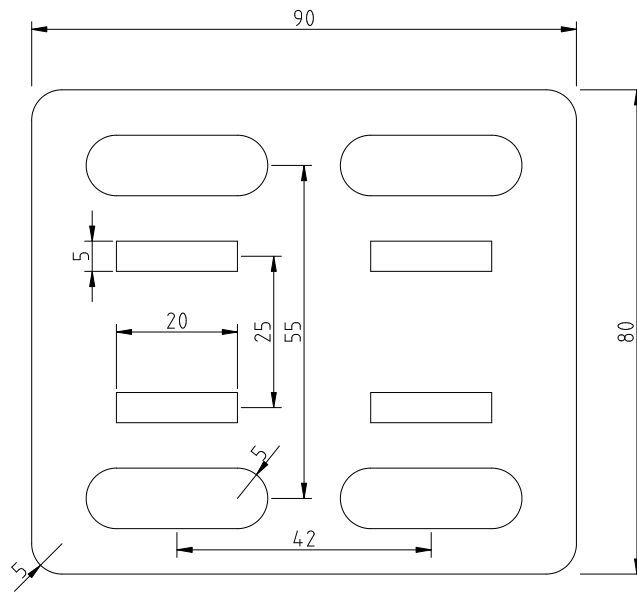
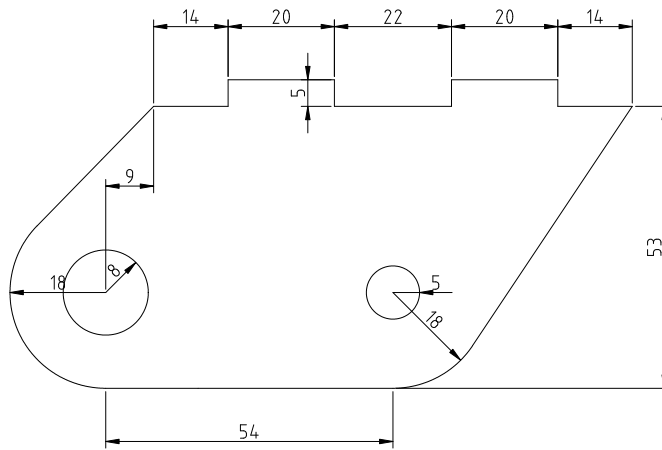


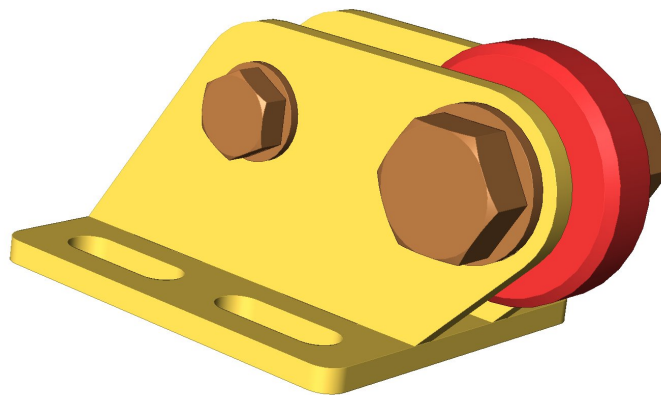
Figure C.7: Inner Stator Lower Support: EIE-03



a) LC-02: Assembly Base

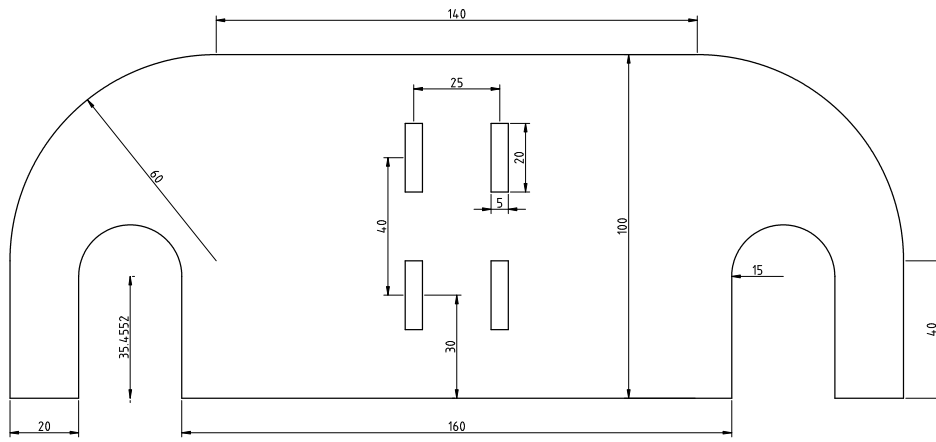


b) LC-03: Assembly Upright

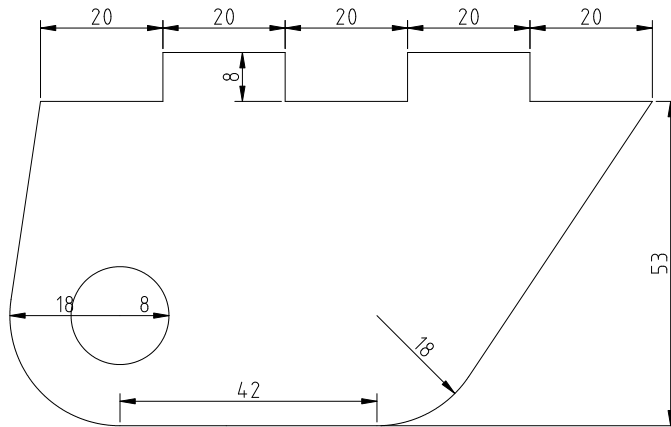


c) 3D CAD Representation of the Bearing Assembly

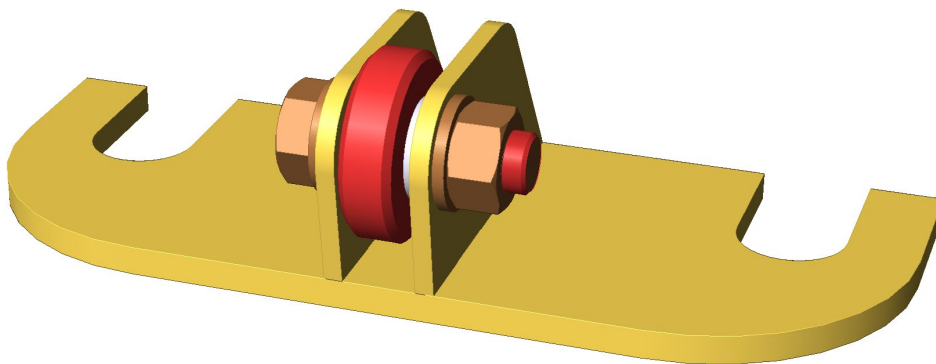
Figure C.8: Top Support Bearing Assembly: LC-02 and LC-03



a) LC-04: Assembly Base

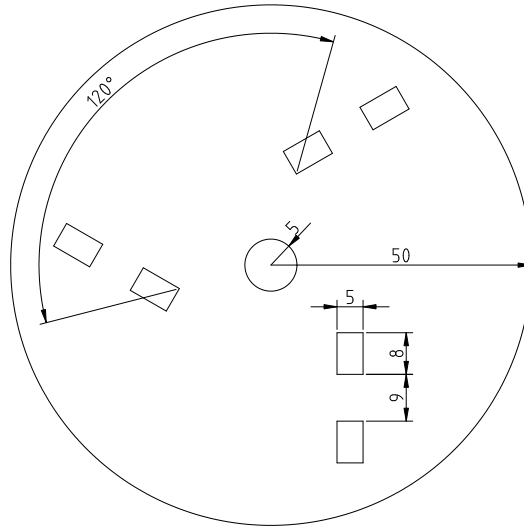


b) LC-05: Assembly Upright

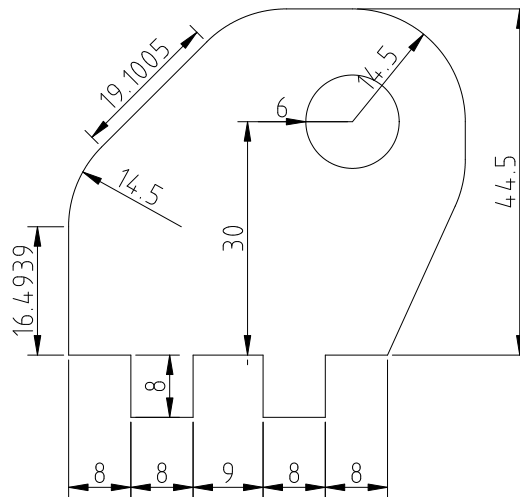


c) 3D CAD Representation of the Bearing Assembly

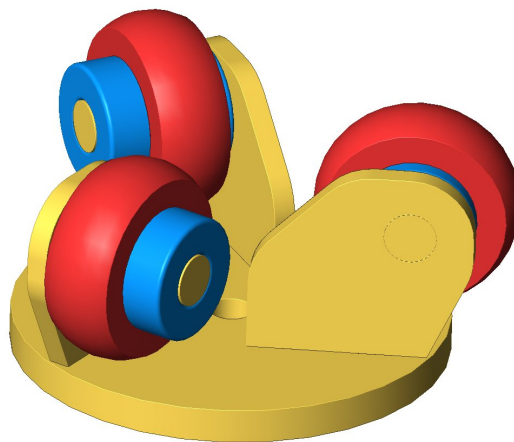
Figure C.9: Outer Stator Bearing Assembly: LC-04 and LC-05



a) LC-06: Assembly Base

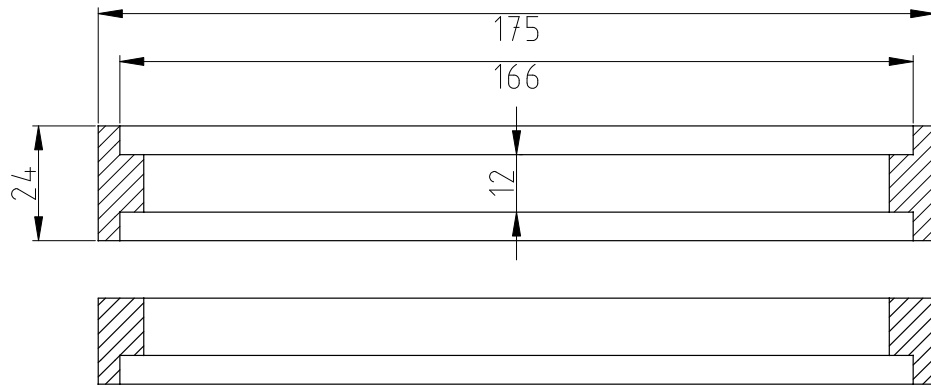


b) LC-07: Assembly Upright

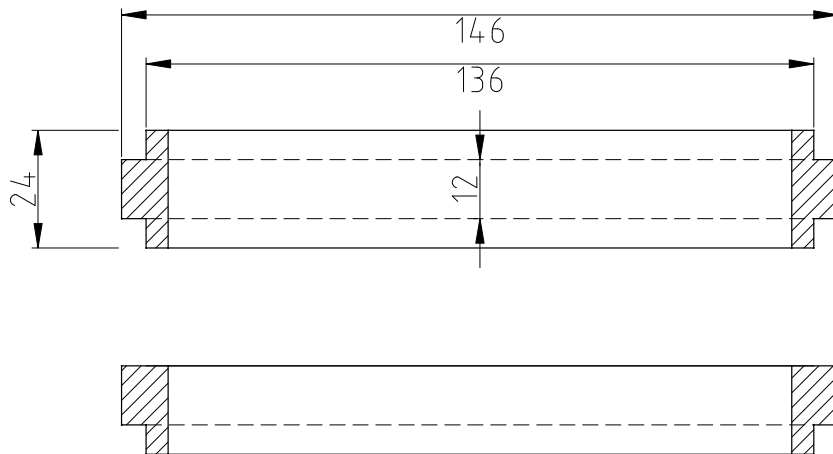


c) 3D CAD Representation of the Bearing Assembly

Figure C.10: Inner Stator Bearing Assembly: LC-06 and LC-07



a) VC-01: Outer Magnet Array Vesconite Rings



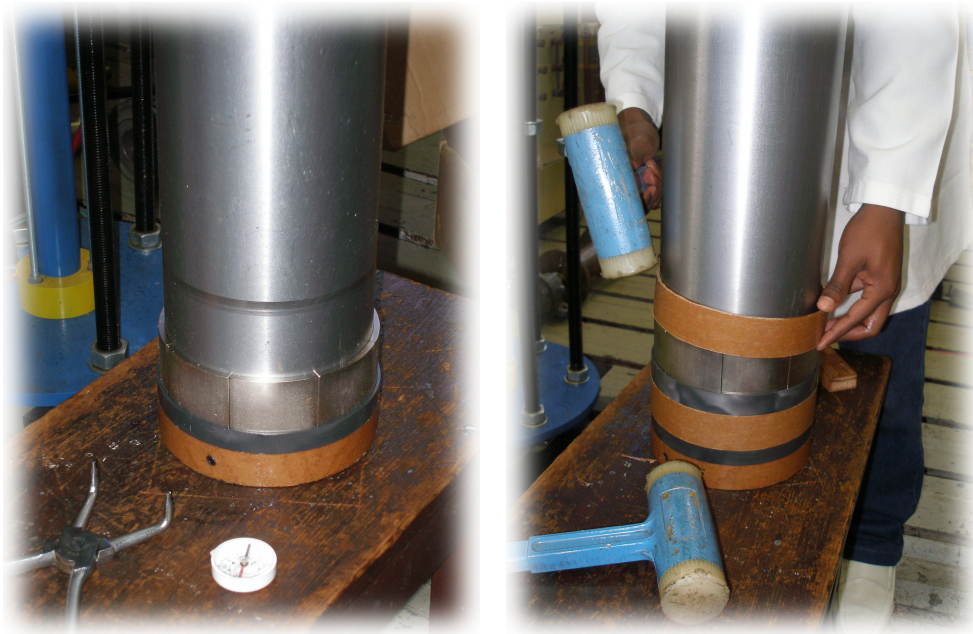
b) VC-02: Inner Magnet Array Vesconite Rings

Figure C.11: Vesconite Retaining Rings: VC-01 and VC-02. The top version of each ring was used in-between layers of magnets. The lower version of each ring was used at the ends of the magnet array where a subsequent layer was not present and so did not require a retaining lip.

C.2 Construction Procedure

C.2.1 Translator Construction

The translator was assembled in two stages. The inner magnets were laid first, and the outer magnets thereafter. The reverse order is not practical as the outer magnets would have been attracted to the metal machine bed on which the translator was laid. It was not possible to take photographs of the inner array assembly because of the aperture of the translator core. The following sequence of images shows the assembly of the outer magnet array. The procedure for the assembly of the inner magnet array was identical. The magnets were handled very carefully because their volume and quality made the forces involved rather dangerous.



a) Tufnol and Vesconite Supports

b) Tufnol Sleeve Placement

Figure C.12: Tufnol and Vesconite Support Structures for the Permanent-Magnets.

The translator assembly begins with the fixing of the lower Tufnol support onto the base of the translator. The inner and outer supports were affixed to the translator core by means of grub screws which passed through the core and into the supports as shown in Figure C.12 a).

The Vesconite magnet support was placed on the translator thereafter, and the magnets slipped beneath the lip of this support. Once a ring of magnets had been completed, a Tufnol sleeve was placed over the ring as shown in Figure C.12 b). This served two purposes: firstly it protected the magnets, and secondly it provided a consistent surface on which the bearings would run.

Each magnet was inserted, at an angle, into the lip of the Vesconite retaining ring as shown in Figure C.13 a). It was then gently eased onto the translator core surface using a tapered tool like a screwdriver. The individual magnets were then gently tapped as far into the Vesconite ring as possible using a rubber mallet.



a) First Magnet

b) Last Magnet

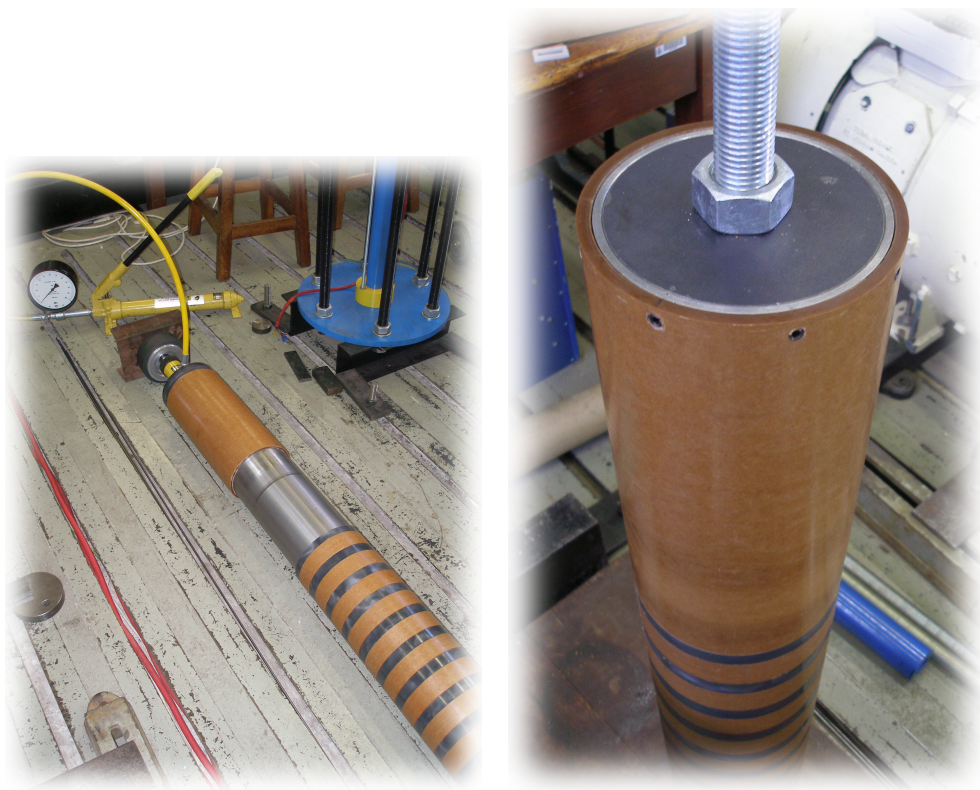
Figure C.13: Placement of the Permanent-Magnets on the Translator Core.

The magnets repelled each other on their vertical faces, and so tended to distribute themselves horizontally. This was not a problem until the last magnet in the ring was to be placed. The circlip pliers, shown in Figure C.12 a), were used to force the magnets together, making space for the last magnet in the ring to be slid in from the top. Once adequate space had been made for the last magnet to fit in, it was tapped in from the top of the ring using the rubber mallet as shown in Figure C.13 b).

The polarity of the outer magnets, relative to the polarity of the inner magnets was checked using a compass, shown in Figure C.12 a), so as to ensure that the magnetic circuit was in series.

The completed magnet array was comprised of ten poles. Handling of the completed translator became important as nearby magnetic materials would adhere to the surface of the array, sometimes with great velocity and force.

The final Tufnol sleeve was inserted over the translator core to provide the uniform surface on which the bearings would run. This is shown in Figure C.14 a). The magnets' strength was used to our advantage; the translator was stuck to the machine bed preventing the translator from slipping out of position. A hydraulic jack was used to compress the final



a) Final Tufnol Sleeve

b) Mechanical Connection

Figure C.14: Completion of the Translator Assembly

assembly, making sure that all magnets, Vesconite rings and Tufnol rings were as closely packed as possible.

The mechanical connection to the translator was at its top and is shown in Figure C.14 b). The metal plate through which the M30 threaded rod was connected, was fastened onto the translator core via eight grub screws. The M30 nut on the underside of the metal plate was welded to the plate so that the threaded rod could be easily removed without the nut falling out of place and adhering to the magnets within.

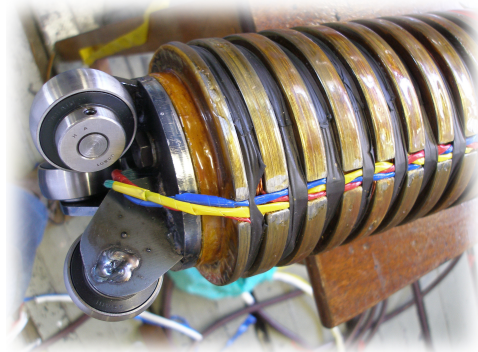
An M30 lifting eye was placed on the other end of the M30 threaded rod from which the crane could hoist the translator. This was the means of force application during the static force tests.

C.2.2 Inner Stator Construction

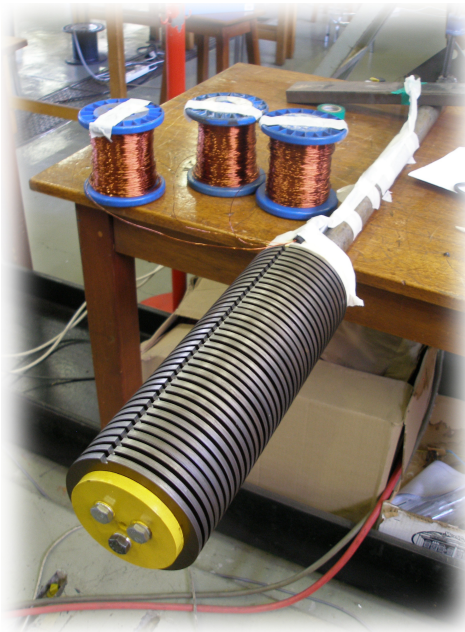
The inner stator was constructed from a long mild-steel core, over which the rotary laminations were placed. Figure C.15 a) shows the components which formed part of the inner stator. The yellow end-supports were used to clamp the assembly of laminations together over the black stator core. Thin mild-steel spacer rings were used to enforce a spacing between sets of laminations. The stator windings were wound using 0.9mm round copper wire, shown on the blue bobbins.



a) Components



b) Completed Assembly



c) Windings



d) Polarity Check

Figure C.15: Inner Stator Assembly

The assembled stack without windings is shown in Figure C.15 c). This particular picture is from a previous design when q_i , the number of slots per pole per phase was equal to two. The design was subsequently changed to $q_i = 1$ because of limitations on the available outer

stator square wire. The effect of the thin spacer rings is evident from this figure. The yellow end-supports were used to clamp the stack together using M8 bolts, threaded into the mild-steel core.

The completed lamination stack was then covered in resin to provide electrical insulation for the windings from the stack. Insulating paper was tried, but the cylindrical slot made curling the paper impractical.

Figure C.15 c) also shows the three bobbins which were used to wind the stator's three phases. During the winding, each completed slot was covered in insulation tape as an interim step to hold the windings in place. Each colour represented a different phase. Once completed, a direct current was passed through the windings to confirm the alternating polarity of the windings' magnetic field, as shown in Figure C.15 d).

The insulation tape was replaced with a black adhesive rubber tape to complete the winding. Figure C.15 b) shows the completed assembly as well as the inner stator's bearing assembly.

The bearing assembly consisted of three insert bearings at 120° angular displacement. This assembly provided contact points against the inner surface of the translator assembly, and would run against the Tufnol which was used in the translator. With the base of the translator fixed to the machine's structure, this bearing assembly was considered sufficient to prevent the inner stator core from bending towards the permanent-magnets and adhering to the translator's surface from within.

C.2.3 Outer Stator Construction

The machine's structure was comprised of six M30 threaded rods for vertical support. During the assembly of the outer stator however, only three were used in the initial stages to simplify the assembly. The remaining three threaded rods were inserted after the outer stator's top support had been placed.

The assembly began with the levelling of the outer stator's lower support using a spirit level. The nuts on the threaded rods were adjusted to achieve a level platform on which to assemble the stator. The mild-steel outer core was placed in the spigot of the lower stator support. The packs of laminations and pre-made windings were then inserted into the core as shown in Figure C.16 a).

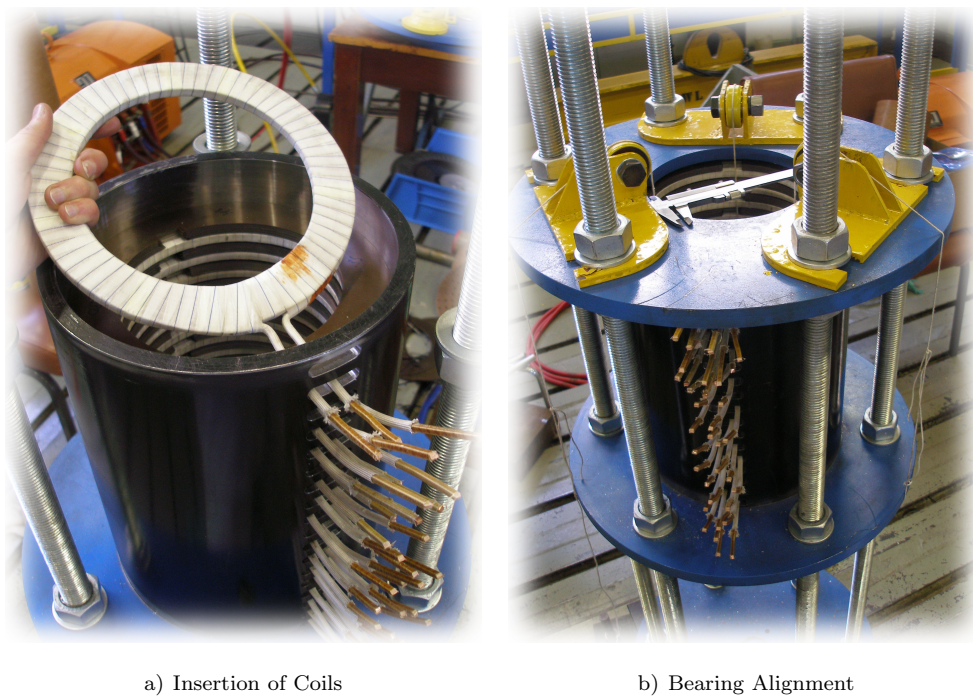


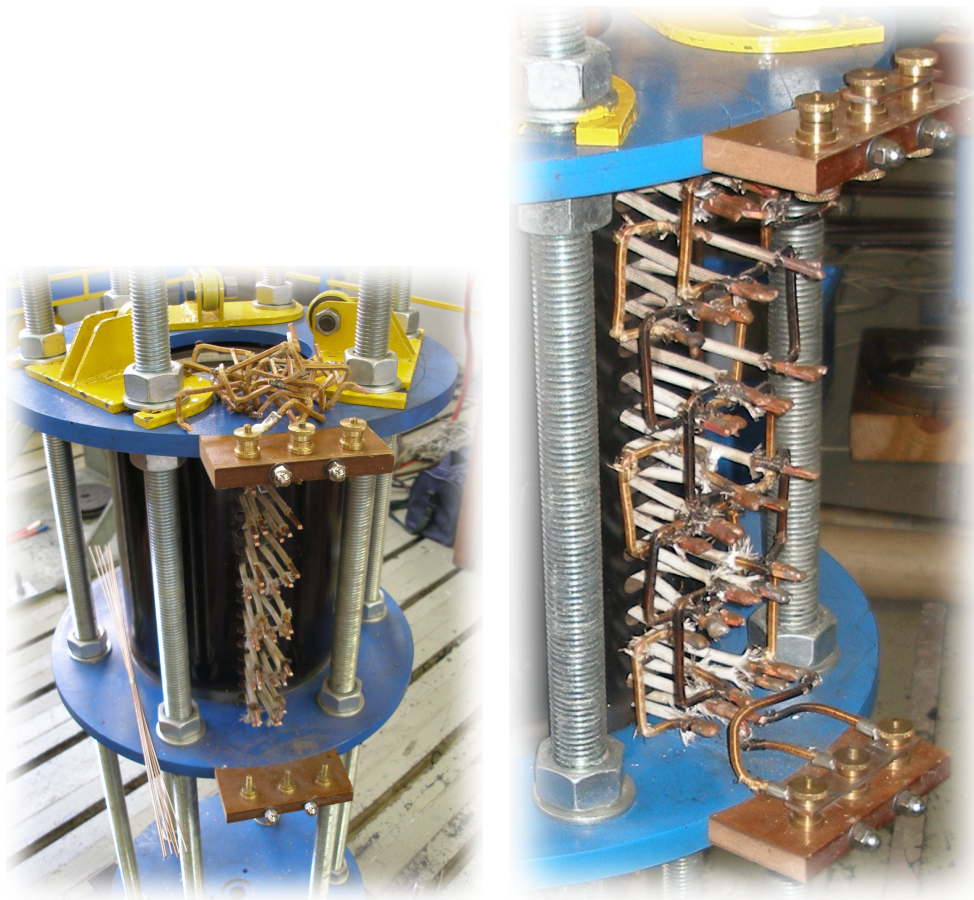
Figure C.16: Assembly of the Outer Stator

Once the final pack of laminations was inserted (which aligned the top of the laminations with the top of the stator core), the stator's top support was placed over the core to fix the assembly in place. At this stage the yellow bearing assemblies were also placed at the top and bottom of the assembly as shown in Figure C.16 b). A plumb-line technique was used to align the bearings, using a vernier calliper to measure the distance between the string and the stator supports.

The individual coils were brazed together to form the three-phase stator winding arrangement. Figure C.17 a) shows the coil linkages, and the brazing rods, which were used to join the individual coils.

The figure also shows the terminals which were installed to which the stator windings would eventually be connected. The lower set of terminals was used as the star point of the three-phase winding while the electrical connection to the excitation system was made at the top set of terminals.

To prepare for brazing, a plate was placed between the left and right ends of the coils. This prevented the heat, generated from brazing the one side of the coils, from burning the coils on the other side. Figure C.17 b) shows the completed stator windings, terminated at the terminals provided. This marked the completion of the outer stator assembly.



a) Coil Linkages

b) Completed Windings

Figure C.17: Outer Stator Assembly: Brazing of the Outer Stator Coils.

C.2.4 Stator and Translator Integration

The final step in the construction of the machine was the integration of the two stators and the insertion of the translator in-between the two stator assemblies. Figure C.18 illustrates the main tasks involved in the system integration.

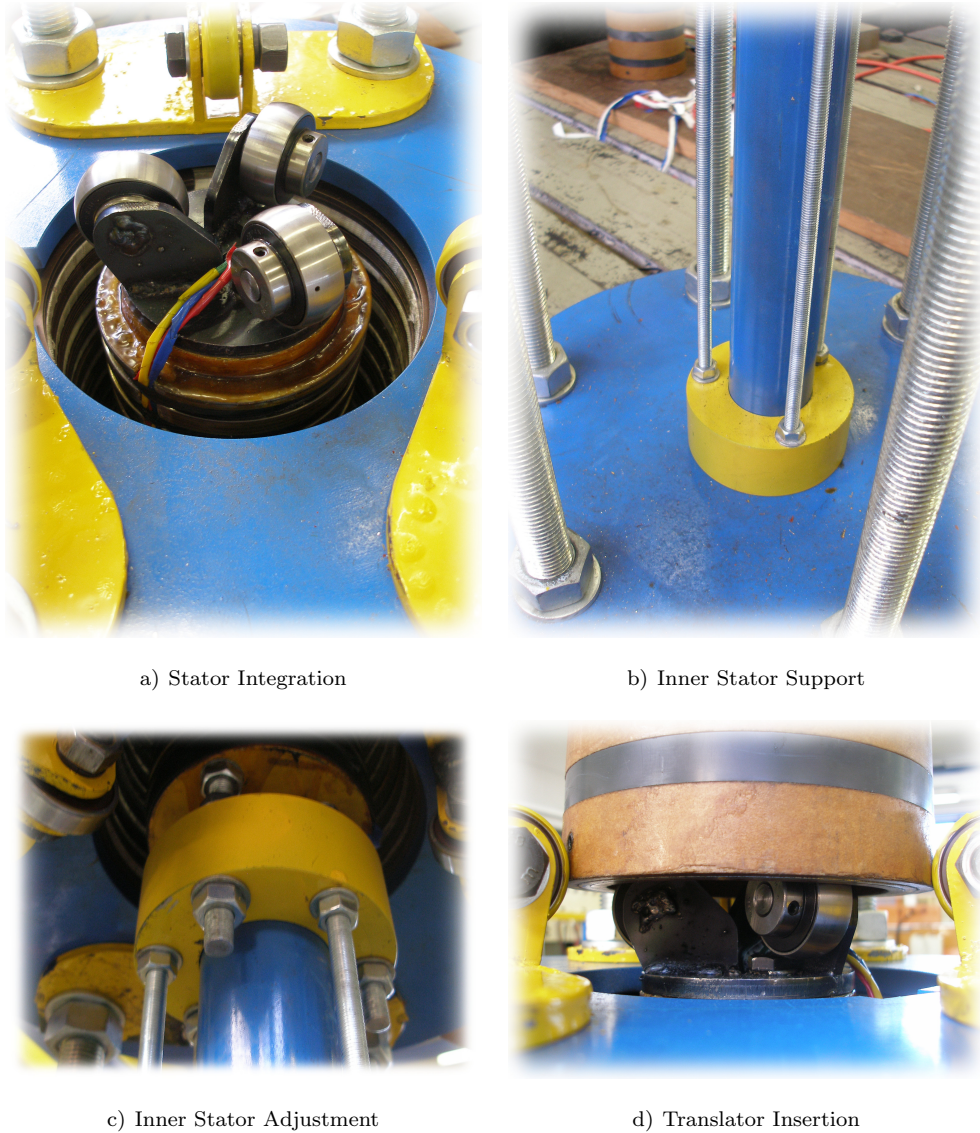


Figure C.18: Integration of the Two Stators and the Translator into the Final Assembly.

Figure C.18 a) shows the alignment of the two stators. The inner stator assembly was lowered into the opening in the outer stator and fixed to the base of the structure as shown in Figure C.18 b). The use of M10 threaded rods gave the structure rigidity, preventing the inner stator from bending towards the magnets on the translator. This was a significant concern because of the high energy product of the magnets.

The nuts on the M10 threaded rods were used to provide tension to inner stator support.

At the base of inner stator stack, a set of threaded rods were used to adjust the alignment and height of the inner stator relative to the outer stator, as shown in Figure C.18 c).

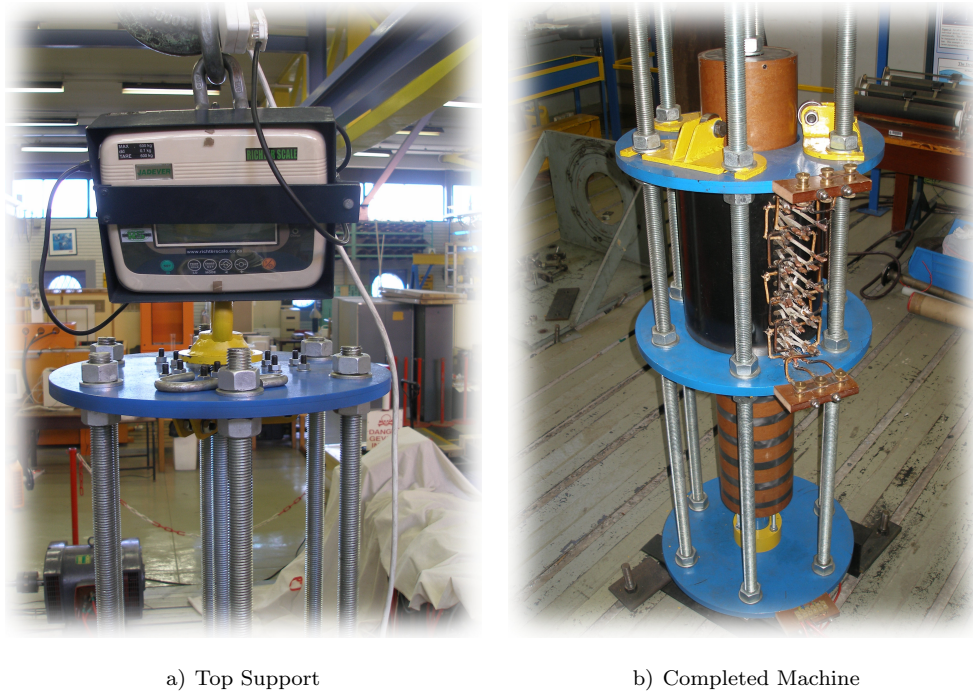


Figure C.19: Completed Prototype Machine

After final alignment of the bearing assemblies, the machine was completed. The top of the machine is shown in Figure C.19 a), excluding the metre-rules which were used for the measurement of the translator position. The completed machine with the translator inserted in-between the stators, and running appropriately on the bearing assemblies is shown in Figure C.19 b).

C.3 Conclusion

The specifications and design of the Double-Sided Tubular Permanent-Magnet Linear Synchronous Generator prototype have been presented as well as the procedures employed during the construction of the prototype. All pertinent dimensions and mechanical drawings have been presented as well as a list of suppliers. The machine was built in the Electrical Engineering workshop in the Genmin Laboratories at the University of the Witwatersrand, and was completed in September 2008.